POWER HANDLING OF LIQUID METAL INFUSED TRENCHES IN THE EAST TOKAMAK

BY

DANIEL O'DEA

THESIS

Submitted in partial fulfillment of the requirements
for the degree of Master of Science in Nuclear, Plasma and Radiological Engineering
in the Graduate College of the
University of Illinois at Urbana-Champaign, 2020

Urbana, Illinois

Master's Committee:

Research Assistant Professor Daniel Andruczyk
Professor David Ruzic

Abstract

Flowing liquid metal PFCs offer an attractive solution to the problems currently facing conventional solid high-Z PFCs such as: the sputtering of high-Z impurities into the core, fuzz formation from helium implantation and thermal damage (melting, blistering and cracking.) By presenting a constantly refreshing surface to the plasma liquid metal PFCs protect against damage by removing heat via convection from the system and by acting as a particle sink thereby preventing sputtering of high-Z atoms. Lithium is the popular choice for liquid metal PFCs as it is a low-Z element and is a strong chemical getter so can remove impurities from the plasma greatly enhancing confinement time within the plasma. Lithium also reduces the recycling of hydrogenic species at the plasma edge decreasing the collisional cooling in these regions consequently keeping the edge of the plasma hot. Maintaining a hot plasma edge flattens the temperature gradient across the plasma which in turn suppresses the anomalous turbulent transport, stabilising the plasma against ELMs and greatly increasing confinement time.

In order to develop lithium PFC technology: three generations of a FLiLi type limiter have been tested in EAST. The tests in EAST have shown the inclusion of FLiLi to increase the confinement time within the tokomak, reduce large scale ELM and produce ELM free periods as well as reducing the recycling within the plasma increasing stored plasma energy. In continuation of this work a LiMIT type limiter was exposed to the EAST plasma and this experimental campaign will form the basis of this work. The LiMIT design consisted of a trenched front face with 2mm wide 1mm trenches, these trenches allow for lithium flow to be driven by TEMHD via the Seebeck effect. Previous work at UIUC has shown the ability for a LiMIT design to produce velocities of $\sim 60 cms^{-1}$ and withstand heat fluxes of $10 MWm^{-2}$ under electron beam exposure. Complementary to the experimental data a COMSOL model has been developed to calculate the heat absorbed into the TZM backplate of LiMIT by correlating the simulated temperature profiles over the plasma exposure with the experimentally measured TC. This data can then be combined with calculations of the heat absorbed into the lithium film via convection and the power dissipated by a lithium vapour cloud formed above the plate to produce a measurement of the total heat flux experienced by the plate and begin to benchmark the heat handling capabilities of the LiMIT design.

The most extreme conditions faced by the LiMIT plate occurred with $6.7MW$ of auxiliary heating with the plate positioned 2cm from the separatrix. In this case a conductive heat strike of $8.2MWm^{-2}$ was calculated in COMSOL further supplemented with $5MWm^{-2}$ dissipated by the vapour cloud. This result displays the ability of the LiMIT design to exceed the maximum heat limit for tungsten PFCs of $10MWm^{-2}$ and further still the LiMIT design withstood multiple high powered NBI shots with heat fluxes above $10MWm^{-2}$ with no macroscopic damage caused to the plate highlighting LiMIT's ability to protect against multiple exposure to high temperature plasma. Increase in plasma performance was noted with lithium evaporation and subsequent redepostion on EAST's divertor regions: during RF heated shots this effect conditioned the device leading to a transition from low to high confinement operation and with NBI heating; shots subsequent to large lithium evaporation from LiMIT produced plasmas with increased density, stored energy and confinement time due to a decrease in the global recycling. Development of the COMSOL model elucidated the interaction between the EAST plasma and LiMIT. The plasma strike points were found to be localised to the ion and electron sides of the plate, with the ion side experiencing a heat flux an order of magnitude higher than the electron side.

To Gran

Acknowledgments

I would like to start by thanking Professor Daniel Andruczyk for offering me a place in his group and his constant support and tutorage not only with my work at UIUC but also with my transition to life in a new country. I must of course say thanks to Professor David Ruzic for his advice at key moments of the project along with his welcoming nature that has allowed me to find a home within his laboratory.

Special thanks must be given to Professor Rajesh Maingi and Professor Zhen Sun, not least than for sitting through hours of meetings presented by myself, without their help and guidance I would still have a rudimentary understanding of the nature of fusion plasma and this project would have never been realised.

Finally thanks must go to all my colleagues and lab work for their constant help and support academically and personally. In particular: Alfonso De Castro, Rabel Rizkallah and Steven Stemmley who played major roles throughout this work.

Table of Contents

List of Tables

List of Figures

List of Abbreviations

PFC	Plasma Facing Component
FLiLi	Flowing Lithium Limiter
EAST	Experimental Advanced Superconducting Tokamak
ELM	Edge Localised Mode
LiMIT	Liquid Metal Infused Trench
TEMHD	Thermoelectric MagnetoHydrodynamics
UIUC	University of Illinois at Urbana Champaign
TC	Thermocouple
ITER	International Thermonuclear Exxperimental Reactor
MCF	Magnetic Confinement Fusion
ICF	Inertial Confinement fusion
JET	Joint European Tauras
MHD	MagnetoHydrodynamics
W7-X	Wendelstein 7-X
DEMO	Demonstration Power Plant
JT-60	Japan Torus-60
ST-40	Spherical Tokamak-40
SPARC	Soonest/Smallest Private-Funded Affordable Robust Compact.
ITG	Ion Temperature Gradient
TEXTOR	Tokamak Experiment for Technology Oriented Research
ASDEX-U	Axially Symmetric Divertor Experiment-Upgrade
ALCATOR C-MOD	Alto Campo Toro
TFTR	Tokamak Fusion Test Reactor
LTX	Lithium Tokamak Experiment
FTU	Frascati Tokamak Upgrade

CPS	Capillary Porous Systems
H Mode	High Confinement Mode
L Mode	Low Confinement Mode
SOL	Scrape Off Layer
EM	Electromagnetic
MAGLIMD	Magneticallly Guided Liquid Metal Divertor
SEM	Scanning Electrom Microscope
FLIT	Flowing Liquid Torus
CPMI	Center for Plasma Matter Interaction
HT-7	Hefei Tokamak-7
PSI	Plasma Surface Interaction
MAPES	Material and Plasma Evaluation System
RF	Radio Frequency
ECRH	Electron Cyclotron Resonance Heating
LHW	Lower Hybrid Wave
NBI	Neutral Beam Injection
EP	Enhanced Pedestal
NSTX	National Spherical Torus Experiment
IR	Infrared

List of Symbols

τ_ϵ	Confinement Time
W_{MHD}	Plasma Energy
P_L	Plasma Power Lost
k_b	Boltzmann Constant
q	Elementary Charge
R_c	Radius of Curvature
q_s	Safety Factor
a	Minor Radius
R_0	Major Radius
B_T	Toroidal Magnetic Field
B_{pol}	Poloidal Magnetic Field
Q	Scientific Q factor
H	Confinement factor
κ	Plasma Elongation
A	Reactor Aspect Ratio
P_{sep}	Power Across separatrix
λ_q	Heat Strike Width
R	Hydrogenic Recycling Ratio
V_p	Plasma volume
β	Plasma Beta
P_{fus}	Fusion Power
$< p >$	Average Plasma Pressure
ρ_{ion}	Ion Gyroradius
D_α	D_α spectral line
S	Seebeck Coefficient

Q_{plasma}	Plasma Heat Flux
Q_{vap}	Heat Dissipated in Lithium Vapour Cloud
Q_{Conv}	Heat Stored in Lithium via Convection
Q_{TZM}	Heat Conducted into TZM backplate
Γ_{vap}	Evaporative Flux
ϵ_{cool}	Average Energy lost by Lithium Atoms entering SOL
E_{vap}	Energy of Vaporisation
p_{Li}	Lithium Vapour Pressure
λ_{ion}	Mean Free Path of Ionisation
$< \sigma\nu >$	Rate Coefficient for Ionisation
C_p	Heat Capacity at Constant Pressure
u	Fluid Velocity
h	Height of LiMIT Trench
t	Thickness of LiMIT Trench
Ha	Hartmann Number
σ	Li Conductivity
μ	Li Dynamic Viscosity
$q_{\parallel}$	Parallel Heat Flux
$q_{\perp}$	Perpendicular Heat Flux
σ_a	Standard Deviation in a

Chapter 1

Introduction

1.1 Nuclear Fusion

As the classical energy sources are depleted and their negative impact on the health of both ourselves and the planet become more apparent; the development of a renewable green energy source is of vital importance. Nuclear fusion is certainly one of the more exciting solutions to this problem, by harnessing the reactions that power the Sun an abundant energy source that produces minimal waste products may be realised. With the only waste produced from the building supplies and energy production constrained only by hydrogen supply which should last 1000yrs [10].

Though to utilise such an ideal source presents a variety of challenges. To overcome the strong electromagnetic repulsion between two nuclei, fusion reactions must occur at extremely high temperatures and pressures, at which a gas is fully ionised and forms a plasma. These conditions present major issues: firstly, how to overcome the huge mechanical forces present in a very dense hot gas (when heating solid/liquid Deuterium to 10^5K the pressure exceeds 10^6atms [11]) that act to expand the gas and secondly how to avoid massive thermal losses between the hot gas and it's surroundings. These factors require novel and innovative techniques to create and then contain such a plasma without destroying the vessel it occupies and sustaining a burn for a long enough duration to extract energy, these challenges are so great that as of writing no machine has surpassed the engineering breakeven.

Clearly a third parameter alongside pressure and temperature is going to play a major role in the likelihood of fusion reactions, one that is a measure of how long the nuclei can be contained at high enough energy and density for a fusion reaction to occur. This third parameter is known as the energy confinement time. Armed with these three major parameters a triple product can be defined [12] which gives the lower limit for the product of the density, n, temperature, T, and the confinement time, τ_ϵ required to reach ignition, a plasma that is self-heating. A plot of the minimum triple product ($nT\tau_\epsilon$) required for ignition

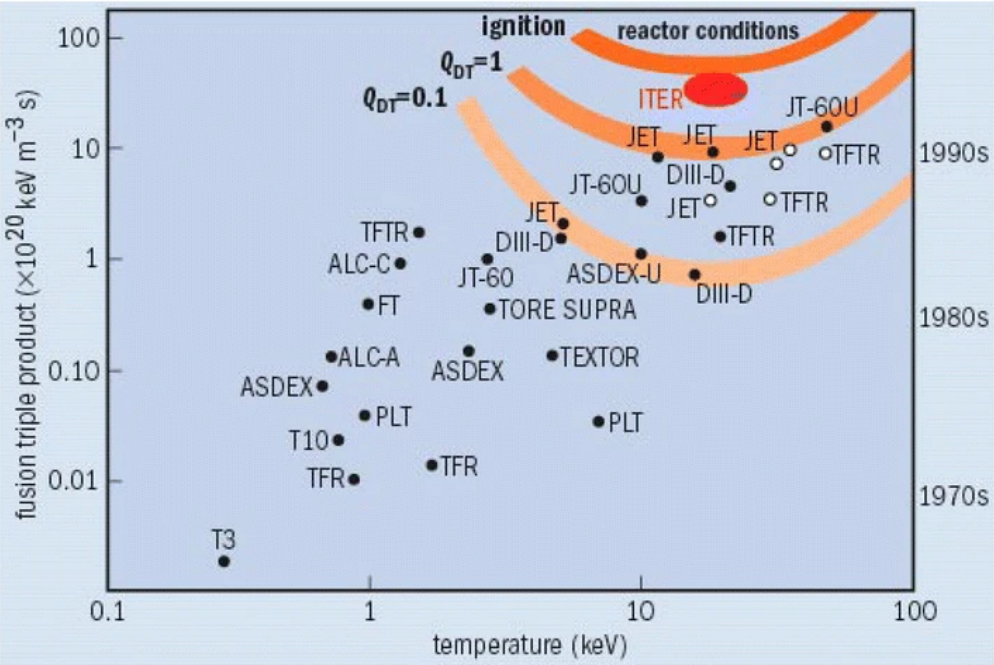

Figure 1.1: Plot of the triple product for ignition, $Q_{DT} = 1$ and $Q_{DT} = 0.1$ for a deuterium tritium plasma. Also shown are the values of triple product measured in the major global fusion devices where the black dots indicated a D-D plasma and the white a D-T plasma; the predicted ITER triple product is shown by the large red circle. With the D-D values it is important to note that though Deuterium is more readily available and is not radioactive making it a better fuel than tritium the triple product is more stringent for such a plasma [1]

in a D-T plasma against plasma temperature is shown in figure 1.1. along with values measured in major global fusion devices and a predicted triple product for ITER. It is important to mention that the black dots represent a D-D plasma which has a more stringent ignition condition, its minimum triple product occurs at a higher temperature. The general shape of the triple product is that initially it decreases with temperature, as the plasma requires large enough temperature to exceed the repulsion between the positively charged nuclei, till a minimum value is reached the product then increases with temperature, due to the drop in reaction cross-section for the DT reaction as at high enough temperature collisions between particles become increasingly rare. The minimum ignition value for a deuterium-tritium reaction (D-T) occurs at a temperature of 22keV has a criterion given by:

$$nT_p\tau_\epsilon \geq 2x10^{21} keV s m^{-3} \tag{1.1}$$

This ignition condition is achieved when the power transferred to the D and T nuclei by alpha particles via collisions is equal to the power lost due to diffusion (defined as $P_L = \frac{W}{\tau_\epsilon}$) and the plasma therefore requires no external heating to stay hot, this is complicated by the inclusion of bremsstrahlung radiation losses which

makes the ignition condition more strenuous. Two main methods have been developed to achieve ignition Magnetic Confinement Fusion (MCF) and Inertial Confinement Fusion (ICF.) MCF looks to maximise τ_ϵ , with values on the order of a few milli-seconds, and a moderate density ($10^{22}m^{-3}$) whereas ICF maximises n ($10^{29}m^{-3}$) to overcome low confinement time. ICF has achieved a comparable Lawson criterion to MCF, $\rho\tau \approx 1.2 - 1.5atms$ [13] for cryogenic implosions in OMEGA compared to $\rho\tau \approx 1atms$ [14] measured in JET though MCF has reached a higher value of ignition condition due to the higher temperatures present in such devices (10keV compared to 2keV in ICF [15].) Due to the nature of this thesis and that is a more widely researched area focus will be given to MCF.

MCF research began with a device known as a theta-pinch. The device is effectively solenoid with two endcaps, if a high enough current is applied to the solenoid electrons and ions are trapped on the magnetic field lines formed within tracing Larmor orbits as they progress along them. However, this still does not provide the confinement times required for fusion as there is a massive particle loss at either end of the pinch. To overcome this it was proposed to wrap the solenoid into a torus forming an 'infinite cylinder' clearly eliminating the end losses. However, the bending of the field lines within the torus produces two guiding centre drifts that allow particles to deviate from the magnetic lines. The first of these drifts arises from the curvature of the field lines within the torus, in order for particles to follow the curved field lines there must be a centripetal force acting. This centripetal force gives rise to a velocity component perpendicular to the toroidal magnetic field and the radius of curvature (R_c) producing drift in this direction. The second drift arises from the gradient of the magnetic field in the radial direction, magnetic field is highest on the inner edge of the torus and lower on the outer edge, which produces a drift perpendicular to both ∇B and B . Equations for curvature drift and gradient drift are shown in equations (1.2) and (1.3) respectively.

$$v_{\nabla B} = \frac{2k_bT}{qB}\frac{\vec{B}x\vec{\nabla B}}{|B|^2} \tag{1.2}$$

$$v_{\nabla B} = \frac{2k_bT}{qB}\frac{\vec{R_c}x\vec{B}}{|R_c|^2|B|} \tag{1.3}$$

Where k_b is the Boltzmann constant, q is the elementary charge and T is the temperature of the drifting species. As the ∇B and R_c are in the same direction the drift velocity will be in the same axis, though the dependence on charge means that electrons and ions will drift in opposite directions. This drift will produce a radial electric field that when crossed with the toroidal magnetic field will cause the plasma to drift inwards towards the wall where it will extinguish. The solution to this was proposed by Tamm in his 1929 work 'Fundamentals of the Theory of Electricity' and further improved upon by Sakharov and

Tamm in 1950. They theorised that by including a poloidal magnetic field a rotation was introduced to the magnetic field lines which enabled particles on the outer edge of the plasma to transit to the inner edge effectively short-circuiting the charge separation. Though the picture is still not developed as early devices with both toroidal and poloidal fields were still plagued by instabilities. It is known now that these machines exhibited 'sausage' and 'kink' instabilities arising from a magnetohydrodynamic (MHD) imbalance between the poloidal magnetic field pressure and the pressure gradient. In 1951 Shafranov elegantly proved the critical stability criterion for a tokamak that the safety factor q_s must be greater than one [16]. The safety factor is defined as the number of toroidal transits for one poloidal transit and can be controlled by the ratio of the toroidal to poloidal magnetic field and its value on the magnetic axis is given by the equation:

$$q_s = \frac{aB_T}{R_0 B_{pol}} \tag{1.4}$$

Where a is the minor radius, B_T is the toroidal magnetic field, R_0 is the major radius and B_{pol} is the poloidal magnetic field. The Shafranov stability factor can simply be seen as the fact that the toroidal field must be greater than the poloidal field in order for the magnetic tension in the toroidal field to stabilise the MHD instabilities long enough to confine the plasma. Though not stated during the discussion for the necessary inclusion of a poloidal field there is an upper limit on the safety factor set by the required time for charge reconnection to prevent the catastrophic ExB drift. Tokomaks can still only confine particles on the order of seconds due to the toroidal current that flows on axis within the device. This current though beneficial in heating the plasma, via ohmic heating, ultimately leads to current driven instabilities, such as the n=0 mode which can cause unstable vertical displacement of the plasma, [2] that make it near impossible to operate a tokamak in steady state, though it is theorised that a perfectly conducting wall would reduce this instability.

This brings us to the topic of the stellarator, a MCF device developed concurrently with the tokamak and credited to the project Matterhorn at Princeton University. In 1958 Spitzer presented the concept by suggesting a torus bent into a figure of eight which introduced the rotational transform directly into the cross-section plasma without the inclusion of a poloidal field thereby eliminating the central plasma current present in a tokamak [17]. The stellarator design has evolved to now having the same torus-shaped reactor as the tokamak but only one set of non-axisymmetric coils, such as W7-X, which are designed to introduce the twist to the plasma within a stellarator while also providing the toroidal confinement. A image showing a comparison between a tokomak and stellarator plasma can be found in figure 1.2 the tokomak exhibits a 2-D axisymmetric plasma with the curvature produced by the fieldlines whereas the stellarator exhibits a 3D plasma shape with the twist produced by the plasma itself. The clear benefit of the stellarator is the

ability to operate in the steady state due to the large reduction in current driven MHD instabilities present in tokamaks, this reduction of instability has a secondary benefit of reducing disruption within the device which can be catastrophic to plasma performance and the lifetime of surrounding PFCs. The issues with the stellarator ultimately arise from the complexity (in both design and the plasma shape) and the cost (not only with the extra design complexities but also on the greater reliance on external heating source due to the lack of ohmic heating present.) It has also been shown that the neo-classical transport is far higher in stellarators at high electron temperatures [18] leading to much higher neo-classical particle losses in stellarators leading to issues with the fuelling of such devices.

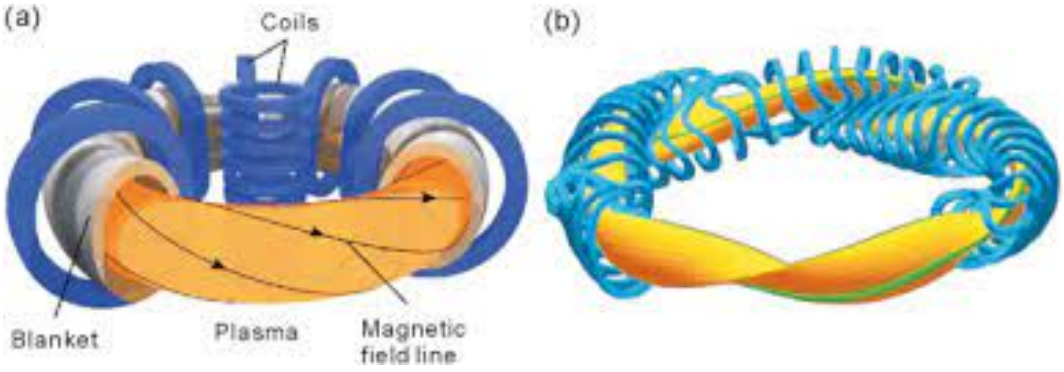

Figure 1.2: Comparison of a tokamak (a) and stellarator (b) plasma shape [2]. The tokomak produces a 2-D axisymmetric plasma with the curvature of particles induced by the field lines differing from the 3D twisted plasma produced by a stellarator which requires a far more complicated design but offers great instability reduction.

1.2 Fusion Stagnation

The enormity of the challenge faced by the fusion community is a highlighted through the progression of the most vital parameter when viewing fusion as a viable electrical source; the scientific Q factor, $Q = \frac{P_{out}}{P_{heating}}$. In 1996 the Joint European Taurus (JET) recorded a Q factor of 0.6 for a D-T plasma [19] and though 24 years have passed no higher value has been recorded. Obviously, advancements have been made in the field with magnet design, plasma shaping and heat handling, but the length of time required to build new devices (ITER, DEMO etc.) coupled with the rapid deterioration of current machines the limits fusion recent research progression in fusion to glacial at best. Further highlighting this point, in a recent paper [3] plotted the fusion triple product in major fusion reactors against the year it was measured in, figure 1.3. As one can see there is a rapid increase faster than Moore's law for semiconductors [20](note that the y-axis is a log scale) up until 2000 with a maximum value for triple product of $1.1x10^{21}m^{-3}skeV$ being obtained by JT60 in 1994 [21]. Following this rapid growth however, there is a mass stagnation while the ITER project

faces further and further delay.

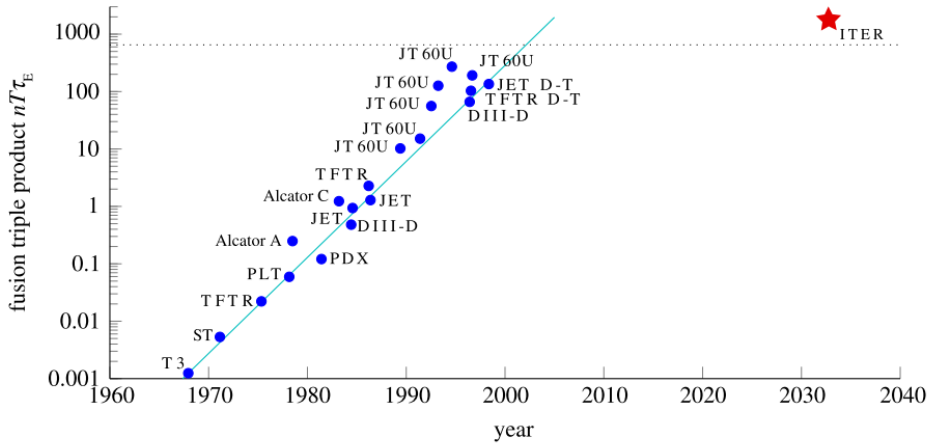

Figure 1.3: Figure showing the improvement of triple product measured with time. Up until 2000 a rapid increase in the triple product was observed, however a plateau in improvement followed as the ITER project is constructed. The units on the yaxis are $x10^{21} keV m^{-3} s$. [3]

Costly also outlines a proportionality of the triple product with key fusion parameters.

$$nT_p\tau \propto H^2 q_s^3 R_0^2 B_T^3 \kappa^{\frac{7}{2}} A^{-3} \tag{1.5}$$

Where H is the confinement factor, q_s is the safety factor, R_0 is the major radius, B_T is the the toroidal field, κ is the elongation and A is the aspect ratio of the reactor. Clearly large devices, i.e larger R, will favour the triple product and this is the idea pursued by the ITER and DEMO concepts. Alongside this the larger R will decrease the heat loads on both the first wall due to the larger vessel volume and the divertor by reducing the ratio of power across the separatrix to the major radius P_{sep}/R_0, this will obviously increase the lifetime and reducing the heat handling requirements of PFCs decreasing the downtime facing a reactor. Due to gyro-bohm diffusion scaling inversely with minor radius (chi is proportional to normalised larmor radius, equal to larmor radius over minor radius [22]) such a device will show an improved confinement time [23].

At this point of the piece one may find themselves with the belief that once ITER is operational Fusion power will be far along in its journey to becoming a commercial energy source. The key word here is 'once', the ITER project was proposed in the 1980s and has cost over $ 20 billion dollars to date [24]. Though the initial years were slowed by the geo-politics of the cold war and the project took a while to get off the ground;

even in recent years the project has been characterised by delays: 'in the Roadmap to Fusion energy' [25] published in 2012 stated that ITER would be operational by 2020 and construction of the first DEMO reactor completed in 2030. As of 2016 ITER's first plasma will be in 2025 and the first D-T shots are scheduled for 2035 (shots likely to produce the highest Q factor.) Now this isn't entirely fair as an experimental reactor ITER is not the model for the construction time and cost of a commercial fusion reactor but its frequent delays highlight the mountain of question and issues facing the fusion community and begs the colloquial question if putting all of our eggs in (an admittedly large) basket is the strongest course of action. To highlight this point lets turn our attention to a paper from Cardozo [26] which compares the growth of fusion to other renewable energy sources: nuclear, wind and solar. In the paper it is stated that for fusion to follow the growth shown by the three other renewable energy sources post ITER: 3 DEMO like reactors producing energy at $\approx \$60/W_{eff}$ will need to be operational in 2050, 10 GEN I reactors ($\approx \$30/W_{eff}$) now attached to the power grid will need to be built by 2060 and 100 GEN II reactors ($\approx \$15/W_{eff}$) operational in 2070. The stringent nature of these time frames combined with the frequent delays in the ITER project really leave fusion at risk of being left behind by the other sources of renewable energy. The prospect of fusion power on the grid via large devices becomes more concerning when the capital upfront costs are considered which scale with device volume [27] with the already massive cost of ITER the likelihood of building many more larger devices would appear unfeasible without significant cost reduction/engineering developments.

The big machine approach also produces a homogeneity in research that is very rigid. With only one experimental reactor, the ability to study new avenues are restricted and this is further amplified for the ITER project as the sizeable percentage of large tokomaks around the world are now installing ITER-like components for testing. For a field in its relatively infancy this approach runs the risk of ignoring viable research avenues.

This issue can be rectified through the development of multiple smaller devices that maximise magnetic fields and optimise plasma shape (elongation and aspect ratio) to increase the triple product. ST-40 and SPARC are two spherical tokomaks whose designs kept this in mind. Small devices unfortunately, as is the way with fusion, have their own set of issues. The major problems with small reactors come in regards to heat handling and plasma facing components (PFCs.) To match an ITER relevant Q factor and extracted power small devices will have an extreme temperature profile across the device, vastly increasing the risk of disruptions, and a much higher value of P_{sep}/R_0 this combined with a tiny heat strike width λ_q (as it scales inversely with poloidal magnetic field [28] means that the walls and divertors of such a reactor must be able to handle huge heat fluxes far in excess of what is seen in ITER. It is therefore, apparent in order to build smaller devices that are crucial to the development of technology on a rapid time scale, new novel

approaches for Plasma Facing Components (PFCs) are needed.

1.3 PFCs: Material Choice

Tungsten is currently the material chosen for the ITER divertor [29]. Tungsten exhibits a number of qualities making it suitable as a solid PFC: high melting point , low sputtering yield (in detached plasma regimes) and the ability to sustain neutron bombardment [30] [31] [32]. However, these valuable properties come at a cost, its high atomic mass. When Tungsten is sputtered and enters the core it greatly degrades plasma performance radiating away power in the form of high energy radiation and increasing the effective Z in the core decreasing confinement, in the core a fractional density of 10^{-5} of tungsten extinguishes the plasma [33]. This means that tungsten sputtering must be avoided at all costs, limiting the max heat handling capability of a tungsten divertor to $10MWm^{-2}$ [34] in ITER and this is further restricted to $5MWm^{-2}$ in DEMO [35]. This is far below what will be present in a small device and even in a large ITER-like device. To overcome this issue power needs to be radiated away in the separatrix, effectively detaching the plasma and the wall, and this is achieved by bleeding higher Z materials, nitrogen and neon are the planned gases in ITER [36], into the plasma edge to the radiate the power in a process known as seeding (i.e cover entire machine volume with heat rather that the narrow plasma wetted areas.) It is estimated that ITER will need to radiate around $90 - 95\%$ [37] [38] of its power across the separatrix in order to keep the temperature in front of the divertor below the sputtering threshold $5eV$ [39] and this radiation fraction will be further increased for DEMO [40]. Clearly this will cause a mass degradation in the plasma, firstly as discussed above the high z material can penetrate into the core and radiate away energy, W7-X reported a 10-15% drop in stored energy with active nitrogen seeding [41]. This seeding also requires strict control without which a high to low confinement transition can be triggered and can ultimately lead to a complete radiative collapse of the plasma [42]. Bleeding cold neutrals into the edge also cools the plasma down, through collisions, greatly increasing the temperature gradient across the plasma. One of these gradient is the ion temperature gradient (ITG) which has been shown to be the main driver of turbulent transport within a fusion plasma [43] as the ion diffusion χ_i is the main hot loss mechanism within the core [44]. This effect is further enhanced by tungsten PFCs via recycling, a process where ions incident on a PFC are thermalised to the wall temperature and then reflected as cold neutrals. A recycling ratio can be defined [45]:

$$R = \frac{Hydrogenic\ influx\ back\ to\ plasma\ from\ surface}{Hydrogenic\ flux\ to\ surface\ from\ plasma}$$

Tungsten's chemistry results in a R value ranging from 0.95 up to unity when the tungsten PFC is

saturated with hydrogenic atoms [45]. A high recycling regime has benefits in terms of fuel retention, however similarly to neutral gas seeding the presence of cold neutrals in the plasma edge produces collisional cooling increasing the ITG and therefore the turbulent transport within the plasma.

A more extreme ITG further degrades reactor performance by increasing the risk of large edge localised modes (ELMs) that threaten to destroy the PFCs with immensely high heat flux far beyond the handling capabilities of tungsten PFCs, $10GWm^{-2}$ ELM events are predicted on ITER [46] [47]. Coenen [48]reported on macroscopic damage to tungsten tiles, surface melting and then recrystalising, in TEXTOR $45MWm^{-2}$, ASDEX-U $80MWm^{-2}$ and ALCATOR C-MOD $500MWm^{-2}$ exposed to ELMs showing the extreme damage that could be observed in the $\sim 20x$ higher magnitude events that could occur in ITER. Tungsten also exhibits issues with helium implantation at high temperatures. Under helium bombardment, even at energies well below the sputtering threshold, high temperature tungsten ($\approx 1000K$) forms a microscopic fuzz on it's surface that can be easily removed by wiping which leads to an increase in sputtering yield during plasma exposure [49]. This is clearly problematic as the formation of such fuzz could leak to a flux of tungsten to the core and a loss of confinement. Fuzz was observed in ALCATOR-CMOD with $100nm$ thick $400nm$ deep tendrils form on the tungsten surface [50], interestingly though no net negative effect was observed on plasma performance (minimal area coverage) and it is important to mention at this point that testing of a number of pre-made fuzz samples installed in DIII-D showed minimal damage to the vast majority though it was reasoned that the fuzz samples were more prone to arcing than smooth samples which did lead to tungsten dust ejection. This research led to a proposed maximum electron temperature that said samples can be exposed to of 10-30eV [51].

So what is the solution to the PFC issue if tungsten is not suitable? It is the opinion of the author that a complete paradigm shift is required with PFCs and that the utilisation of liquid metal PFCs offers solutions to the challenges. The first benefit therefore comes from a consistently flowing component thereby, presenting a constantly refreshing face to the plasma removing heat via convection and acting as a particle sink thus reducing the surface damage to the PFC reducing the cost both of replacing components and in downtime during maintenance. The most researched and strongest candidate for a liquid metal PFCs is lithium. Lithium is chosen as it is low-Z; as such has little effect on confinement when sputtered and it is also a strong chemical getter thereby cleaning the plasma through impurity removal [52]. Lithium pellet injection in TFTR produced a 55% increase in the triple product and an increased fusion power due to a reduction in the ion temperature gradient [53] [54].

Liquid lithium divertors also offer a natural defence against ELMs and transient events through an effect

known as 'vapor shielding.' When a transient event occurs the divertor region experiences a high heat flux increasing the surface temperature of the lithium layer leading to evaporation from the surface. This evaporated material forms a cloud of vapor above the PFC effectively detaching the plasma from the divertor protecting the PFC. This will also cool the plasma edge through collisions, once the edge temperature drops the vapor cloud is redeposited onto the plate allowing for normal operation to resume, obviously some lithium will penetrate the core but as discussed this will have a much lower effect on confinement than tungsten. The TFTR results highlighted that the major source of anomalous transport, transport that reduces the confinement and increase the risk of ELMs, is the Ion Temperature Gradient (ITG.) A reduction of the ITG clearly then will be beneficial to reactor operation and the question becomes how to maintain a hot edge of the plasma. Zakharov states simply that 'plasma stays hot if you do not cool it' [55]. The main cooling source at the edge arises from the flux of neutral atoms from the wall to the plasma (recycling) which collide with the hot ions and through a system of successive excitations and ionisations drain energy from the plasma, lowering the recycling coefficient R will therefore increase the edge temperature, decreasing the ITG and suppressing the anomalous transport within the plasma, Krasheninnikov [56] states in his paper on Lithium walls that 'plasma flux to the walls is governed by the recycling'. Lithium is the ideal candidate to achieve this low recycling regime due to its strong chemical affinity with hydrogen (Lithium has also been shown to be effective at pumping Helium ash within the device [57]) in the Experimental Advanced Superconducting Tokamak (EAST) it was shown that after an evaporate coating of lithium with an 85% wall coverage wall retention increased from 55% to 75% [58] clearly a flowing liquid metal divertor (assuming the majority of particle loss occurs here) will greatly increase retention as the lithium film will be pumped and as such will not saturate as quickly. Lithium therefore offers a completely different operating regime to the currently investigated high recycling low edge temperature offered by tungsten PFCs and the next paragraphs will outline the benefits of this novel approach.

In the limit that R tends to zero there is no influx of neutral atoms to the plasma therefore edge cooling is completely eliminated producing a flat temperature profile across the plasma in a regime known as the 'isothermal tokomak', the Lithium Tokamak Experiment (LTX) with evaporated lithium coatings ($\sim$ 200mg of lithium at a $\sim$ 100nm depth) on the lower divertor demonstrated a retention of $\sim$ 60 % of the injected hydrogen in the walls and produced a flat electron temperature profile across the plasma [59] highlighting that the zero recycling regime is accessible. It blatantly follows that a flat temperature profile will completely suppress the conductive loss of energy due to anomalous transport within the plasma causing a massive increase in the confinement time, LTX showed a 200% increase in confinement compared to the ohmic scaling law, and a mass reduction in the ELMs [59]. Increasing confinement reduces the auxiliary power

required to sustain a burning plasma, Zakharov [60] predicts that for JET in a zero recycling regime a Q factor around 5 could be achieved with an NBI power of around 3-4 MW a very modest value compared to the $\approx 70MW$ ITER will require to achieve the same Q factor [61]. A hot edge also allows for a much greater burning region within the plasma, ITER currently predicts a tritium burn fraction of .035% [62] which is an order of magnitude lower than the predicted fraction $\approx 8\%$ with $R = 0.5$ [60] . This regime also produces a much higher plasma beta (ratio of plasma to magnetic pressure), a 20% increase has been predicted in simulations [56]. This increase in plasma beta enables the Greenwald limit to be reached, experimentally shown in FTU through the application of the three capillary porous systems (CPS) [63]. The plasma beta ,β, is directly related to the fusion power, P_{fus} through the equation [64].

$$P_{fus}/V_P \propto < p >^2 \propto B_T^4 \beta^2 \tag{1.6}$$

Where V_P is the plasma volume, $< p >$ is the average plasma pressure and B_T is the toroidal field strength. One can see that a maximisation of the plasma beta is another method to produce high fusion powers without increasing magnetic field strength.

Edge conductivity increases with higher edge temperature producing an increase in plasma toroidal rotation (ExB shear) causing a reduction in the thermal diffusion of species [65] leading to an improvement in confinement [66]. This rotation of the plasma also satisfies the boundary condition for edge transport with MHD rather than requiring particle and energy ejection produced by ELMs [67] [67] giving rise to an operating regime known as the Quiescent H Mode characterised by high Greenwald fraction (>80 %) and low collisionality.

A hot edge does cause a concern: how will this effect the heat flux incident on our PFCs and will it be so extreme such that mass evaporation of lithium will be certain? The low recycling regime offers a number of protections to the PFC that should guard against this. Firstly, it is theorised that in the regime the ion heat flux will be independent of the edge temperature and will actually depend on the edge density, as the density gradient between the edge and the core will be driving the transport to the walls [60]. The second effect arises from the effect of the regime on the scrape off layer width, λ_q, it has been shown that this is proportional to the ion gyro-radius [68] ($\lambda_q \propto \rho_{ion} = \frac{mv}{qB}$). This shows that λ_q will scale with $T^{\frac{1}{2}}$, producing greatly increased widths in the low recycling regime. The low collisionality in the SOL will also lead to a large number of particles being trapped in the SOL ($\sim 80 - 90\%$ [69]) this extended confinement in the SOL is theorised to increase λ_q through turbulent broadening [70].

The use of lithium does present a number of problems to operation. Concerns are raised over the low vapor pressure of lithium it is theorised that mass evaporation, where Li influx from the plate is greater

than the supply, could occur leaving the solid substrate underneath exposed to the plasma. This worry has lead to research has led to study of Sn-Li compounds due to it's higher vapor pressure, coming at a cost to the gettering ability of the surface and therefore access to the low recycling regime however. This low vapor pressure also means that the plate temperature must be kept below 450^oC for the low recycling regime to be achieved, this requires novel cooling techniques to maintain this surface temperature. A similar concern to evaporation is macroscopic ejection of lithium via fluid instabilities that could lead to the extinguishing of the plasma, solutions to this proposed by research at UIUC are outlined in the section on the LiMIT design. Pumping of such a divertor also poses large engineering difficulties, the lithium will experience drag when pumped across magnetic field lines due to MHD. This MHD drag force is proportional to the toroidal magnetic field squared ($F_{drag} \propto B_T^2$), as the EM pumping is proportional to the toroidal field showing that the flow will be hindered by a inverse relationship with the massive toroidal field requiring that a massive current be driven in order to pump the PFC which will add another source of cost to the reactor. Recently a new concept Magnetically Guided Liquid Metal Divertor (MAGLIMD) in which the liquid metal is pumped along the broken field lines in the SOL has been outlined [71] to suppress the MHD drag effect on pumping.

1.4 Current Technology and Results with Lithium PFCs

1.4.1 Slow Flow

The CPS is a slow flow PFC that consists of a porous capillary mesh above a lithium reservoir. When the surface is heated the lithium in the reservoir flows up the pores to the surface via capillary action presenting a lithium face to the plasma (an SEM image of a wet and unwet CPS system is shown in figure 1.4 [72].) A CPS limiter has been shown withstand heat fluxes of $10 MW m^{-2}$ in T-IIm without any sustained damage, decrease deuterium recycling and increase helium gettering [73][74]. A test in a linear plasma device showed the system withstand a peak heat flux of 25 $MW m^{-2}$ far in excess of the ITER limits [74].

The CPS system is not without its flaws however: firstly in order to wet the mesh the CPS must be heated to very high temperatures of around 600-700^oC [75] for lithium and $\sim 1000^oC$ for tin [76]. The second issue is that there is no method of impurity or fuel removal from this static face of lithium leading to the lithium surface becoming saturated during long term operation. Impurity build up on the surface leads to blocking of pores preventing full lithium coverage on the surface and the lack of fuel retention/ability to flow lithium out of the device and recycling the fuel limits the lifetime of such a device.

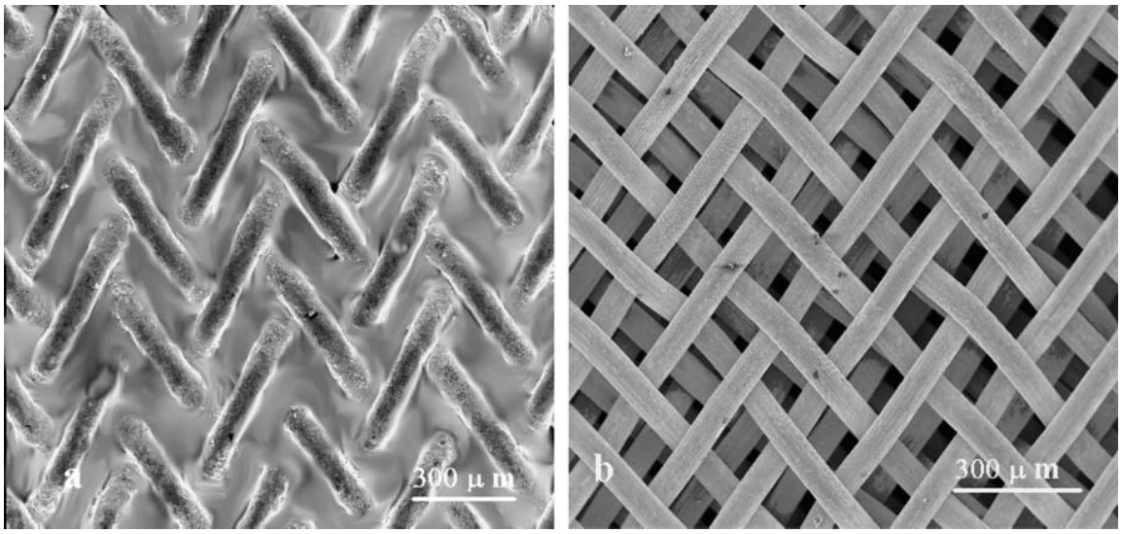

Figure 1.4: SEM image of a molybdenum CPS system. With a wetted lithium mesh 1.4 a and an unwet mesh 1.4 b

1.4.2 Medium Flow

Medium flow systems are characterised by flow velocities of around $0.1 - 100 cms^{-1}$. This speed enables impurities and fuel to be removed from the lithium surface presenting a constantly refreshing face to plasma however, it is not fast enough to enable for heat removal by lithium convection meaning that such PFCs must have a suitable backing material and cooling system to handle the majority of the heat flux from the plasma. Two medium flow systems will be discussed here FLiLi and LiMIT.

Figure 1.5 shows the basic design of a FLiLi PFC. A lithium reservoir is filled prior to experimentation, JxB pumps are then used to drive lithium flow up the feeding pipes and into the distribution box from which it is spread uniformly across a flat plate flowing down due to gravity back to the reservoir where the process repeats. Behind the front plate are installed cooling channels, currently supplied with helium gas, to aid heat removal from the plate.

Three generations of the FLiLi limiter have been tested in the EAST tokomak and have shown a reduction in ELMs with increasing lithium exposure, an increase in the confinement time of the plasma with a FLiLi type plate and a reduction of the D_α signal a sign that the recycling within the device has been reduced [7][8][9][77][78][79].

The LiMIT design is identical to the FLiLi design but its front plate consists of a number of narrow shallow trenches ($\sim mm$ deep and wide.) These trenches enable a thermoelectric current to flow along their

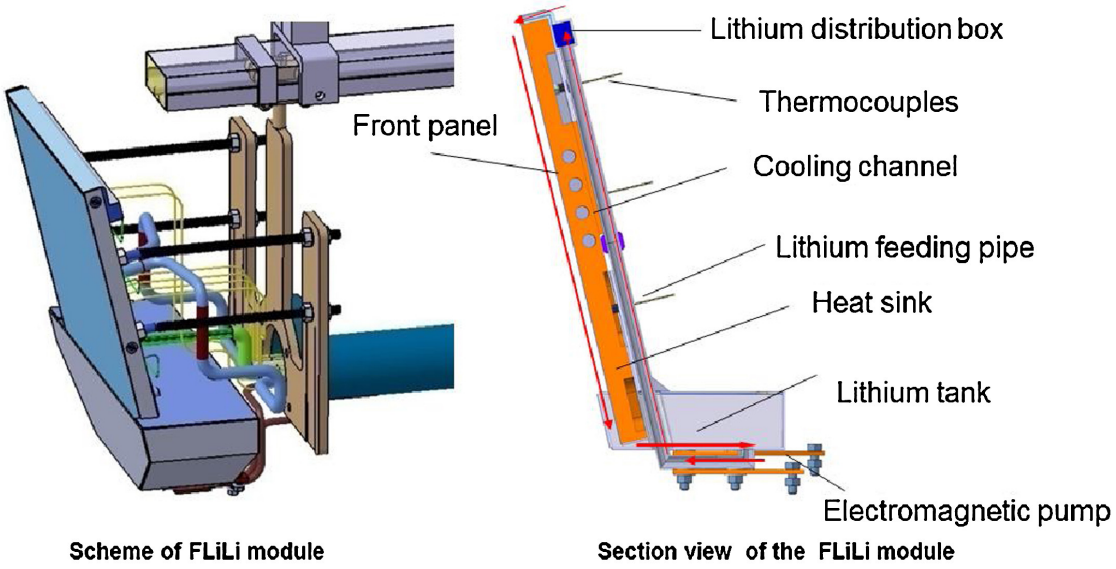

Figure 1.5: Basic design of a FLiLi type PFC. Lithium is pumped from the reservoir to a distribution box on the top of the plate it then flows under gravity back into the reservoir and the process repeats. [4]

boundary which when crossed with a toroidal field produces a JxB force passively pumping lithium down the plate, this produced velocities in excess of $20cms^{-1}$ to be reached [2]. The trenched design also limits the droplet eject due to the high surface tension of lithium and the narrow trenched design. A more in depth outline of the LiMIT design can be found in Section 2.2.

1.4.3 Fast FLow

Recently fast flow (1-$20ms^{-1}$) [80] lithium PFCs are beginning to be developed. Faster flow has a couple of benefits: firstly it reduces the lithium surface temperature allowing for better access to the low recycling regime alongside this it also utilises lithium as the source of the heat removal without relying on the solid plate and cooling beneath the lithium samples. No fast flow PFCs have been tested in a fusion reactor but a new test bed is being developed in PPPL known as FLIT to begin testing a full fast flowing system under fusion relevant magnetic fields.

1.5 Thesis Overview

To further the development of liquid lithium technologies a LiMIT type limiter was exposed to the EAST plasma allowing for the plate's temperature response to be studied under fusion relevant heat fluxes. Within chapter 2 the design of the LiMIT PFC will be discussed alongside the experimental setup in EAST, chapter 3 then talks of the various methods of heat handling available to LiMIT, chapters 3-4 will present a interpretive

analysis tool created within COMSOL and chapter 5 will touch on future experimental work at UIUC based on the EAST results.

Chapter 2

LiMIT Plate Design and Experimental Setup

2.1 Thermo-Electric MagnetoHydrodynamics

TEMHD theory in relation to fusion was first theorised by Shercliff [81], he proposds a flow that arises from the thermo-electric effect. When two dissimilar metals share a boundary with a temperature gradient along it a potential difference between the top and the bottom of the boundary driving a current along it. When this thermo-electrically driven current is combined with a perpendicular magnetic field a $\vec{J}x\vec{B}$ force causing flow perpendicular to both occurs provided one of the metals is liquified and contact between the surfaces is maintained. The magnitude of the current driven depends on the difference in Seebeck coefficients (S) between the two metals as shown by the modified ohms law:

$$\frac{J}{\sigma} = \vec{E} + \vec{v}x\vec{B} - S\nabla T \tag{2.1}$$

A figure showing the absolute Seebeck coefficients for various metals can be found in 2.1. The plot shows that lithium is an outlier with a high positive positive value (especially in a liquid state) making it a prime candidate for TEMHD driven flow, if combined with a metal with a negative Seebeck coefficient (such as stainless steel) a sizeable current will run through the lithium film to drive flow. Ultimately the higher the difference in Seebeck coefficients the faster the flow is able to be driven in the liquid medium. Unfortunately, after Shercliffs paper in 1961 TEMHD in fusion applications was widely forgotten/ignored. That is until Jaworski [82] noticed swirling of liquid lithium during exposure to an e-beam and connected this to the formation of thermo-electric currents in the lithium, this lead to a multi-year CPMI effort to produce a PFC that utilises this effect and this effort produced the LiMIT design.

2.2 LiMIT Design

The LiMIT design is shown in figure 2.2. The design consists of a series of narrow and shallow trenches ($\sim mm$). When a heat strike is applied to the lithium surface a temperature gradient is present down the

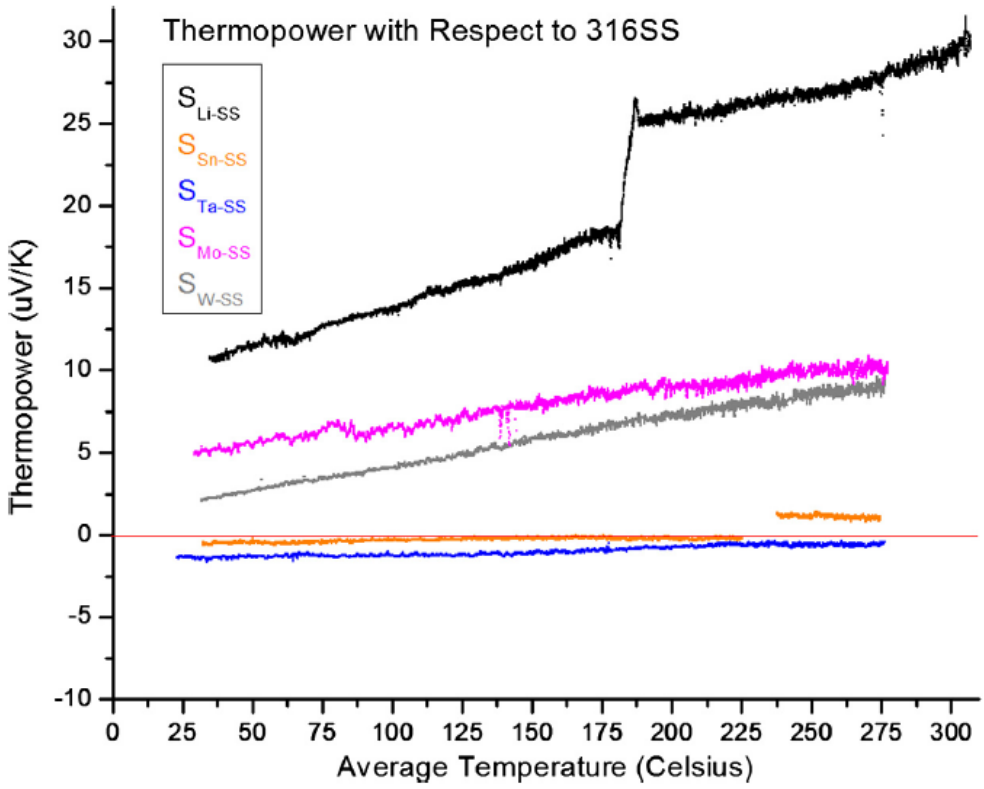

Figure 2.1: Figure showing the absolute Seebeck coefficients for various metals compared to 316-SS. Note the high positive value of lithium and its increase once lithium is liquified. [5]

trench, this is further amplified by the addition of cooling channels in the back of the plate, this drives a current in the lithium in the same direction along the trench boundary when a magnetic field is applied across the plate the crossed current and magnetic field drive lithium flow down the plate. The LiMIT concept has been thoroughly studied at UIUC with the ability to sustain flow with the plate inverted [83], flow velocities greater than $20cms^{-1}$ and heat handling capabilities of $10MWm^{-2}$ under electron beam exposure highlighted [84] [85] [86]. Testing has also been performed within global devices: within HT-7 though the experiments were hampered by wetting issues a flow velocity of $3.7cms^{-1}$ due to TEMHD was measured [87] and exposure to the Magnum PSI plasma ($3MWm^{-2}$ heat flux 0.3T magnetic field) produced velocities of $\sim 60cms^{-1}$ on the plate (though issues with lithium circulation lead to the plate sustaining heat damage ending the experimental campaign.) [88]

The trench design does present one key issue, in a phenomena known as dry-out highlighted in figure 2.3. When an uneven heat strike is present across the LiMIT plate the temperature gradient varies with position on the plate, clearly the area under the peak of the gaussian shown on the figure will have the

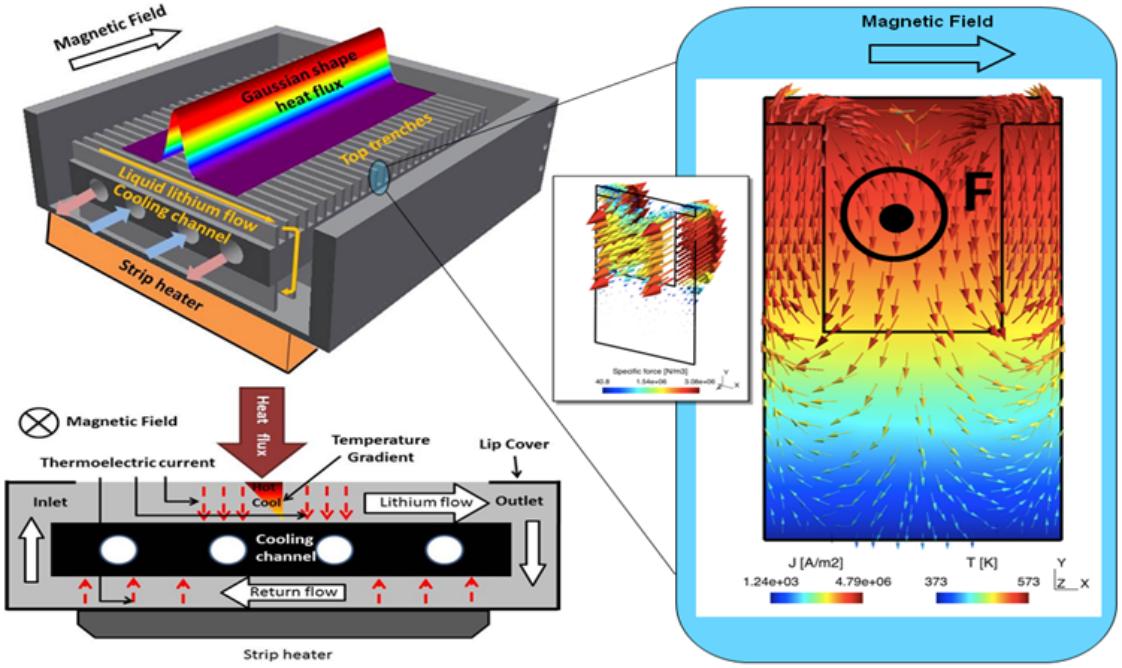

Figure 2.2: Figure showing the LiMIT design concept alongside a description of the TEMHD flow produced by the trenched design. A temperature gradient along the trench liquid metal boundary induces a current in this direction which induces a flow when a crossed magnetic field is applied.

largest temperature gradient across the trench. The lithium situated under the peak flux will therefore have a higher velocity, this leads to the lithium film thinning in this region and causes a 'pile-up' of lithium downstream. This can have catastrophic consequences for a PFC as it can expose the plate material to the plasma which will: firstly lose the benefits of the low recycling regime and secondly can lead to the plate suffering heat damage (as shown by electron beam exposure at UIUC [6].) Research at UIUC has displayed that the application of 3D order foams can mitigate this dry-out by allowing lithium flow between channels ('cross talk'.)

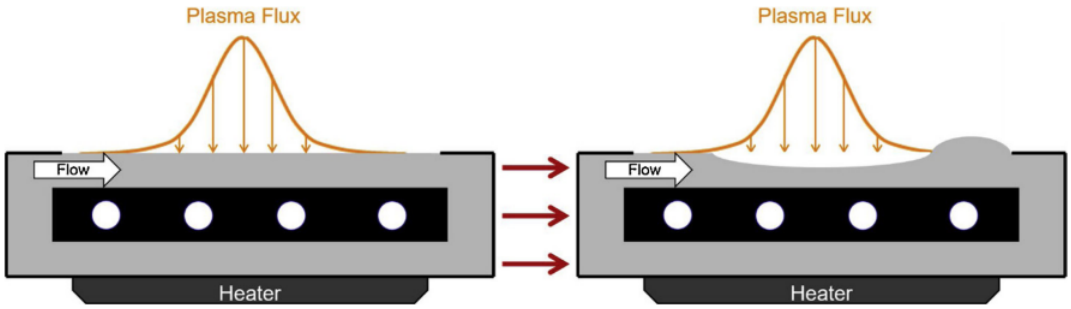

Figure 2.3: Figure showing how a gaussian heat flux leads to dryout in the area of the highest area of the heat strike causing lithium pile up down-stream [6]

2.3 Experimental Setup

Pictures of the front and back of the TZM LiMIT plate can be found in figure 2.5, 316-L Stainless Steel cooling lines have been pressed into the back of the plate to enable helium cooling to promote TEMHD flow. To improve thermal conductivity the gap between the lines and the plate is filled with a soldering alloy PdAgCu (composed of 25.1% Palladium, 20% Copper and the 54.9% Silver.) The plate has 2mm wide and 1mm deep trenches machined onto its 320mm x 298mm face. To achieve an even flow of lithium on the plate a distributor was bolted onto the top of the plate, shown in figure 2.6,this consists of a vast number of narrow full channels designed to achieve a uniform flow along the plate. Lithium is loaded into the main reservoir beneath the plate from here two EM pumps, operating at 100Amps, push the lithium into the reservoir at the back of the divertor, once this reservoir is full the lithium wicks up the vertical flow channels within the distributor and out of the narrow pinholes onto the plate. The lithium then flows down the plate driven by both TEMHD and gravitational flows and back into the main reservoir. There are two main diagnostics installed with the plate: two TZM Langmuir probes that are positioned either side of the plate and a set of fourteen TCs. A diagram highlighting the position of the TCs can be found in figure 2.7: TCs 12 and 15 are hooked up to the input and output of the cooling lines respectively, TC 14 is on the distributor, TC 7 is in the collector and the rest are positioned 2mm below the surface of the plate.

Globally EAST has a wide selection of diagnostics. This analysis will mainly focus on using data taken from the diamagnetic coils (stored plasma energy W_{mhd},) the interferometer (line average n_e on a chord at R=1.82m,) spectrometers positioned to study the upper and lower divertors as well as the midplane and finally a bolometer to calculate the total power radiated from the plasma. The LiMIT plate was installed on the transfer arm attached to the Material and Plasma Evaluation System (MAPES) allowing for the insertion and position of the plate through the H-port in EAST ($\phi = 292.5°$) the plate position toroidally is shown in figure 2.4, the toroidal position and the alignment to the magnetic field was checked prior to the experiment using a laser measurement system. Once inside the vacuum vessel LiMIT was baked out for 24 hours at a temperature of $\sim 350^oC$ it was then retracted into the MAPES chamber and 350g of liquid Li was loaded into the reservoir in an argon atmosphere. After loading the plate was re-inserted for testing, the run schedule was broken into five main sections: initial shots to determine optimum operating conditions and to obtain a high confinement plasma, a sweep of the plate's helium cooling pressure from 0-3MPa, a sweep of the RF auxiliary heating power from 2.9MW to 3.4MW (RF heating was provided by two ECRH and two LHW devices,) a study of the radial position of the limiter ranging from R=2.35m to R=2.31m (seperatrix positioned at $R \sim 2.385m$) and finally a study of NBI heating with total heating power reaching a maximum of 7.9MW looking to examine the maximum heat handling capabilities of LiMIT. Too allow for

a conclusive study of the effect on the plasma due to LiMIT the usual lithium coating run to condition the walls in EAST prior to the shots was not performed .

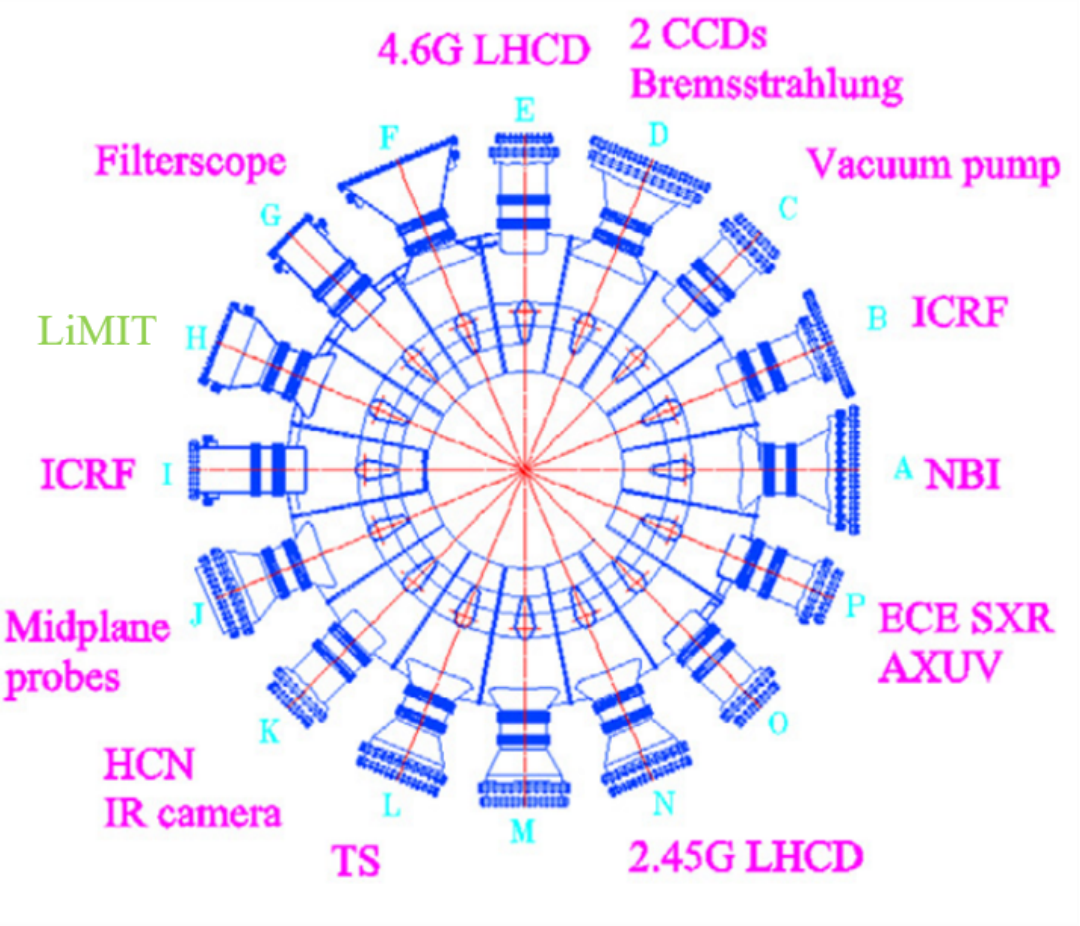

Figure 2.4: Toroidal diagram of EAST highlighting the plates position within the torus.

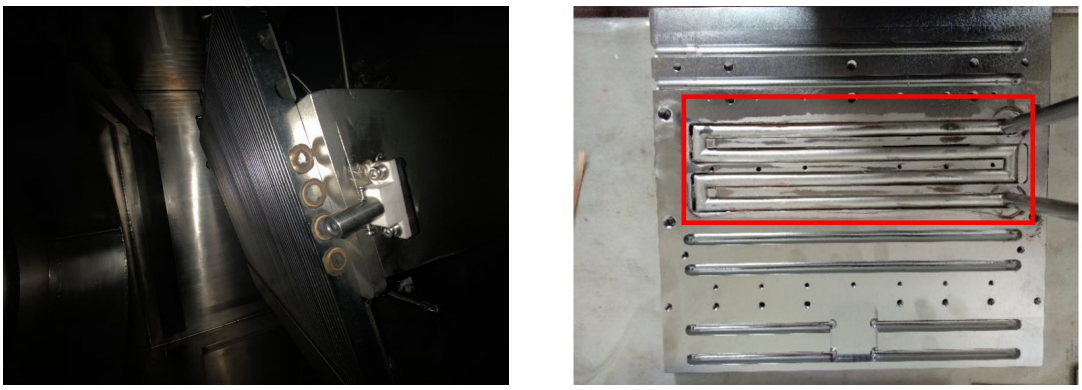

(a) Plate Front (b) Plate Back

Figure 2.5: Photos of the front and the back of the LiMIT plate prior to plasma exposure. Cooling lines are pressed into the back of the plate and thermal conductivity was improved between the two via the use of a soldering alloy PdAgCu and slots are cut into the back for the insertion of heaters aimed to maintain limiter temperature at $350 - 400^oC$. The plate front consists of 2mm wide 1mm deep trenches with a distributor clamped on top by TZM clips. To measure electron and ion temperature and density at the plate two langmuir probes in TZM housing flank the module.

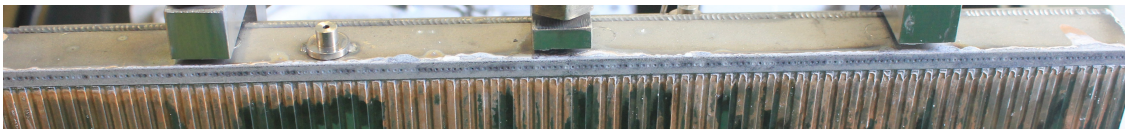

Figure 2.6: Figure showing distributor design for LiMIT plate. Lithium flows into the back of the distributor and fills a reservoir in the module once full, lithium wicks up and seeps from the holes in the distributor.

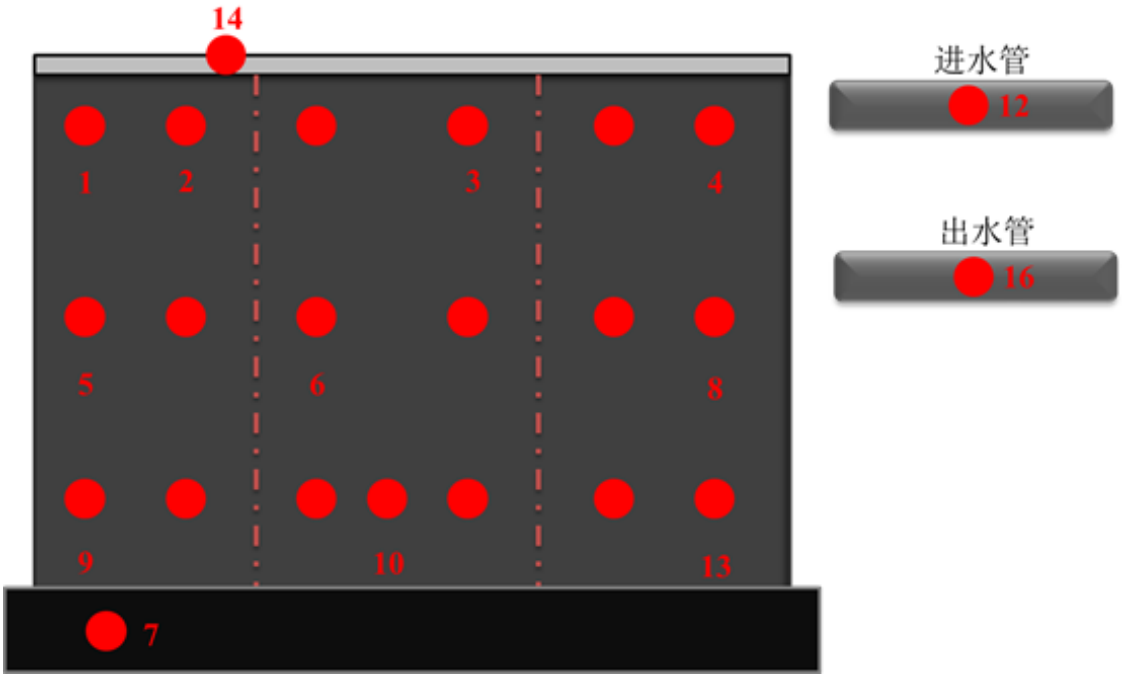

Figure 2.7: Thermocouple position within the plate. TCs 12 and 16 are located on the cooling line inlet and outlet respectively, TC 14 is positioned on the distributor, TC7 is on the reservoir and the rest are positioned 2mm below the surface of the limiter with the left hand side being on the ion side and right the electron.

Chapter 3

LiMIT Power Handling

3.1 Mechanisms for Heat Exhaustion

Three main mechanisms for power loss due to the liquid lithium are determined as follows: power dissipated by the formation of and collisions with the lithium vapour cloud (Q_{vap}), heat stored via convection within the lithium (Q_{conv}) and heat that is conducted into the TZM back plate (Q_{TZM}). These three factors can be summed to give an equation for the total heat flux absorbed by LiMIT

$$Q_{plasma} = Q_{vap} + Q_{conv} + Q_{TZM} \tag{3.1}$$

A value for the heat conducted into the TZM plate is obtained using the interpretive analysis tool outlined in chapter 4. The two process (Q_{vap} and Q_{conv}) of heat dissipation by the lithium layer itself will be discussed in the subsequent sections.

3.1.1 Vapor Shielding

Rindt [89] [90] outlined an equation for the power dissipated due to the formation of a lithium vapor shield in a plasma given by:

$$Q_{vap} = \Gamma_{vap}(1 - R)(\epsilon_{cool} + E_{vap}) \tag{3.2}$$

$E_{vap} = 1.41eV$ [89] is simply the energy of evaporation for lithium. The more interesting term is ϵ_{cool}, this is the average energy lost by lithium atoms entering the SOL; modelling work in [91] and [92] has shown that this is dependent on electron temperature T_e, electron density n_e and the confinement time of lithium in the SOL τ (assuming that the majority of energy loss will come from inelastic collisions.) Clearly T_e and n_e will determine the collisionality of the SOL and the longer the lithium is confined the more subsequent ionisation and recombination events can occur increasing the energy dissipation. Using the simulation work described and the parameters of the EAST plasma during the LiMIT shots an $\epsilon_{cool} = 5eV$ was assumed for

the vapor shielding calculations. Armed with the energy losses for an individual lithium atom one now must consider the flux of lithium atoms entering the scrape of layer, Γ_{vap} is the evaporated flux of lithium from the liquid surface, note that the sputtering of lithium ions has been ignored as the majority of the sputter lithium escapes the surfaces as ions and will be promptly redeposited [93] .The evaporative flux can be found using the Langmuir evaporation law [94]:

$$\Gamma_{vap} = \frac{p_{Li}}{\sqrt{2\pi m_{Li} k_b T_s}} \tag{3.3}$$

Where T_s is the temperature of the lithium surface, m_{Li} is the mass of lithium $6.941amu$ and p_{Li} is the vapour pressure of lithium which can obtained using the two-term vapour pressure equation [95]:

$$log_{10}(p_{Li}(Pa)) = 10.061 - \frac{8023}{T(K)} \tag{3.4}$$

Not all lithium evaporated from the surface will enter the SOL [96] shows that lithium that is ionised close to the lithium surface will promptly be redeposited on the plate and as such no energy will have been lost from the system; to account for this a redeposition factor (R) is included in the power balance.

3.1.2 Re-Deposition Coefficient

It is prudent when looking at the Re-Deposition coefficient to consider the ionisation lengths λ_{ion} of lithium atoms and the larmor radii ρ_{Li^+} of Li^+ ions [97], here higher order ionised states of lithium can be ignored as it is assumed that once lithium is ionised it will be redeposited. If $\lambda_{ion} \leq \rho_{Li^+}$ then lithium atoms are ionised near the surface and will redeposit prior to completing a full gyration. If $\lambda_{ion} > \rho_{Li^+}$ two main developments are expected: lithium will back scatter off other evaporated particles leading to redeposition at another point of the plate or lithium atoms escape into the SOL dissipating power. The lithium ionisation length is given by [98]:

$$\lambda_{ion} = v_{Li}(\langle \sigma v \rangle n_e)^{-1} \tag{3.5}$$

Where v_{Li} is the velocity of the lithium ions to get an idea for this value lithium atoms are assumed to be evaporated with a temperature equal to the surface temperature of the liquid. $\langle \sigma v \rangle$ is the rate coefficient for ionisation calculated using T_e above the plate. Values for T_e and n_e are obtained from the LP data for the shot. Huba [99] gives a formulation for the Larmor radius.

$$\rho_{Li^+} = 102(\mu.T_i)^{\frac{1}{2}}(ZB(G))^{-1} \tag{3.6}$$

μ is the mass of lithium in amu (6.981), T_i is the ion temperature in eV estimated as discussed above, Z is the charge state of Lithium, assumed to be one as higher order ionised states will follow tighter Larmor orbits as such if lithium is deposited in the +1 charge state it is unlikely to be at higher orders and B will be 25000G to match the toroidal field in EAST. Once the ratio is calculated a value much smaller the redepostion factor can be calculated using the equation:

$$R = \frac{1}{1 + (\frac{\lambda_{ion}}{\rho_{Li}}^2)} \tag{3.7}$$

3.2 Convective Power Losses

Ruzic [84] in the initial outline of the LiMIT concept uses a 2D model to give an equation for the heat stored convectively in a lithium surface:

$$Q_{conv} = \rho C_p(\frac{1}{2}\frac{dT}{dy}h)hw\bar{u} \tag{3.8}$$

Where ρ is the density of lithium ($512 kgm^{-3}$), C_p is the heat capacity of lithium at constant pressure $4349 JK^{-1}kg^{-1}$ [75],$\frac{dT}{dy}$ is the temperature difference across a LiMIT trench (calculated via the difference in the infra-red surface temperature and that measured by the TCs in the TZM back plate), h and w are the height and width of the trenches respectively (both $0.5mm$) and $\bar{u}$ is the average velocity of lithium.

The average velocity of the lithium is also obtained using the 2D model following the method outlined by Shercliff and applying current conservation and Kirchoff's law to give [84]:

$$\bar{u} = \frac{Ha - tanh(Ha)}{Ha + Ctanh(Ha)}(\frac{s}{B}\frac{dT}{dY} - \frac{1+C}{\sigma B^2}\frac{dP}{dZ}) \tag{3.9}$$

Where s is the Seebeck coefficient for lithium ($25 \mu V K^{-1}$ [SURLA 2011]), B is the EAST toroidal field, Ha is the Hartmann number (ratio of electromagnetic force to viscous force) given as $Bw\sqrt{\frac{\sigma}{\mu}}$ where σ and μ are the conductivity and the dynamic viscosity of lithium respectively, C is defined as $C = \frac{w\sigma}{t\sigma_{TZM}}$ where t is the thickness of the TZM wall and σ_{TZM} is its conductivity and $\frac{dP}{dz}$ is the pressure change from the distributor to the reservoir (i.e across the plate) and is assumed to be equal to the EM pumping pressure (viscous forces have been ignored as they are infinitesimal) $P_{pump} = \frac{JB}{s}$ with a linear drop along the plate.

Chapter 4

COMSOL SIMULATIONS

4.1 Initial Problem Setup

As an extension to the experimental results obtained from the exposure of the LiMIT plate to EAST plasma an interpretive analysis tool has been created in COMSOL Multiphysics allowing for the heat flux incident on the plate to be determined. The setup of the domain can be found in figure 4.1 the model was constructed within in Inventor and then imported into COMSOL for the simulations

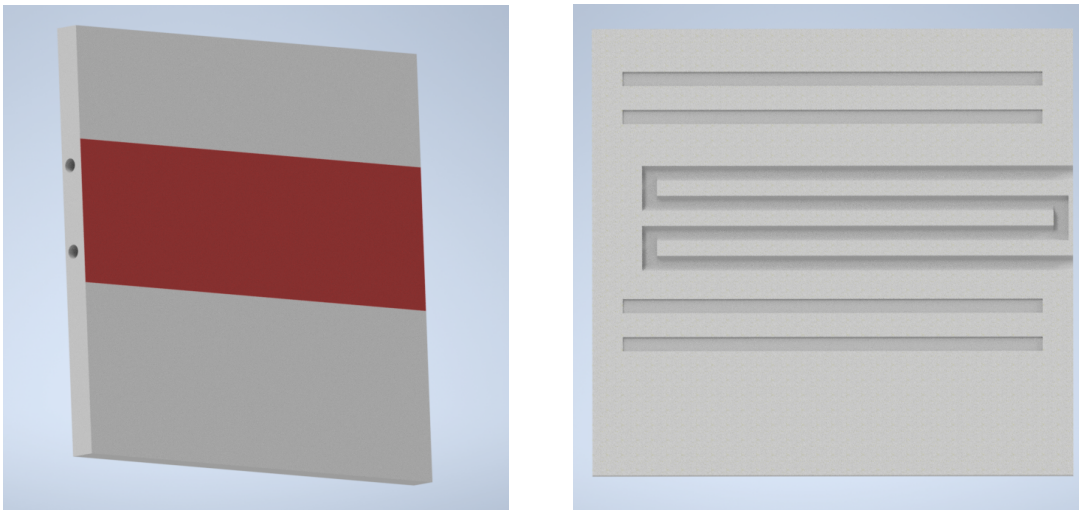

(a) Plate Front (b) Plate Back

Figure 4.1: Domain setup for the COMSOL simulations, based on simplified FLiLi design from Princeton. Figure 4.1a is the plate front with the area of plasma contact highlighted in red and 4.1b is a cut profile of the back of the plate displaying the snaked cooling lines and the four heater slots. A FLiLi-like design was chose to ease computational cost associated with the more complex mesh required for the LiMIT geometry.

The model was based off drawings from Princeton for the FLiLi Gen III plate. The decision to simulate a FLiLi type plate rather than a LiMIT design was made as the vast number of narrow shallow trenches in the LiMIT plate means that the geometry is far more complex and as such requires a better refined mesh greatly increasing computation with very little difference in results. The domain has 4 locations for heaters in the back and a snaked cooling line embedded below the region that will be struck by the plasma, the

Table 4.1: Key Parameters for shot 95058.

Shot #	Distance from separatrix (cm)	Average Limiter Temperature (^{o}C)	Auxiliary Heating Power (MW)	Helium Cooling Pressure (MPa)	Line averaged n_e ($10^{19}m^{-3}$)	Plasma Energy, W_{mhd} (kJ)
95058	3	400	3.4	1	4.175	139

plasma heat strike region (highlighted in red on the figure) was assumed to be rectangular area centred on the cooling lines and constant over across a region 2.5cm either side of the profile. The plate was set as TZM and the cooling gas as Helium. A coupled model was created that used a turbulent flow level set module to simulate the helium flow within the cooling pipes and a heat transfer module to calculate the heat flow between the plasma, the plate and the cooling lines.

A time dependant solver was used over a 100 second window, so chosen to match with experimental TC data, the entire domain was set initially to match the experimental temperature and was assumed to be constant across the plate, the Helium cooling was turned on at 45s and ramped up to the desired pressure, plasma contact occurs in a window between 55-65s the heat flux on the plate rose to the set value over two seconds stays at this value for a further eight seconds and finally drops over the final two seconds as to replicate the EAST ramp-up and ramp-down of the plasma. To accurately compare simulation results with experimental results 3D cut points were included at the location of the experimental TCs, this allows for plots of temperature against time to be produced for the simulation at these points giving a direct comparison of the two profiles. As the heat flux (in Wm^{-2}) is a parameter fed into the simulation, matching the temperature profiles between the simulation and experimental TCs will give the experimental heat flux incident on LiMIT during its exposure. Integrating this over the total area of the heat strike allows for the power absorbed by the plate to be determined allowing for the extrapolation to divertor relevant powers and the study of lithium PFCs in these conditions.

To begin the simulations shot 95058 was chosen as shot to develop the model on, shot parameters shown in 4.1, as such Helium cooling pressure was set at 1MPa, the initial plate temperature was set to $400°C$ and an initial guess of the heat strike was $1MWm^{-2}$.

4.1.1 Initial Results

Initial comparisons of the central line TCs can be found in figure 4.2. The comparison of the central line TCs clearly shows that the cooling rate in the simulation is far too high. The first 10s of cooling TC5 shows a ΔT of 350^oC for the simulation and 5^oC for the experiment. The first problem with this model is that

pressure values from EAST are recorded from a regulator on the Helium gas bottle and not at the plate inlet due to the long gas pipes present with the MAPES system the pressure difference across the plate cooling lines will be far lower. To rectify this mistake, pipe length was factored into the simulation by assuming 10m of piping with a linear pressure drop between both the gas bottle and the inlet and the outlet and the exhaust. A second problem was identified with the geometric design of the module; due to a break in the braising the cooling lines had to be cut out of the plate for repair. When the pipes where reinstalled they were pressed into the groves left by the cut with thermal contact between the plate aided by a soldering alloy PdAgCu (composed of 25.1% Palladium, 20% Copper and the 54.9% Silver.) As such it These realisations culminated in a complete redesign of the model.

4.1.2 Project Redesign

The redesign of the COMSOL domain can be found in 4.3. Two major chances have been made in the re-designed model firstly only half of the cooling tube is now in thermal contact with the plate greatly reducing the area for cooling and the pipes are now modelled as 316-L stainless steel with a non-negligible thickness as it was assumed that the time taken for conduction through these pipes would reduce the cooling rate. All other major parts of the COMSOL simulation were unchanged.

Both models were run with the input parameters analogous to Shot 95058 from the EAST run. The temperature profiles for the three central line TC data can be found in figure 4.4 for both the new geometry and the experimental results.

The simulation data shows a marked decrease in the cooling rate in the new model with a temperature drop on the ion side of the plate now of $\approx 20^oC$ which is a marked improvement over the initial model (350^oC drop). A major issue remains however; the experimental TCs display changing temperature profiles across the central TCs with a far higher temperature response on the ion side of the plate whereas the simulation data show produces near identical profiles across the centre, with the cooling pipe geometry producing the slight variation.

To elucidate what causes the model deviation, the surface temperature change over the plasma exposure window was measured for a shot with identical auxiliary heating and plate position compared to 95058 but without helium cooling. The absence of helium cooling means that none of the temperature response can be attributed to the cooling and as such is solely due to the interaction between the plasma and the plate. It is apparent from figure 4.5a that the ion (left hand) side of the plate experiences the greatest temperature rise highlighting that the majority of the heat flux is concentrated here, there is then a moderate rise on the electron side and very little temperature response in the centre. In Zuo et al [7] a similar trend is noticed for

(a)

Ion Side

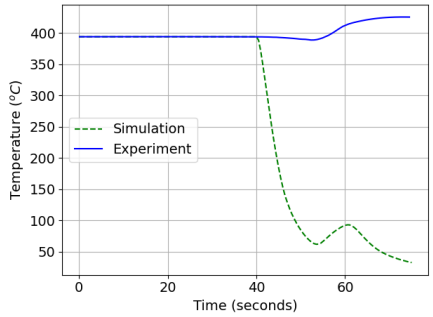

(b)

Center

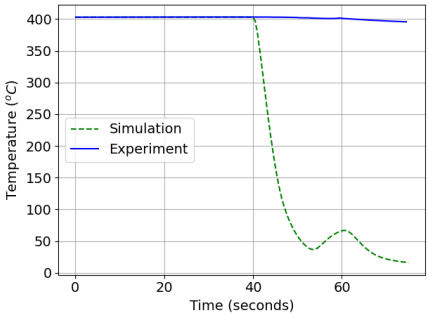

(c)

Electron Side

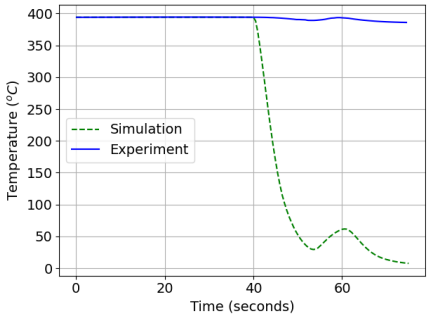

Figure 4.2: Comparison of central profile TC traces from the experiment (shot 95058) and the initial simulation. Helium cooling run at 1MPa and a gas temperature of 293K, Heat strike $1MWm^{-2}$ and the initial temperature was set at $400°C$. Figure shows profiles for the ion side 4.2a, centre 4.2b and electron side 4.2c for the thermocouples located under the heat strike. The simulation shows a far increased cooling rate with a ΔT of 350^oC compared to 5^oC, due to a too high pressure difference across the cooling pipes, too low a gas temperature and finally a difference in cooling geometry.

the Gen II FLiLi plate, temperature change over a shot from this paper is shown in figure 4.5b. This points to the presence of a localised heat flux on the plate and invalidates the assumption of a constant rectangular heat stripe across the plate.

Two theories are proposed for the uneven central heat profile: firstly that the plate was miss-aligned due to a fault with the installation that meant when both plates were inserted into EAST the ion side was tilted

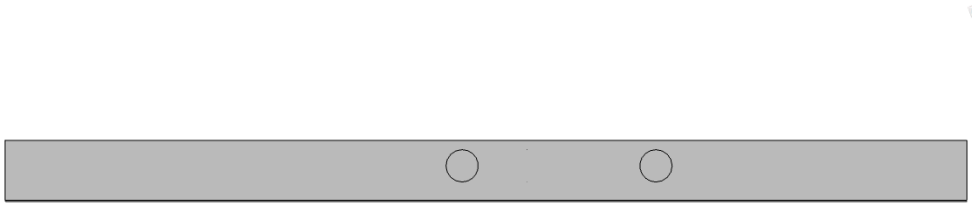

(a) Old Model

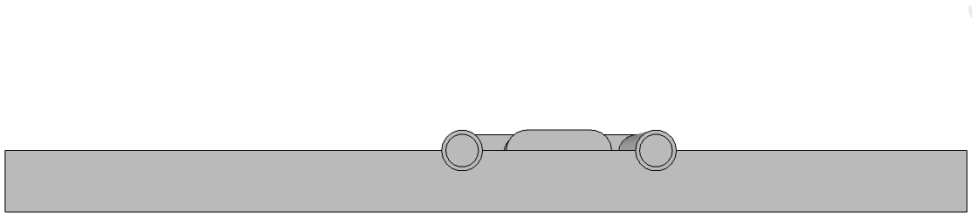

(b) Redesigned Model

Figure 4.3: Comparison between the two different cooling pipe designs. The new model has reduced thermal contact between the cooling pipes and the plate and the pipes now have a non-negeligible thickness and are set as 316-L stainless steel to further hinder heat transport.

towards the plasma and hence faced the bulk of the heat flux. An issue with this theory is the presence of a second smaller heat strike on the electron side; if the plate was tilted towards the plasma on the ion side it would shadow the entire plate from the plasma and one would expect the electron side to therefore display the lowest temperature response. The second explanation arises due to the curvature of the field lines. As the plate is flat when the centre of the plate is aligned with the toroidal field the field lines will be curved at the edge of the plate. This is important as it means that a component of the parallel heat flux impinges on the edge of the plate, as $q_{\parallel} >> q_{\perp}$ this means that the heat stripe is concentrated on either edge, one due to the parallel flux of electrons and the other due to parallel ions. The larger gyro-radius of ions means they can drift further from the field lines increasing the number incident on the plate leading to a more intense heat strike.

From this analysis it is clear that modelling the heat strike as a constant over the entire central profile is incorrect and that the heat flux is localised at either side of the plate. To rectify this a new heat strikes were defined on either side of the plate, shown in figure 4.6. Both are identical sizes and have a dimension of 5cm across the plate and 9.5cm vertically, these values were determined by studying the area of dryout

(a)

Ion Side

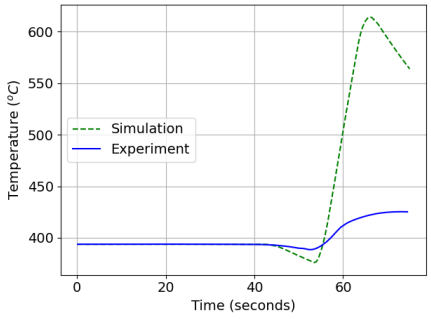

(b)

Center

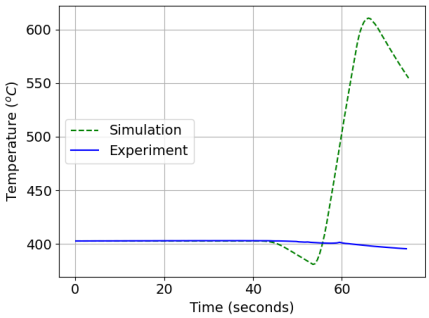

(c)

Electron Side

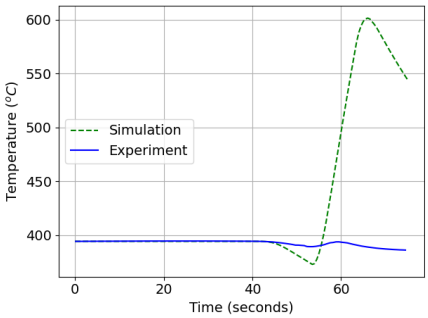

Figure 4.4: Comparison of TC traces from the experiment (shot 95058) and the analogous simulation. Helium cooling run at 1MPa with a gas temperature of 350^oC, Heat strike $1MWm^{-2}$ and the initial temperature was set at $400°C$. Figure shows profiles for ion side (4.4a), central (4.4b) and electron side (4.4c.) The simulation now displays a more reasonable cooling rate however all three simulated profiles are homogeneous whereas the experimental profiles differ based on plate position highlighting that the assumption of a constant rectangular heat strike is not valid.

shown in post-mortem photos of LiMIT.

Plots showing the central-line profiles for the new-heat strikes can be found in figure 4.7. These simulations were ran with an Ion side heat flux of $1.5MWm^{-2}$, electron heat flux of $.2MWm^{-2}$. The plots show

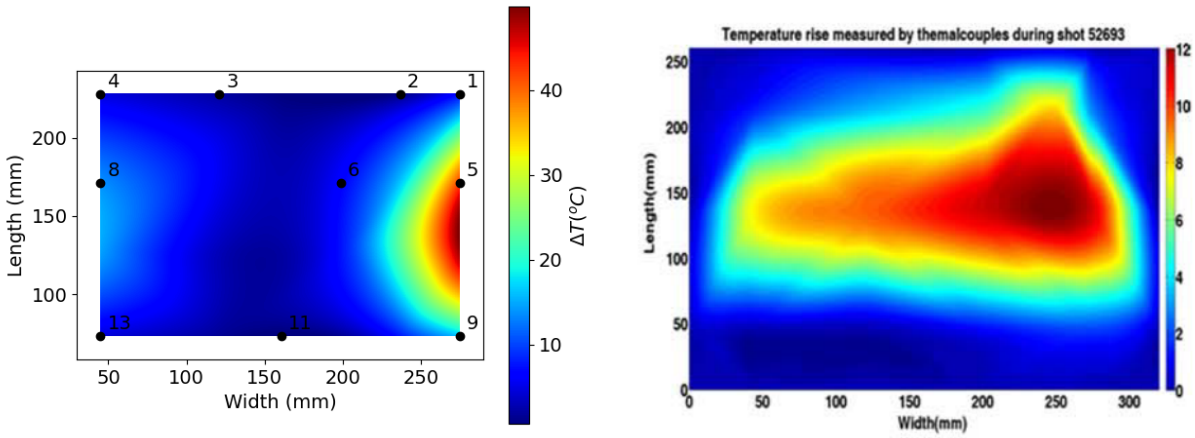

(a) (b)

Figure 4.5: Temperature change during plasma exposure for shot 95056 figure 4.5a and for the Gen II FLiLi 4.5b [7]. The figure faces the LiMIT plate head on: i.e ion-side of the plate is on the right hand side of the image and the electron side on the left. Figure 4.5a was created using a cubic interpolation of the temperatures measured at the points highlighted on the plot. Surface plots both indicated localisation of the strike points to the edges of the plate.

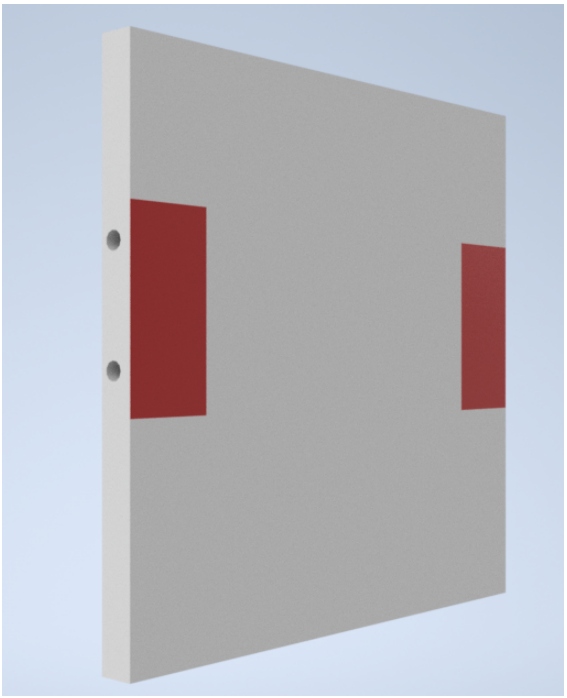

Figure 4.6: New localised heat strikes for the simulations. The new model has two constant rectangular heat strikes both centred on the cooling pipes and with a width of 5cm and a height of 9.5cm.

an agreement in the general profile for each TC pointing to a general agreement with the physics of each and that at this point the inputs of the simulation require tweaking to achieve accurate modelling of the temperature response (currently the simulation reaches a max temperature of $\approx 560^oC$ which is over 100^oC

hotter than the measured experimental profile.)

(a)

Ion Side

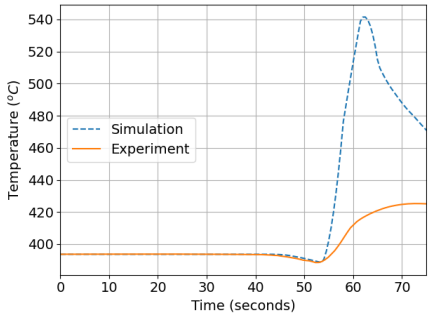

(b)

Center

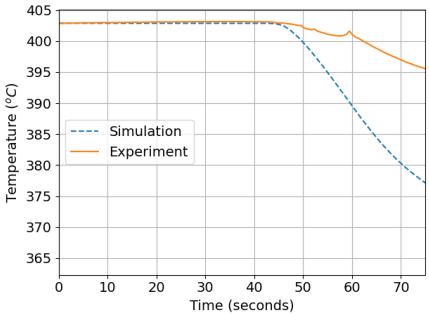

(c)

Electron Side

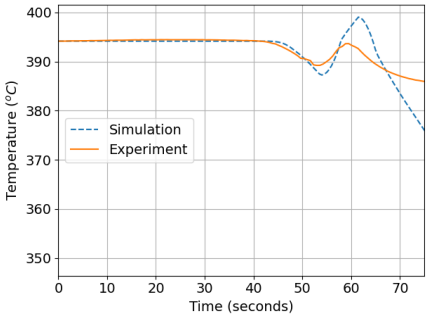

Figure 4.7: Comparison of the central profile TC traces showing the traces for the ion side 4.7a, centre 4.7b and the electron side 4.7c. The two profile sets show a general agreement in there shape, though the inputs to the simulation must now be tuned to accurately match the two.

4.2 Profile Matching

4.2.1 Time Domain Splitting

The simulation now produced profiles that agree with the general shape displayed by the experimental traces pointing to a good grasp of the physics within the simulation. For accurate calculation of the power absorbed a full 1D match, i.e matching of ΔT during the plasma exposure, was attempted between the simulation and experiment. Due to the vast number of parameters involved in determining heat transfer and the turbulent flow of the cooling gas within the model the simulation was split into two discrete time domains within which one was dominated by flow parameters and another dominated by heating allowing for a smaller set of parameters to be studied at one time reducing the computational load. Once the parameters for each domain were selected a parametric sweep was run in COMSOL varying the inputs around regions of interest, producing a spread of temperature profiles which are then compared to the experimental data.

The first region encompasses the firsts 55s, the period just before plasma contact, during this period only cooling effects the heat transfer on the plate and therefore a study of only the cooling gas flow parameters is required to match this region. In this domain the three parameters varied were the pressure change across the inlet and outlet of the cooling pipes (a larger pressure difference results in faster gas flow resulting in increased heat removal from the plate), the cooling rate of the Helium at the inlet (pipes will start off hot and their temperature will drop during the shot as they are cooled by the gas, this was modelled by decreasing the Helium temperature at the inlet during the shot) a faster ramp down of the inlet temperature will produce a higher cooling rate and the last parameter was the gas temperature at the inlet after (the lower the final temperature the faster the cooling.) The first set of sweeps was run with a pressure difference ranging from $\Delta P = .5x10^3 Pa - 4.5x10^3 Pa$, a temperature drop varying from $-5Ks^{-1} - -25Ks^{-1}$ and a final temperature in the range of $293.15K - 493.15K$. Both the temperature drop and final temperature of the gas was estimated by looking at the temperature trace from the TC attached to the outlet of the cooling lines. The profiles produced by the parametric studied were then imported into python within which they were compared to the experimental profiles using three different statistical methods: L_1, L_2, L_∞ defined below:

$$L_1 = \Sigma|x_{exp} - x_{sim}| \tag{4.1}$$

$$L_2 = \sqrt{\Sigma|x_{exp} - x_{sim}|^2} \tag{4.2}$$

$$L_\infty = max(|x_{exp} - x_{sim}|) \tag{4.3}$$

Where x_{exp} and x_{sim} are the values of the temperature at a given node for the experiment and simulation respectively. L_1 will return the profile with the lowest average difference between nodes, L_2 returns the profile with the lowest root mean squared difference between nodes and L_∞ returns the profile with the smallest maximum difference between respective nodes. The best matched profile from each of the statistical methods was then plotted alongside the experimental traces this is shown in figure 4.8.

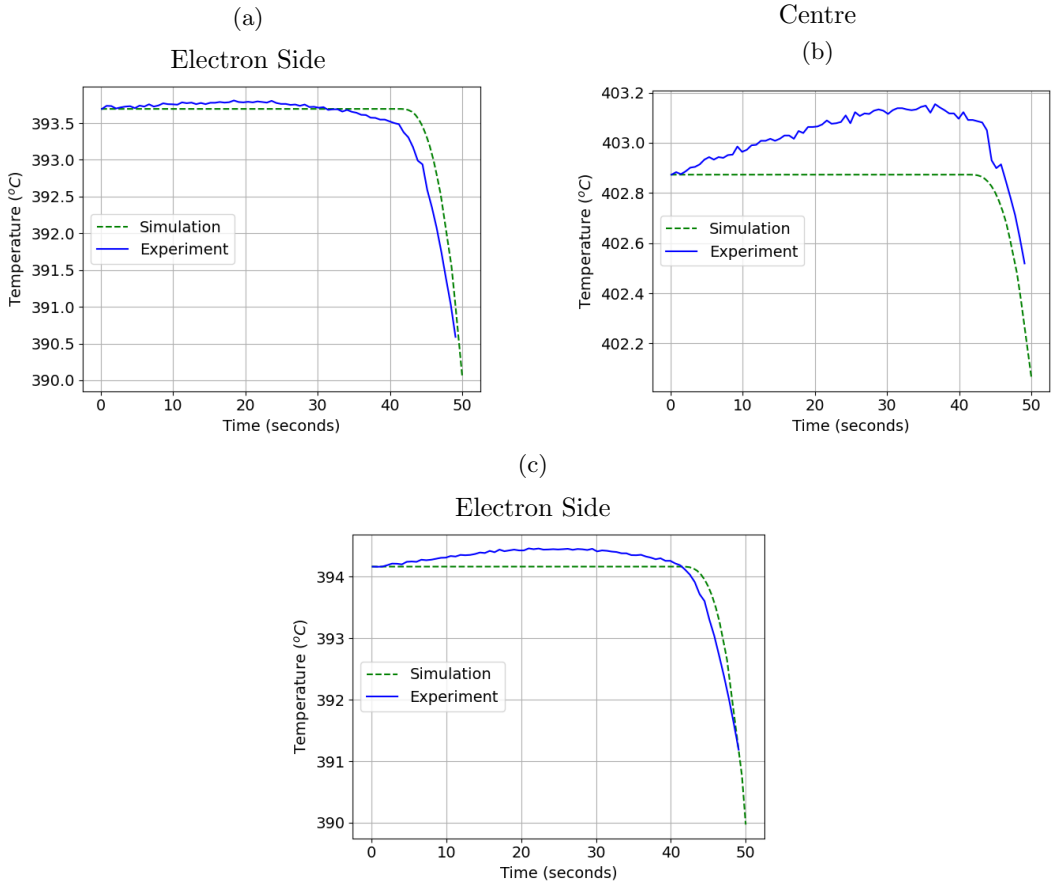

Figure 4.8: Best fit with the three statistical methods between the simulation and experimental profiles for the three TCs centred on the cooling lines. Discrepancies before the line to the cooling gas is opened (before 40s) between the two data sets arise due to heat conduction in the experiment as the plate temperature is not uniform, further difference can be attributed to the heaters which can't be accurately represented in the simulation as no data of the power they were run at was takena. Parameters for the match were a pressure drop of $2.25x10^4 Pa$ across the gas line, a temperature drop of $15Ks^{-1}$ and a final gas temperature of $293.15K$.

TC5 and TC8 show a very close match between simulation and experiment for inputs of $2.25x10^4 Pa$ for the pressure drop along the cooling pipes, a temperature drop of $15Ks^{-1}$ and a final gas temperature of $293.15K$. TC6 shows a greater deviation between simulation and experimental data. This arises due

to the assumption that the temperature across the plate is constant initially for the simulation. In fact, there is a non-uniform profile in the experiment, the initial temperature profile for shot 95058 is shown in figure 4.9, there is a variation of $\approx 50^oC$ across the plate. From the figure it can be seen there is a region of higher temperature below TC6, therefore, prior to cooling heat is conducted to TC6 explaining the rise in the temperature reading in the first 40s and the discrepancy between the simulation and experimental profiles. Concurrently to this effect is the presence of the heaters in the back of the plate which can not be accurately simulated as no data of the power they were run at as a function of shot time was taken. After these consideration it was accepted that a strong match had been achieved for the cooling domain.

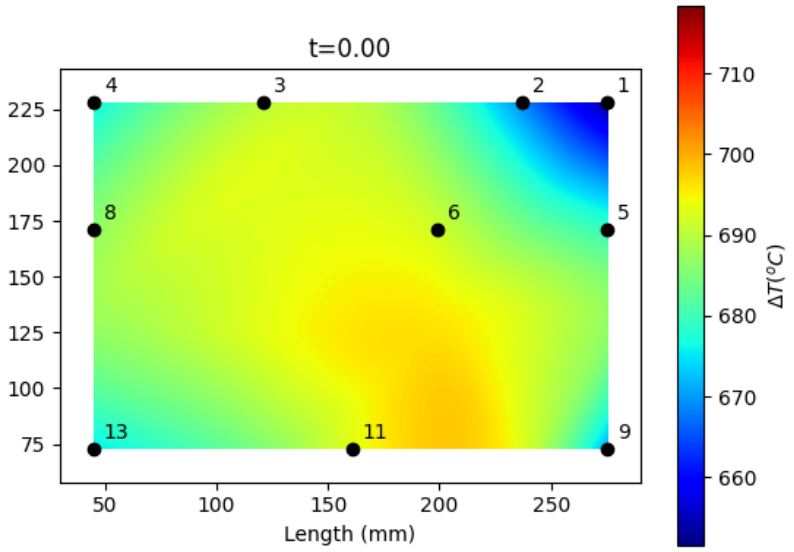

Figure 4.9: Surface temperature plot showing the initial temperature profile for shot 95058. A temperature spread of around 50^oC is seen on the plate differing from the simulation where the plate is modelled as being of constant temperature initially.

The next time domain lasted from 55 to 65 seconds and encompassed the interaction between the plate and the plasma. In this region a nice simplification due to the localised heat strikes on each side of the plate being independent of each other with the electron side heating due to electrons and the ion-side heated by the ions. This simplification allows for the heating sweeps for each side of the plate can be decoupled and studied independently allowing for the number of parameters in one sweep to be further reduced. The same profile matching process discussed above was followed with one study running an ion heat flux sweep of $1MWm^{-2} - 6MWm^{-2}$ and the other with electron heat flux ranging from $.05MWm^{-2} - .2MWm^{-2}$. Plots showing the experimental traces compared to the best matched profiles can be found in figure 4.10.

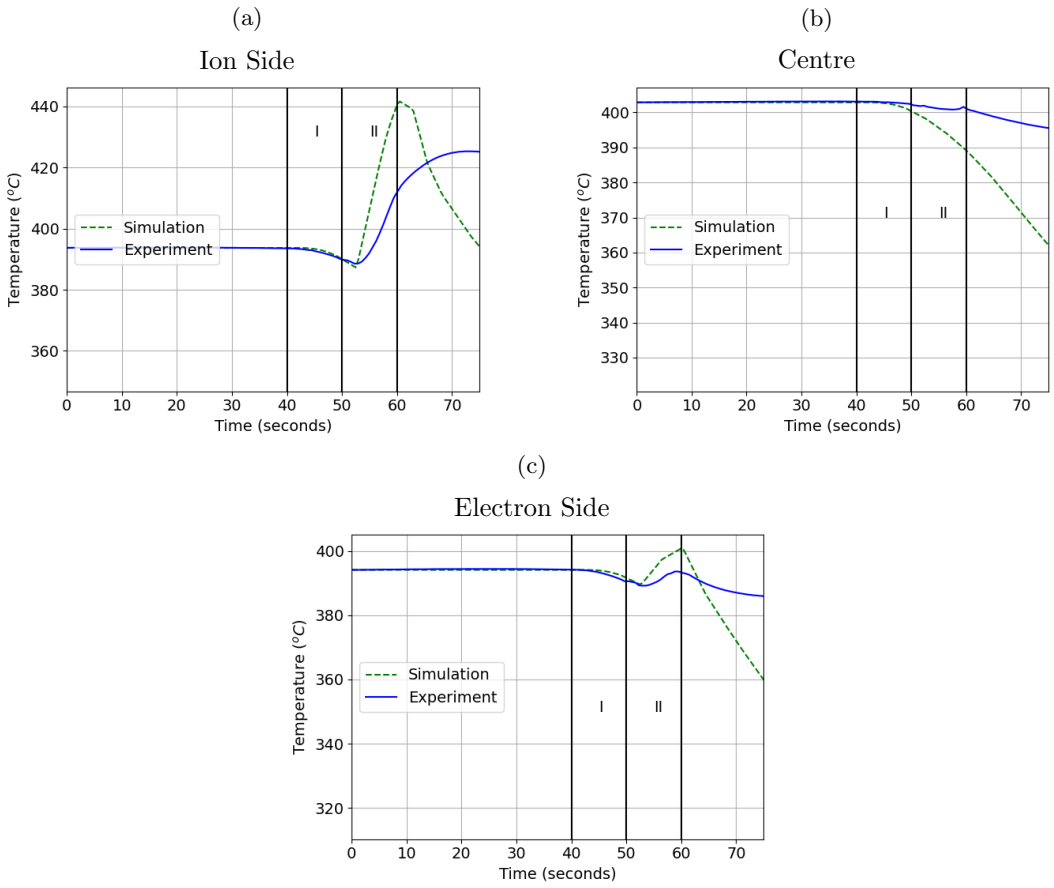

Figure 4.10: Figure showing the comparison between the experimental (blue line) and the best matched simulation traces according to the statistical method. Region I (40-50s) is the cooling zone in which the helium cooling is started, plasma contact occurs in region II (50-60s). The plots show a vastly increased cooling rate in the simulation traces producing a rapid temperature drop-off after the plasma exposure.

Unfortunately two major issues are highlighted from these plots. Firstly the trace for the central and electron side TCs show a rate of cooling that is far higher in the simulation post-plasma exposure. This is caused by the assumption that though the flow parameters will affect the heat transfer during the heating regime they should have already been matched by the previous study in the cooling domain. As the cooling gas only flows for 10s before plasma contact, the temperature drop in this region is governed by the reduction in the inlet temperature as the final temperature of the gas is not reached until the plasma strike. This lead to a much lower cooling gas temperature in the simulation producing the excessive cooling post-shot. The other issue is that TC5 displays a much narrower peak in the simulation the reasons behind this are two-fold: increased cooling present in the simulation and alongside this the presence of a heat stripe on the side of the plate on the ion-side. A study of camera images of the plate during camera exposure (shown in figure 4.11) shows that there is a heat strike on the side of the ion-side heat flux of the plate. The distance

between the side of the plate and the ion side TC is greater than that between the front plate and the same TC, therefore this ion-side heat strike introduces a thermal lag broadening the peak in the profile on the ion side. This effect is further collaborated by the melting of a TZM enclosed Langmuir probe that was positioned on the edge of the ion-side.

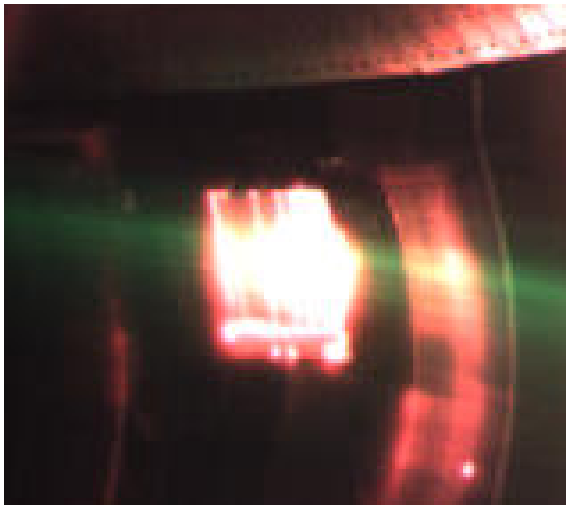

Figure 4.11: CCD showing heat strike incident on the plate, as viewed from the ion-side. The photo shows a large interaction between the plate and the plasma on the side of the plate on the ion side.

4.2.2 Ion Side Heating and Width Scan

Two extensions to the model are proposed to broaden the TC5 peak shown in figure 4.10a. Inclusion of a heat flux on the ion side of the plate will broaden the peak due to the longer travel time for temperature from the side of the plate to TC5. The second proposition is to edit the shape of the heat stripe, the idea behind this is that if the heat flux no longer in a region directly above the TC, similarly to the side heating a thermal lag will be induced into the model broadening the peak. sss Figures showing a TC trace comparison between a 5cm wide and a 3cm wide heat strike on the ion side of the plate can be found in figure 4.12 (note as the heat flux is the same in both case, the 5cm will have a greater power deposited on the plate in comparison to 3cm.) As predicted the narrower heat strike produces a broader peak in the trace, however the narrower heat strike also displays a faster thermal response to the plasma exposure which is counter-intuitive and disagrees with the ideas mentioned above of a thermal. This error in the code is reasoned to have arisen from the re-meshing of the problem when changing the shape of the heat stripe leading to an instability in the model.

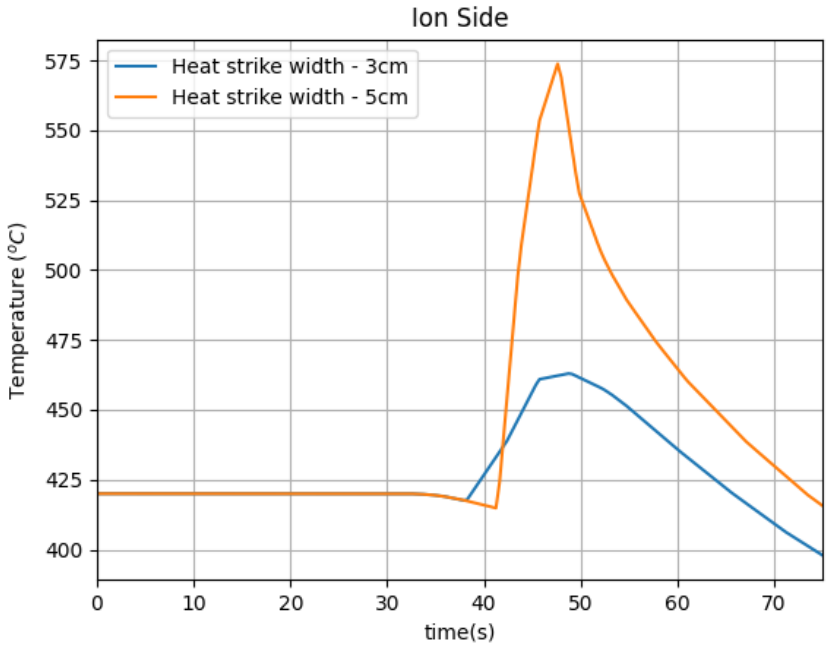

Figure 4.12: Comparison of simulations ran with a heat strike width of 3cm with that of 5cm on the ion side. Profile shows the computed temperature change on the ion side of the plate. Interestingly the narrower heat strike shows a faster temperature response this is reasoned to be unphysical and a result of the boundary heating condition being defined geometrically in the model.

Due to the inconclusiveness and error raised with the ion-width study a new model was created to study the effect of side heating on the measured profile on the ion side. To model this new heat stripe, a new boundary heat condition was included with the same distance vertically along the plate as the front strike and covering the entire width of the side in this region. Over this new region it was assumed that the heat flux here is identical to the front surface. Plots produced for TC5 with and without side heating are shown in figure 4.13

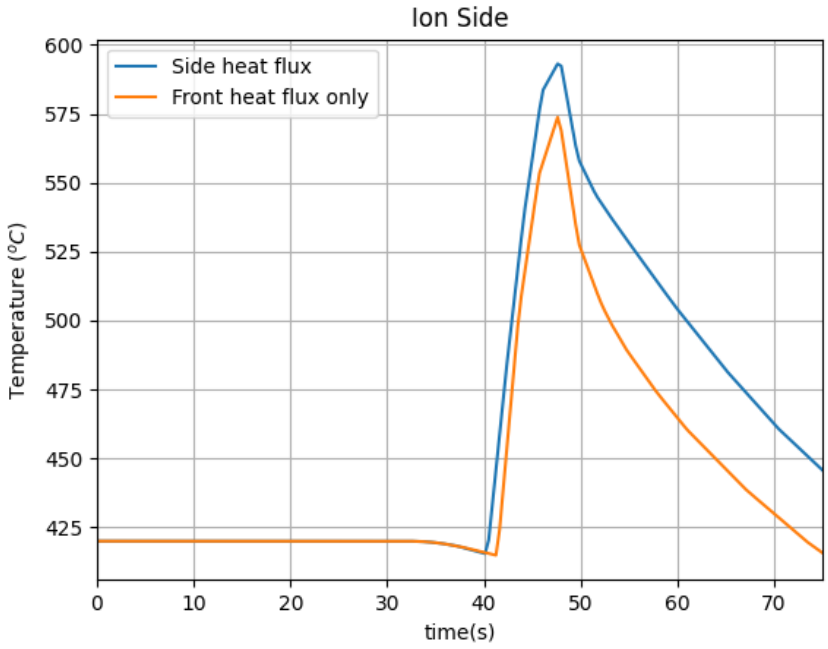

Figure 4.13: Comparison of simulations ran with and without side heating. The inclusion of side heating within the model does act to broaden the peak in the temperature profile on the ion side however again meshing issues produce a greater cooling rate with the new geometry.

The model ran with a heat stripe included on the side of the plate produces a higher peak value of temperature, as a new boundary heat flux has been added the thermal power to the plate has been increased. A broader peak is also seen from the side heating at a temperature of around $860K$ (the peak of the non-side heated trace) the gradient of the trace changes, this gradient change is reckoned to arise from heat conducting from the side of the plate clearly showing that side heating will broaden the temperature profile. However another issue arises due to the re-meshing of the model that occurs with the inclusion of a new heat boundary flux, with this model showing a greater cooling rate and an earlier temperature rise. This instability between two differently meshed systems highlights the need for an analytically (rather than geometrically) determined heat strike and this will be touched on in the next section.

4.2.3 Analysis with Gaussian Heat Fluxes

Ultimately it was chosen to model the two heat strikes by defining a two dimensional gaussian profile in x and y (i.e vertically and horizontally upon the plate) on each side of the plate, the heat strike produced by each profile is shown in figure 4.14. The profiles on either side of the plate were identical, centred above the cooling lines. and with a standard deviation of $\sigma_x = .05m$ and $\sigma_y = 0.03m$.

The profiles were both normalised to the value of the peak heat strike on each side. Remodelling the

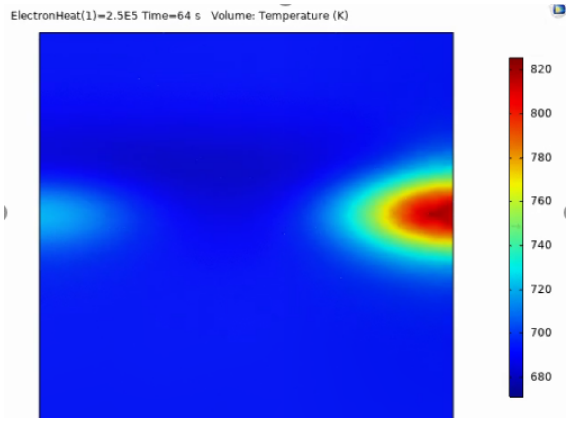

Figure 4.14: Surface temperature plot from simulation highlighting new gaussian profiles. Profiles were centred on the cooling lines as before and were set by a peak value on both the electron and ion side with a standard deviation of $\sigma_x = .05m$ and $\sigma_y = 0.03m$

heat strike as an analytic function rather than a geometric shape allows for the shape and size of the heat strike to be changed without remeshing the problem (changing the geometry) improving the stability of the simulation. The central line TC traces with the new heat strikes compared to the experimental data can be found in figure 4.15 The parameters input to the simulation were: an Ion heat flux of $1.025MWm^2$, an electron heat flux of $.25MW^2$ an absolute gas temperature if $500K$, a temperature drop of $15Ks^{-1}$ and a pressure drop of $22.5x10^3Pa$ along the pipes.

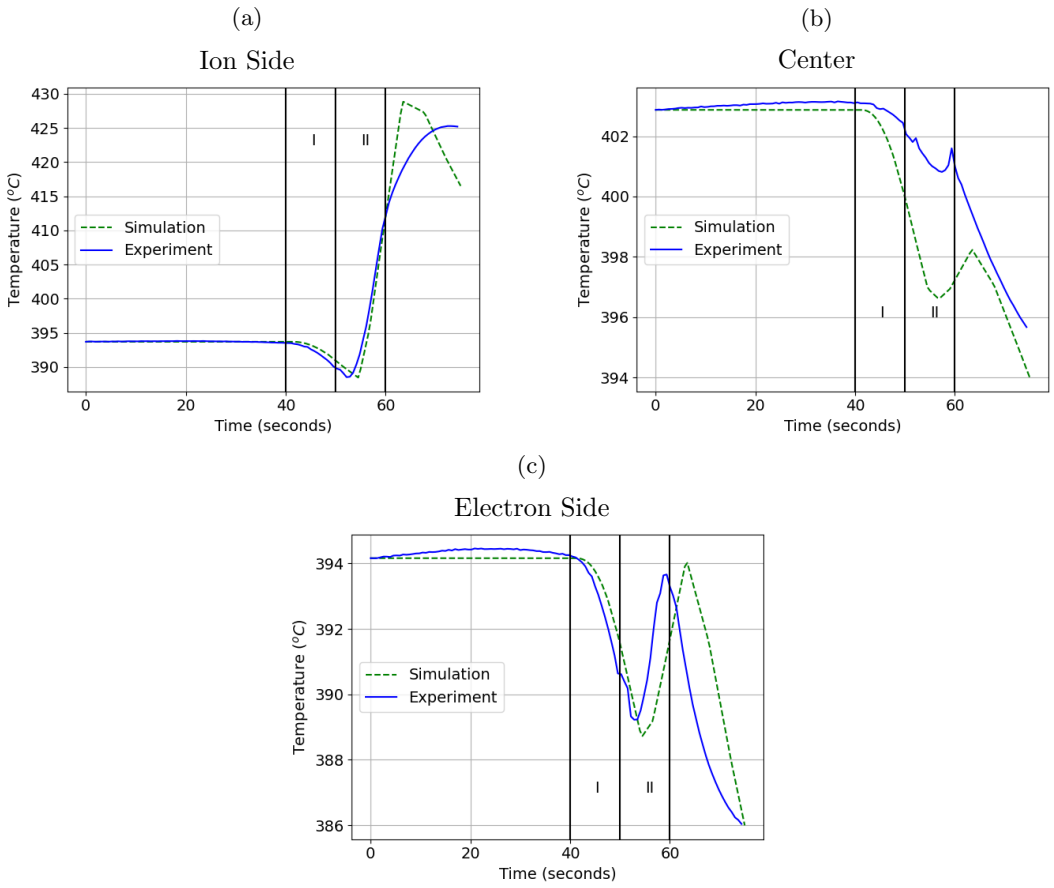

Figure 4.15: Best fit between the simulation and experimental profiles for the three TCs centred on the cooling lines, with the simulated heat stripe solely on the front of the LiMIT plate with two seperate gaussian heat profiles on the ion and electron sides of the plate. Figures show ion side 4.15a, centre 4.15b and electron side 4.15c comparisons. Note that conduction on the plate prior to plasma exposure results in a minor deviation between the simulated and experimental profiles for the central profile.

TC8 shows a very strong match with the simulation data shifted slightly later in the shot this arises from a non-perfect start time in the experiment, human variations that can not be accounted for in the simulation. TC5 also agrees well with the 0-D temperature rise however the simulation shows a more rapid decline in temperature post-shot a remedy to this error will be revealed later. TC6 indicates the biggest deviation between simulation and experimental data. The reason behind this was touched on before the non-even heat profile in the simulation leads to heat being conducted to TC6 before the cooling is switched on leading to a heat rise that is not accounted for in the simulations this coupled with the fact that the final temperatures and general shape correlate points to a mating in TC6.

After (hopefully) convincing the reader that TC6 is well matched the only issue that remains is the fast drop-off in the temperature profile for TC5. Previously it was shown that the inclusion of a heat strike on the side of the ion-side of the plate lead to a flatter temperature profile at the apex as heat takes longer to

conduct from the side of the plate to the TC however a side effect of this is a larger temperature rise due to the increased power deposited on the plate. A new heating match sweep on the ion side was performed with a new gaussian profile defined on the side of the plate, it was assumed that the heat strike would be normalised to the same peak value as the front face, be constant across the thickness of the plate and would vary across the plate identically to the heat strike on the front surface. The best matched profiles for this new scan alongside the non-side heated profiles can be found in figure 4.16, this new simulation was run for an ion-side heat strike of $0.95 MW m^{-2}$ (side and front) and all other parameters identical

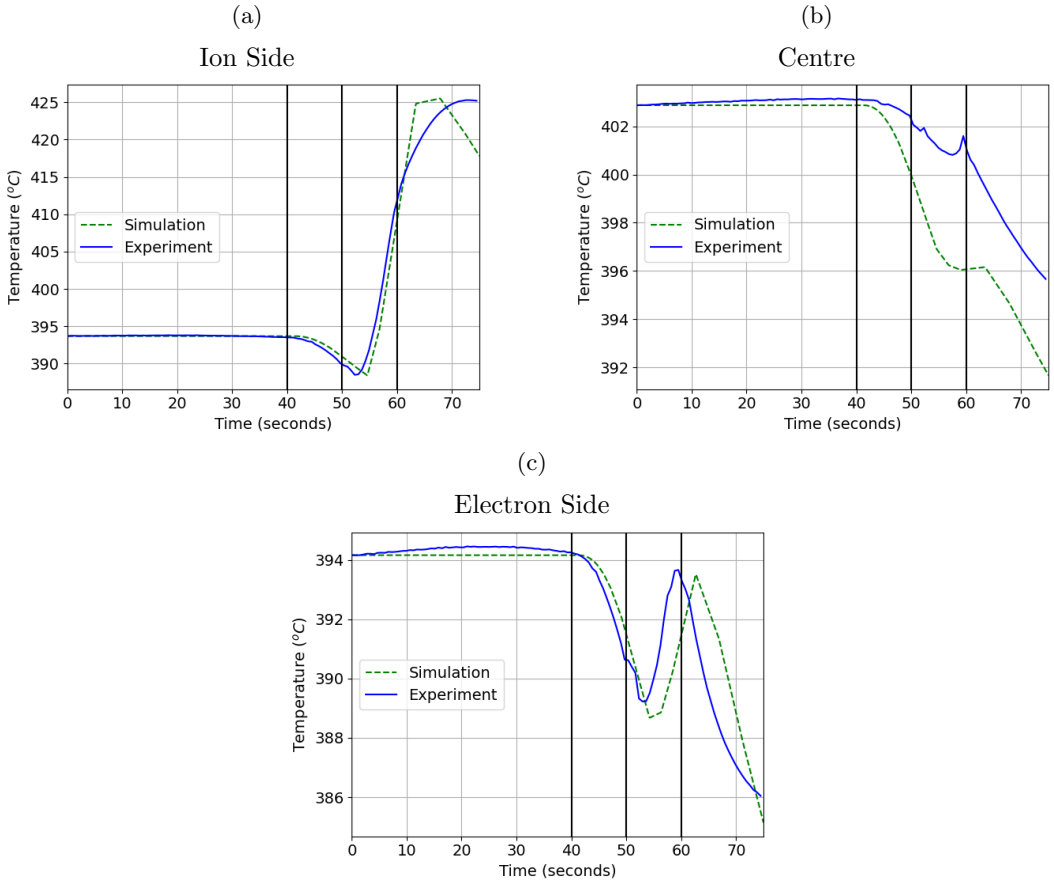

Figure 4.16: Best fit between the simulation and experimental profiles for the three TCs centred on the cooling lines, with the simulated heat stripe on the front and ion side of the LiMIT plate. Figures show ion side 4.16a, centre 4.16b and electron side 4.16c comparisons. Note that conduction on the plate prior to plasma exposure results in a minor deviation between the simulated and experimental profiles for the central profile however a flatter peak in the profile of TC5 now more accurately matches the experiment.

As expected the simulations with a side heat strike included show a flatter profile for TC5 and very minimal difference for TC6 and TC8 (this is to be expected with only the ion heat strike been changed from the prior tests.) At this point of the study a strong agreement has been achieved between the simulations and the experimentally profiles enabling the utilisation of the simulation data to provide deep analysis into

the plate performance during EAST testing.

Chapter 5

Interpretive Analysis

To extend the breadth of the research the process described above was applied to a multitude of shots from the EAST campaign as an attempt to discern the effect on the thermal load of changing the auxiliary heating power, the radial position of the limiter and the helium cooling pressure. The next section will highlight the results achieved from this extension and finishes with a discussion of what can be learnt from it to improve the future testing of lithium PFCs.

5.1 Pressure Scan

The first parameter studied was the effect of the pressure of the helium cooling gas on plate and plasma performance. The parameters for the shots chosen for analysis can be found in table 5.1, the shots were run with identical auxiliary heating, plasma current and fuelling. Figure 5.1 shows the heat fluxes incident on the ion side (q_i) and the electron side (q_e) of the plate as well as the max temperature change measured by the thermocouples. The figure shows that the cooling pressure has no impact on the heat flux incident on either side of the plate, this point is further highlighted through the measurement of the global key plasma parameters (W_{mhd}, n_e, τ_e) which show very little change between shots. However the temperature change on the ion side of the plate, i.e the maximum temperature change on the plate, drops as cooling pressure is increased, with no cooling active on the plate $\Delta T \approx 40^oC$ compared to a $\Delta T \approx 15^oC$ with 3MPa highlighting a marked improvement in heat handling capability.

Table 5.1: Key Parameters for the shots investigating the effect of helium cooling pressure on plate performance

Shot #	Distance from separatrix (cm)	Average Limiter Temperature (^{o}C)	Auxiliary Heating Power (MW)	Helium Cooling Pressure (MPa)	Line averaged n_e ($10^{19}m^{-3}$)	Plasma Energy, W_{mhd} (kJ)
95057	3	400	3.4	0	4.19	140
95058	3	400	3.4	1	4.175	139
95059	3	380	3.4	3	3.934	139

These results are to be expected, increasing cooling pressure would only effect plasma parameters via a reduction in the vapor shielding of the plate (increased pressure leads to increased cooling rate thereby reducing the surface temperature of the lithium and as such the evaporation rate from the plate) however for all of these shots the plate temperature was well below the lower limit for vapor shielding (the limit being well in excess of 600^oC [90]). The operational limit ultimately leads to the key point of this result; application of helium cooling allows for lithium PFCs to withstand higher intensity heat fluxes for an extended time periods without overstepping their operational limit enabling continuous operation in the low recycling regime.

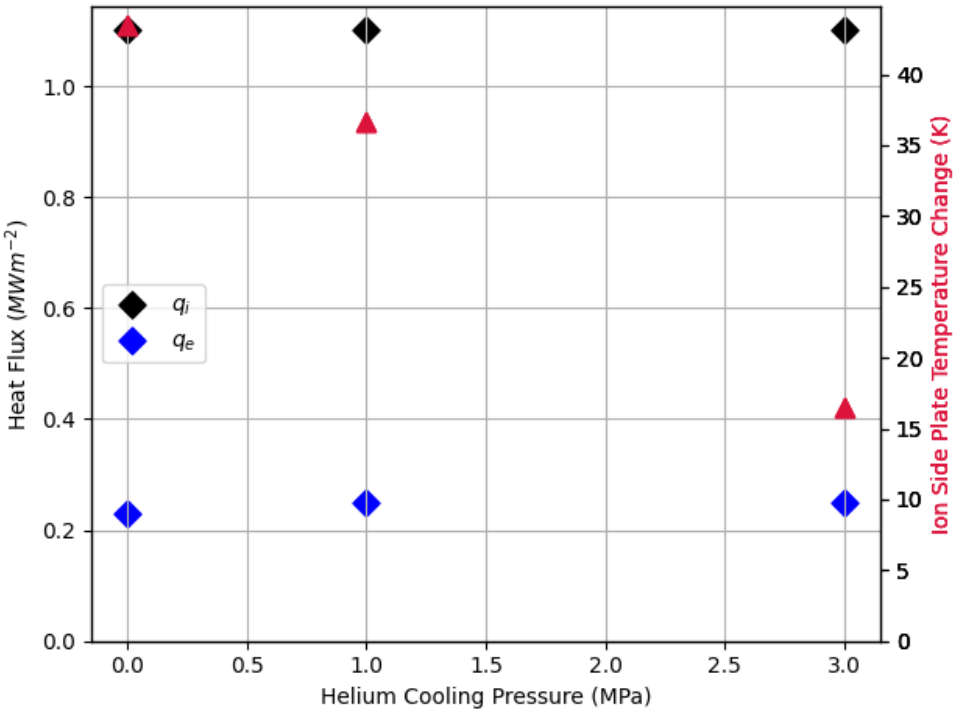

Figure 5.1: Heat fluxes and temperature change for the helium cooled shots. Increasing helium gas pressure has minimal effect on the heat flux on the plate, i.e no change in plasma conditions, but does enable the plate to handle an equivalent heat flux with a far reduced thermal response.

5.2 Power Scan

An RF power heating scan, with powers ranging from 2.9MW to 3.9MW as a combination of ECRH and LHW heating supplying the power, forms the basis of this section of analysis. The shot parameters for the RF scan shots can be found in table 5.2, note that shots with helium cooling have been included in this study due to the lack of effect the plasma parameters as shown in the section above.

Figure 5.2 shows the ion and electron side heat fluxes as a function of auxiliary heating power. The

Table 5.2: Key Parameters from the RF power scan shots

Shot #	Distance from separatrix (cm)	Average Limiter Temperature (^{o}C)	Auxiliary Heating Power (MW)	Helium Cooling Pressure (MPa)	Line averaged n_e ($10^{19}m^{-3}$)	Plasma Energy, W_{mhd} (kJ)
95055	3	380	2.9	0	4.1	116
95056	3	390	3.4	0	3.916	136
95057	3	380	3.4	0	4.194	140
95058	3	400	3.4	1	4.175	139
95059	3	380	3.4	3	3.934	139
95060	3	360	3.9	0	4.054	152
95061	3	330	3.9	0	5.11	154

plot shows a general increase in heat flux with RF heating power clearly an increase in stored energy of the plasma and a decrease in confinement time, shown in figure 5.3, will result in a higher incident heat flux on the plate. Transport locally at the plate also increases with increasing auxiliary power leading to a higher particle flux at the plate and thus a more intense heat flux, this is emphasised by the local gyro-Bohm diffusion at the plate (figure 5.3(f)) which is highest for shots 95060 and 95061.

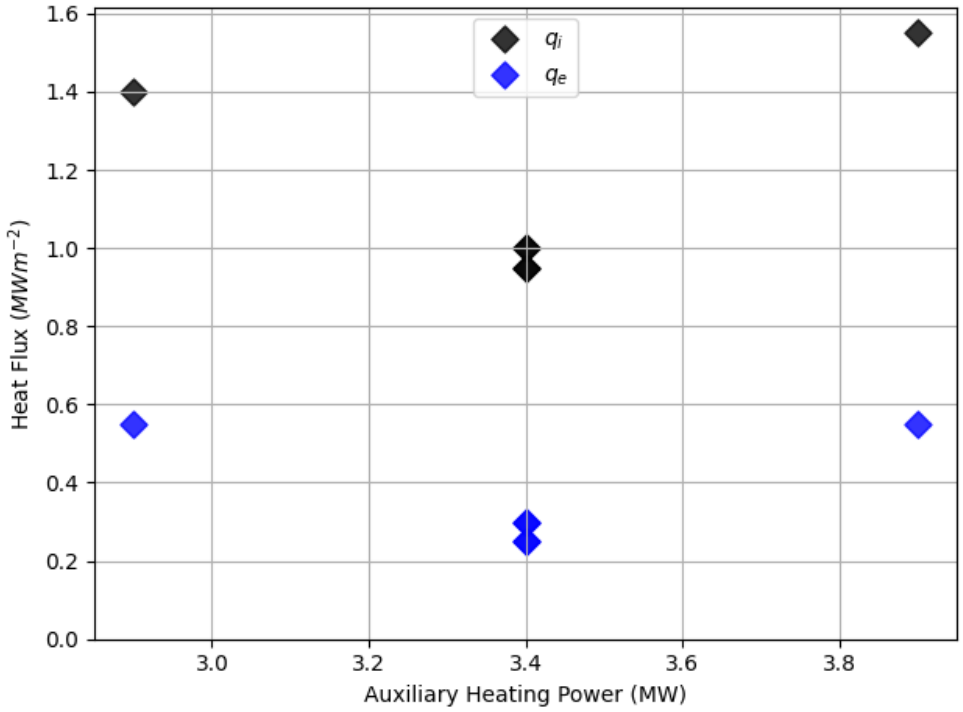

Figure 5.2: COMSOL computed heat fluxes for the Power Scan. Between 3.4MW and 3.9MW an increase in auxiliary heating power increases the heat flux experienced by the plate however an anomalous result is present at 2.9MW with it displaying a higher flux than 3.4MW

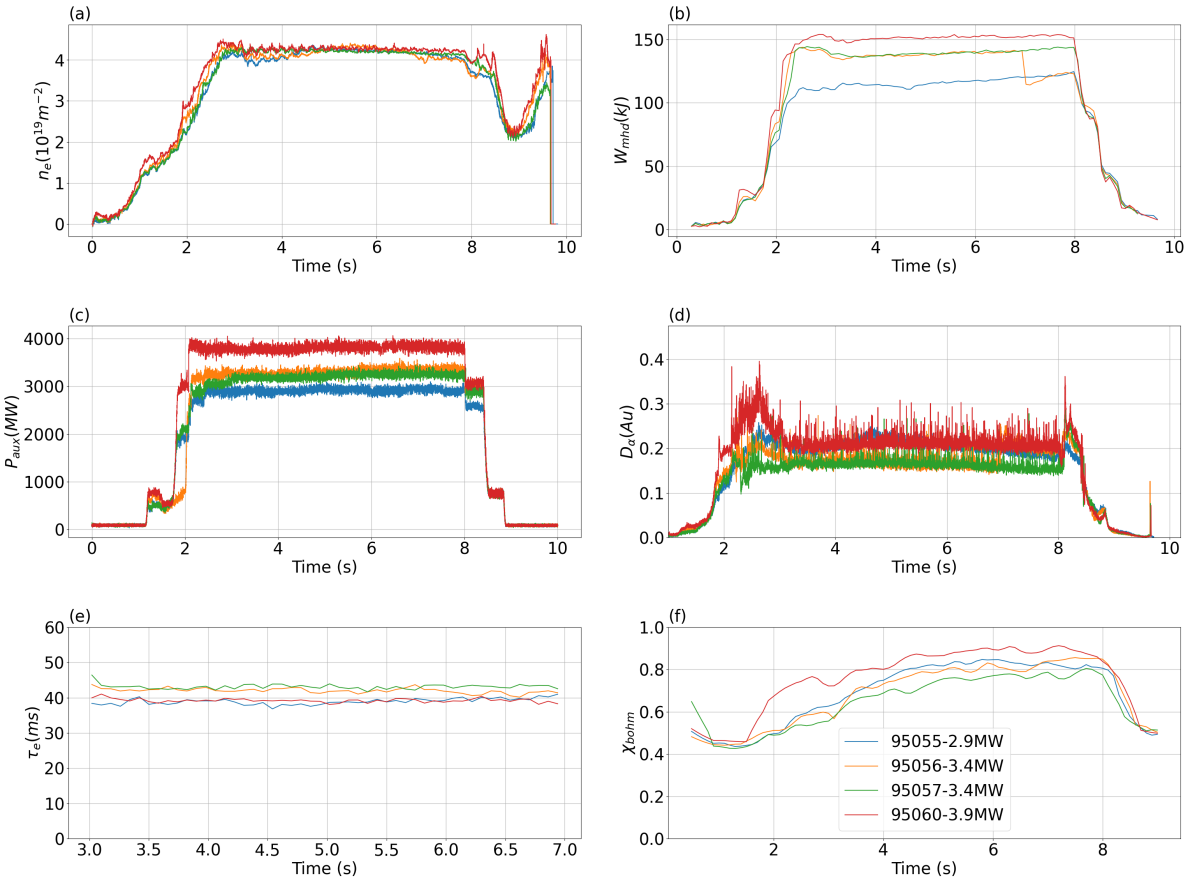

Figure 5.3: Time traces for the three powers included in the RF power sweep (2.9MW,3.4MW and 3.9MW.) Plots show line averaged density (a), stored plasma energy (b), total auxiliary heating power (c), D_{alpha} (d), global confinement time (e) and the coefficient for Bohm diffusion at the plate (f.)

Shot 95055 appears an anomalous result it has the lowest auxiliary heating power ($2.9MW$) but has a more extreme heat flux than all four of the shots at $3.4MW$ which is counterintuitive, this caused by the plasma in 95055 operating in L-mode leading to a higher flux of particles and energy to the plate causing the increased temperature gain. L-mode operation is suggested by shot 95055 displaying a lower confinement time and a larger Bohm diffusion coefficient than expected, this in unison with further examination of the plasma parameters for shot 95055 decides this matter; it can be seen from the plots within figure **??** that the electron temperature and density are much higher at the plate for 95055, compared to the $3.4MW$ shots.

Though an anomalous result this shot allows for a discussion on what causes the transition from the low to high confinement. A plot of the normalised D-α for shots 95055,95056 and 95057 are shown in figure 5.4 these traces can be utilised to infer whether the plasma obtained a H-mode during the shot. Oscillations within a D_α trace indicate that ELMs are present within the plasma and as such that H mode has been achieved.

A study of the figure reveals as expected shot 95055 is completely L mode displaying zero oscillations, shot 95056 starts in H mode but then suffers a H-L transition around 7 seconds into the shot that results in a large confinement drop and finally shot 95058 produced a H mode plasma for the entirety of the shot flat top (2-8 seconds) with no major disruptions. So what causes this improvement? Well the L mode plasma in shot 95055 was likely caused by a fault in the lower hybrid wave heater that lead to a drop in power of 0.5MW this would prevent the plasma reaching a temperature required during flat-top operation to reach H mode operation. The change between shots 95056 and 95057 however, is not the result of any disruption and the difference can be elucidated via analysis of the lithium lines for both shots, figure 5.5. Focussing primarily on the Li-II line in the upper divertor it can be seen that there is a large influx of lithium during shot 95056. Therefore, it is proposed that lithium conditioning of EAST during shot 95056 allows for a full duration H mode shot to be achieved for 95057 via impurity cleansing within the plasma reducing the global hydrogenic recycling, seen by the decrease in the baseline of the D_α trace between shots 95056 and 95057, and the contaminant level within the plasma. It is important to mention that after these shots full duration H mode was achieved for every shot in the RF power scan until a large ELM disruption shot 95061.

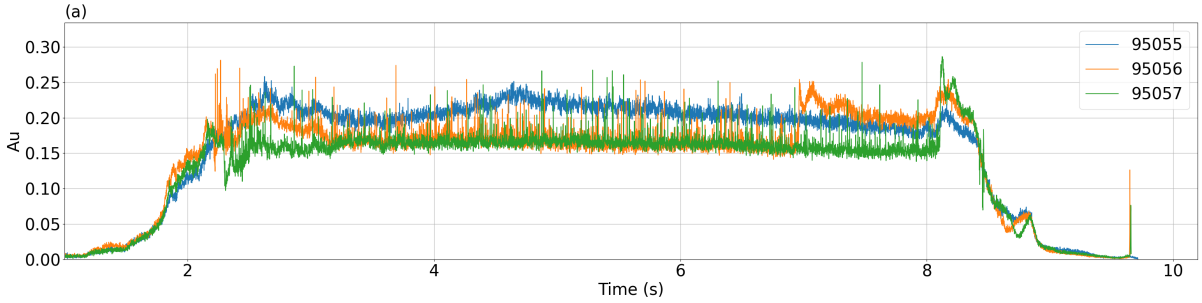

Figure 5.4: Normalised D-α traces for shots 95055 (2.9MW), 95056 (3.4MW) and 95057 (3.4MW). Oscillation in the D-α trace highlights the presence of ELMs in the plasma and as such the attainment of H-mode. Shot 95055 is in L mode for its entire duration, shot 95056 suffers a H to L transition at 7s and 95057 maintains H mode for its entire flat-top.

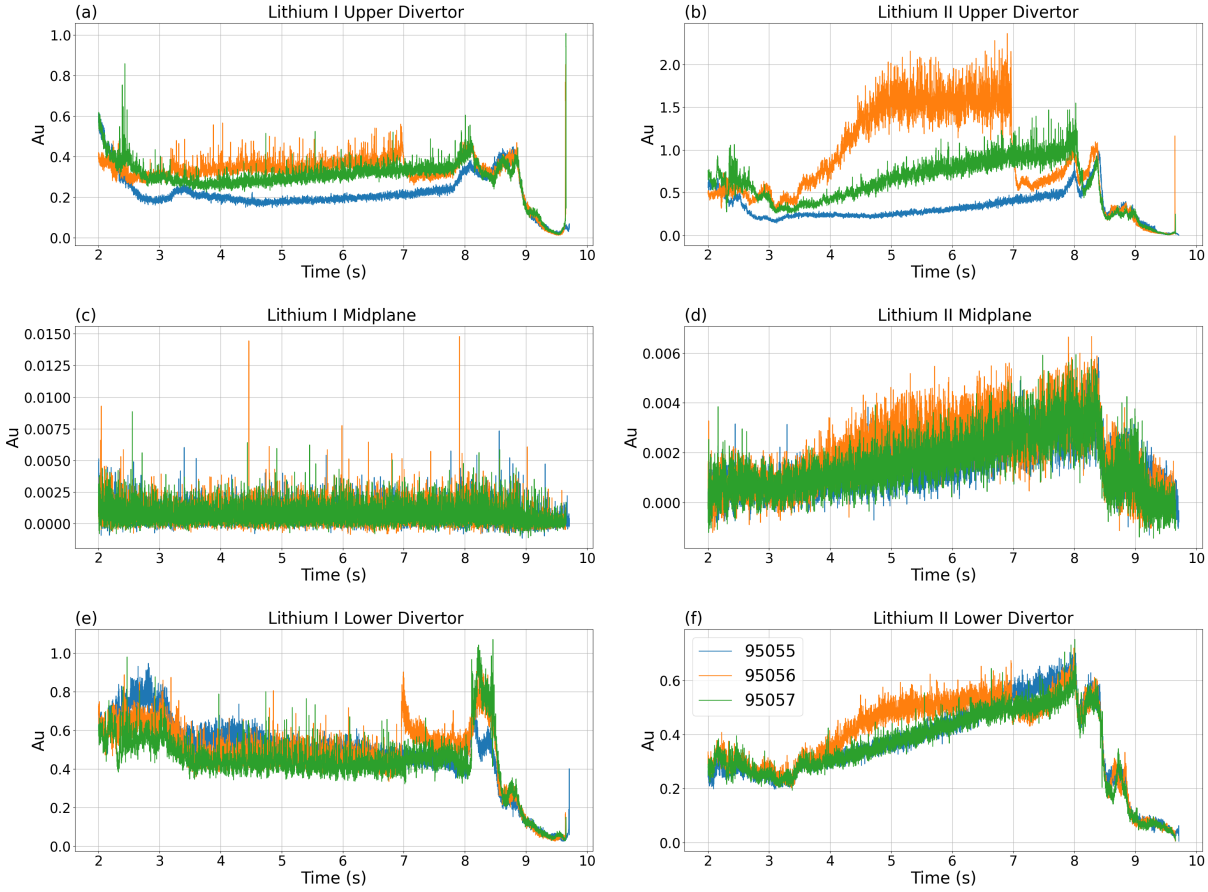

Figure 5.5: Lithium spectral lines for shots 95055 (blue), 95056 (green) and 95057 (red). Li lines shown are LiI upper divertor (a), LiII upper divertor (b), LiI midplane (c), LiII midplane (d), LiI lower divertor (e) and LiII lower divertor (f)

Shot 95061 displays interesting behaviour around four seconds into the shot there is a drastic drop in confinement time, looking at the global plasma parameters for this shot fig 5.6 a concurrent rise is seen in the line average electron density and a drop in the stored plasma energy. This points to a high to low confinement transition within the plasma correlating to a large ELMs event occurring at around 5 seconds, highlighted by a large peak in the D-α trace at this point, this was likely triggered by a high influx of tungsten to the plasma core radiating away a large amount of the plasma energy, shown by the two peaks in figure 5.7 at around four and then five seconds. This disturbance likely was caused by the lack of lithium recirculation in 95061, as the EM pumps on the plate's reservoir were not run during this shot, leading to the TZM backplate being exposed to the plasma. Interestingly though after this disturbance the plasma settles again and actually displays a higher stored energy, increasing from 150kJ prior to the disruption to 159kJ, and electron density than pre-disturbance this could be attributed to an enhanced pedestal H-mode

being achieved post disturbance. The EP mode is characterised by a wider temperature pedestal at the plasma edge suppressing the ITG and as such reducing transport within the plasma producing an increase in confinement and therefore stored energy within the plasma. NSTX [65] showed triggering of the EP mode via lithium deposits, a similar large lithium flux is shown by shot 95061 in the upper divertor, during the large ELM event around 5 seconds.

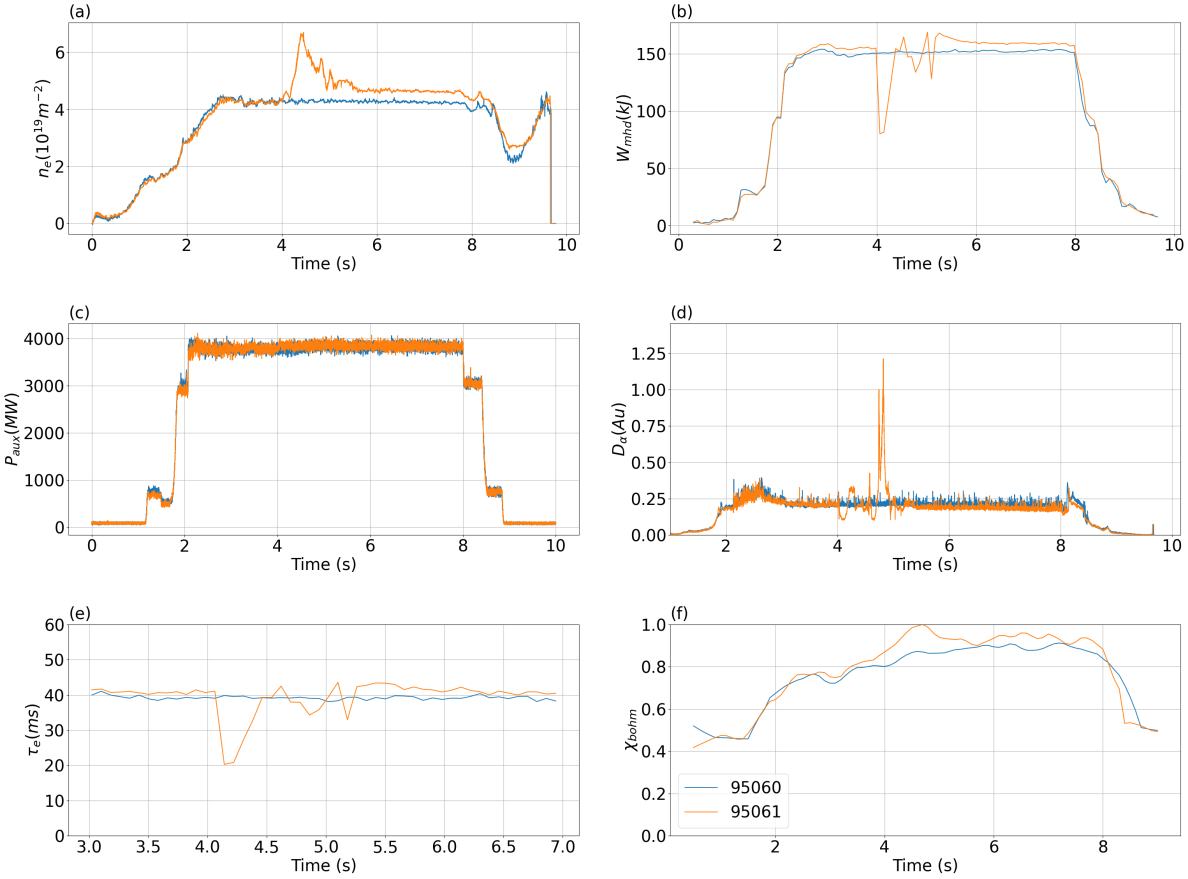

Figure 5.6: From top left top row line averaged electron density, stored MHD energy, global confinement time. From bottom left bottom row: electron density, temperature and normalised Bohm diffusion coefficient at the plate. Shot 95061 is displayed in orange and shot 95060 in blue the shots are identical except that in 95061 the EM pumps from the plate reservoir to the distributor were turned off preventing lithium replenishment.

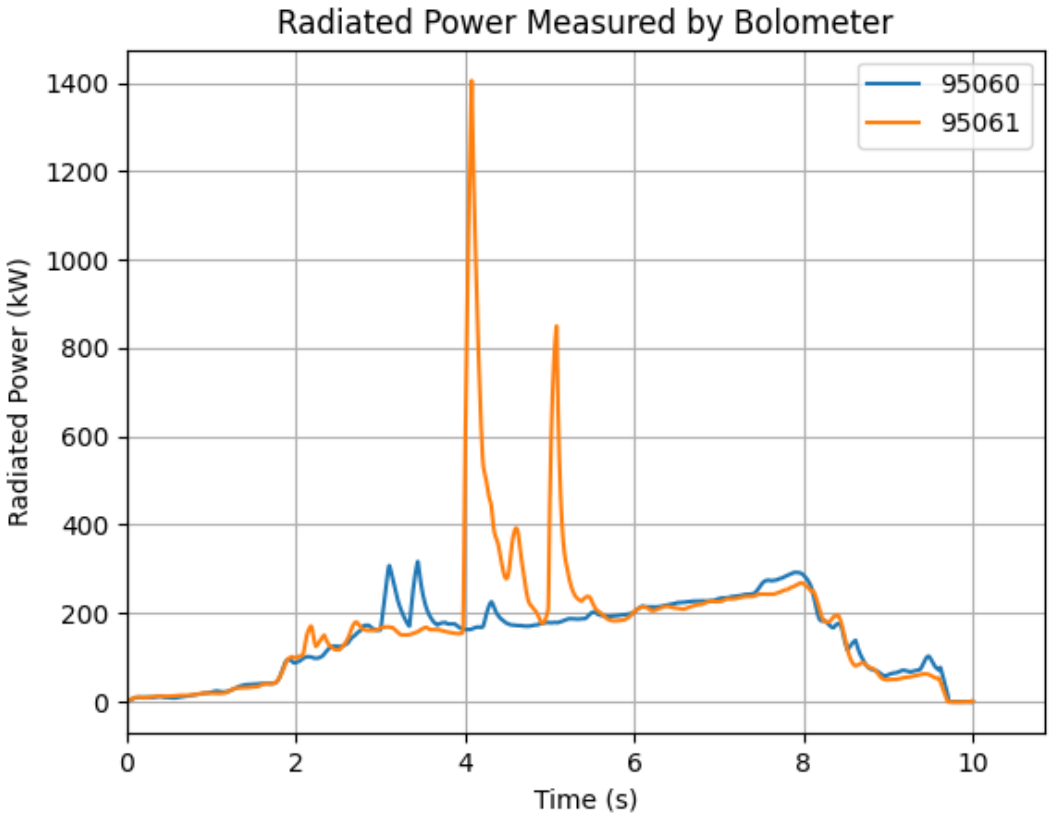

Figure 5.7: Total power radiated away by the plasma for shots 95060 and 95061 measured by the fast bolometer. Note the large spike in 95061 around 4 seconds i.e just before the radiative collapse causing an L-H transition.

5.3 Radial Scan

The next study was the effect on plate and plasma performance of changing the position of the plate relative to the separatrix, with the general expectation being of an increase in interaction between the plate and the plasma with decreasing seperation. The shot parameters for the chosen shots for this radial scan can be found in table 5.3, these shots are heated by a combination of ECRH, LHW and NBI with a total auxiliary heating power of 6.7MW . The heat fluxes as a function of distance from separatrix are shown in figure 5.8.

The distance from the separatrix has a large effect on the heat strike experienced by the plate with a roughly exponential decay in the heat flux experienced on both the electron and ion side. The ion side experiences a heat flux is $8.2 MW m^{-2}$ when LiMIT is positioned 2cm from the separatrix and only $0.1 MW m^{-2}$ at a distance of 5cm, suggesting that the decrease is not due to solely intensity drop off. This can be explained by recalling that heat-flux localisation on the ion and electron side of the plates was a

Table 5.3: Table of key parameters for the shots included within the scan of position of LiMIT relative to the separatrix

Shot #	Distance from separatrix (cm)	Average Limiter Temperature (^{o}C)	Auxiliary Heating Power (MW)	Helium Cooling Pressure (MPa)	Line averaged n_e ($10^{19}m^{-3}$)	Plasma Energy, W_{mhd} (kJ)
95115	7	350	6.7	0	4.14	164
95116	5	350	6.7	0	5.803	177
95117	3.5	350	6.7	0	3.979	177
95118	2.5	350	6.7	0	3.933	166
95121	2	370	6.7	1.5	3.934	160
95125	2	339	6.7	1.5	3.741	154

feature of the magnetic field lines being angled with respect to the flat plate hence producing a component of the parallel heat flux incident on the plate. The further the plate is located from the separatrix the more diminished this effect will be as the parallel heat flux will be constrained primarily within the LCFS. This decrease in the localisation effect on the heat strike with increasing radial position can be seen from the surface temperature change of the plate during the ten second plasma exposure for each shot, figure 5.9, where a growing 'shadow' is observed on the centre of the plate as it is move closer to the separatrix.

Analysis of the stored plasma energy and plasma confinement time, figure 5.10 for the radial scan yields some interesting data and provides/verifies a number of key aspects of lithium limiter operation. Shots 95116 and 95117, positioned at 5cm and 3.5cm from the separatrix respectively, produced a marked increase in stored energy ($\approx 11kJ$ higher) and confinement time from shots closer to the separatrix (95118,95121.) This effect is further emphasised by a drop in the auxiliary heating power in shot 95116 (measured as $\approx$ 6.0MW compared to the 6.7MW set value,) this arose due to a reduced lower hybrid wave contribution perhaps caused by worse coupling between the plasma and lower hybrid wave due to the increased plasma frequency (due to larger n_e) in the shot.

A cause for this improvement in plasma performance can be found by studying shot 95115. Analysis of the D_α spectral lines (5.11 (d)) highlights a large ELM event occurring at the end of the shot 95115, this is correlated with a large increase in the Li-II line observed in the upper divertor (5.11 (f)). Therefore, it is proposes that this ELM event lead to a mass lithium evaporation from the plate. This lithium is then re-deposited on the walls of the chamber (most importantly the divertor region) conditioning them, as seen in [58], leading to the increase in confinement time for 95116 and 95117 and thus in the stored energy in plasma. The drop in confinement time in 95117 compared to 95116 arises can then be explained as lithium being evaporated/sputtered off the walls of the chamber during the shots and worsening the conditioning. This increase in confinement can be observed locally to the plate via the suppression of the Bohm diffusion in shot 95116 and 95117. Diffusion is lower than for the shot at a larger distance from separatrix. As the

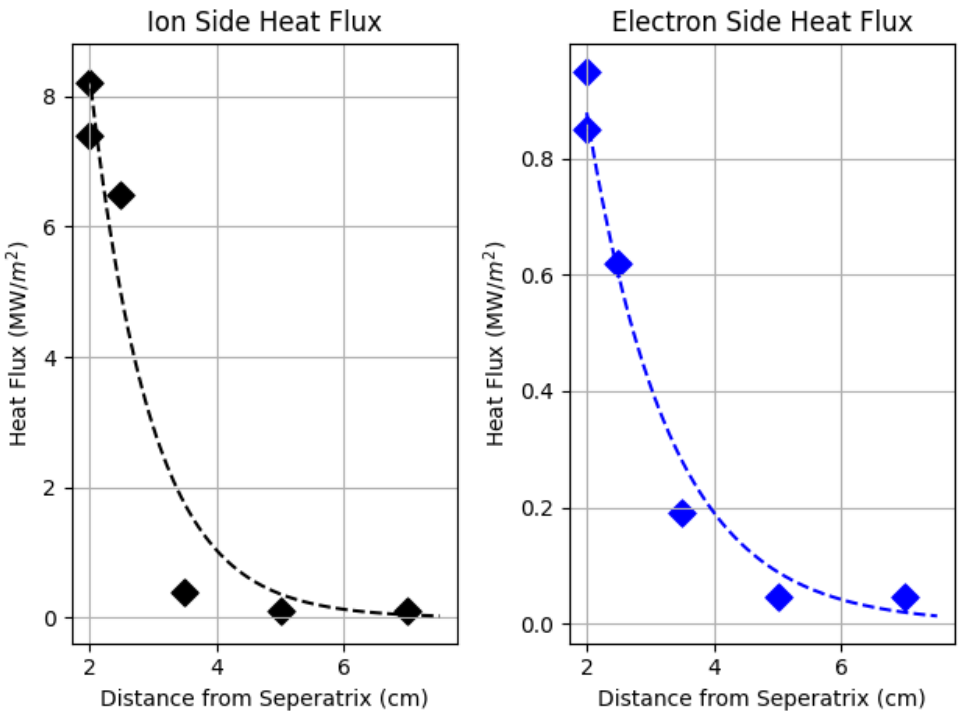

Figure 5.8: Heat fluxes incident on the ion and electron side as a function of distance from the seperatrix. The dotted lines are exponential fits performed on the data which show a good fit with the simulated fluxes suggesting an exponential drop off with distance from the seperatrix

plate is moved closer to the separatrix for shot 95118 (positioned 2.5cm from the separatrix) however, the stored energy drops. This drop is a feature of the variation in temperature change on the plate with position and the effect this has on the recycling within the device.

At this point it is useful to discuss a maximum operational limit for a free surface lithium plate, which is widely agreed to be 450^oC. The limit is decided by the evaporative flux of lithium from the surface of the PFC, too high a flux from the PFC will result in a high density of neutral lithium atoms entering the plasma edge. These neutrals, similarly to the high recycling regime, will collisional cool the plasma edge thereby increasing the ion temperature gradient along with the turbulent transport within the plasma. Alongside this a large evaporative flux of lithium into the core will dilute the plasma worsening the D-T burning efficiency

The mass evaporation of lithium has a further consequence on the plasma health in this setup as for the LiMIT plate there is a fixed lithium content, i.e no continually resupply. As increasing amounts of lithium are evaporated from the plate and redeposited elsewhere in the device the lithium inventory drops and as such it is a distinct likelihood, highlighted in this experimental campaign by the presence of large unwet

(a) R=7cm

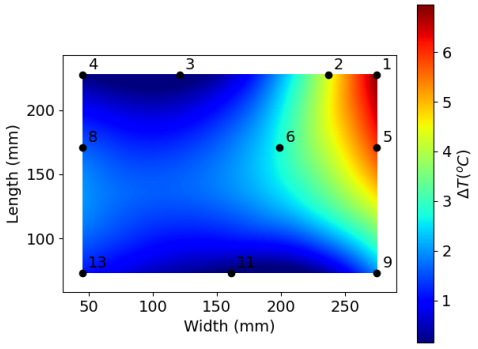

(b) R=5cm

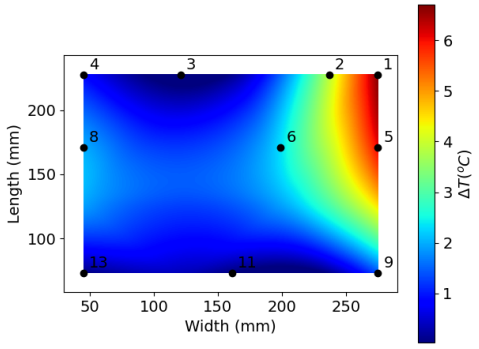

(c) R=3.5cm

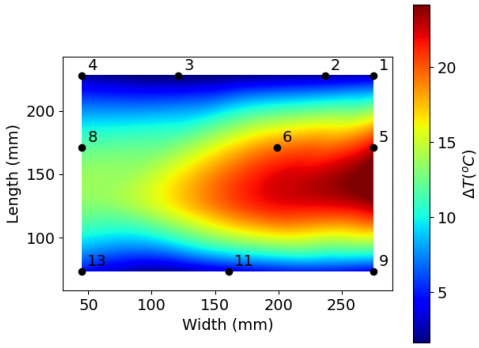

(d) R=2.5cm

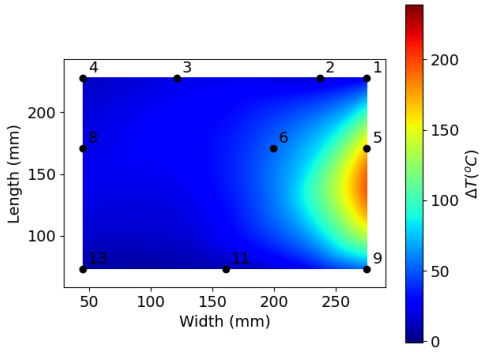

(e) R=2cm

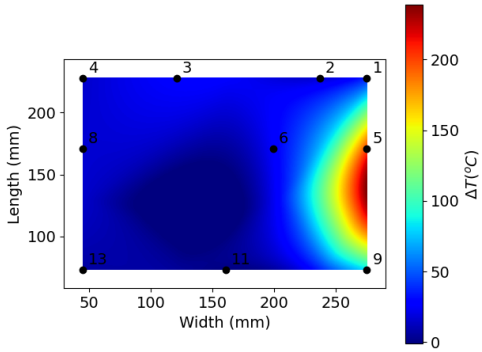

Figure 5.9: Figure showing variation of surface temperature change measured on the LiMIT plate during the 10 second plasma exposure. Note that the scales of each graph are different so that the trends between them can be compared. The localisation of the heat strike to the ion side of the plate becomes more apparent as distance from the separatrix is decreased.

areas on the ion side of the plate, that this leads to areas of the TZM back plate being exposed to the plasma allowing sputtering of high Z impurities into the plasma breaking confinement and radiating away stored energy. With this in mind figure 5.12 highlights the temperature traces for the three central line TCs for shots 95116, 95117 and 95118 with the vertically dashed lines displaying the window of plasma exposure

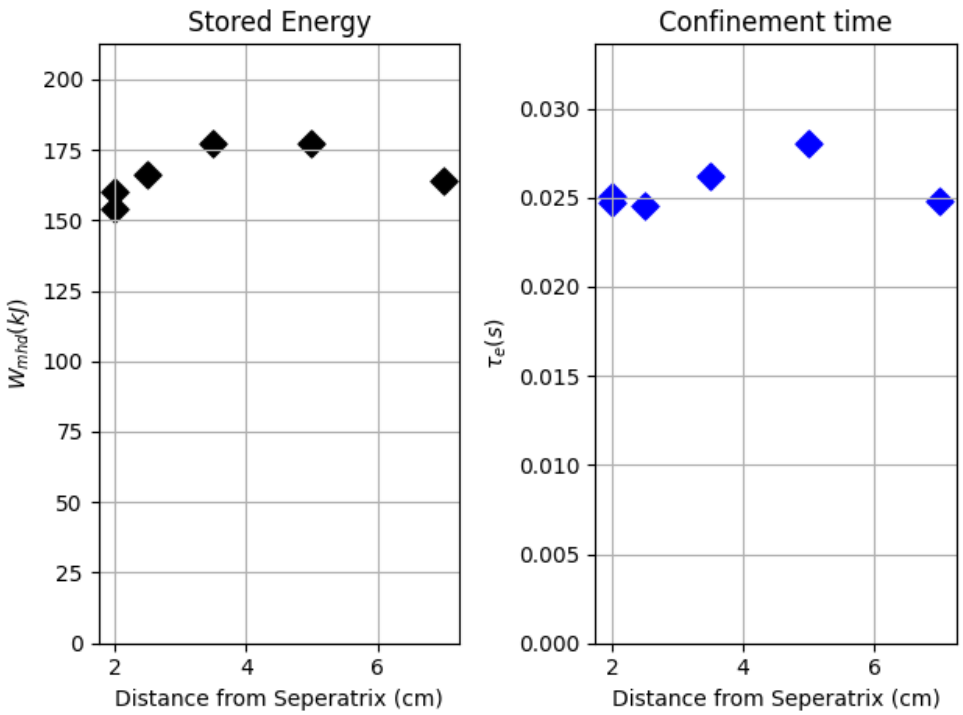

Figure 5.10: Plots of stored plasma energy and confinement time as a function of distance from the seperatrix. Values for both by averaging during flat-top operation and peak when the plate is positioned 5cm from the seperatrix.

and the horizontal dashed line the maximum operational temperature for a free surface lithium PFC as discussed above. As one would expect in all three shots the temperature for both the central and electron side thermocouples stays below the max limit due to the large localisation of the heat flux to the ion side of the plate, an effect further enhanced due to the fast ions produced by the neutral beam heating present in these shots. However, studying figure 5.12a it is clear that the operational limit is exceeded on the ion side when the plate is closest to the separatrix the, note that though the major temperature rise occurs post shot this is a result of the thermal lag due to transport from the lithium surface to the thermocouples. These values are measured by 2mm below the surface of the TZM as such the actual lithium surface temperature will be much higher than this value amplifying the negative effect. The drop in stored plasma energy in 95118 therefore, occurs due to the operational temperature limit being surpassed, leading to mass evaporation on the ion side degrading the benefits of the low recycling regime, this is likely further worsened through the evaporation of the lithium deposited on the walls that benefitted shots 95116 and 95117 and increasing the presence of high Z impurities in the core due to exposure of the TZM plate.

This phenom is further amplified when the plate is moved to 2.0cm from the separatrix in shots 95121 and 95125. Figure 5.11 shows that the plasma in both shots experiences an early drop in stored energy at

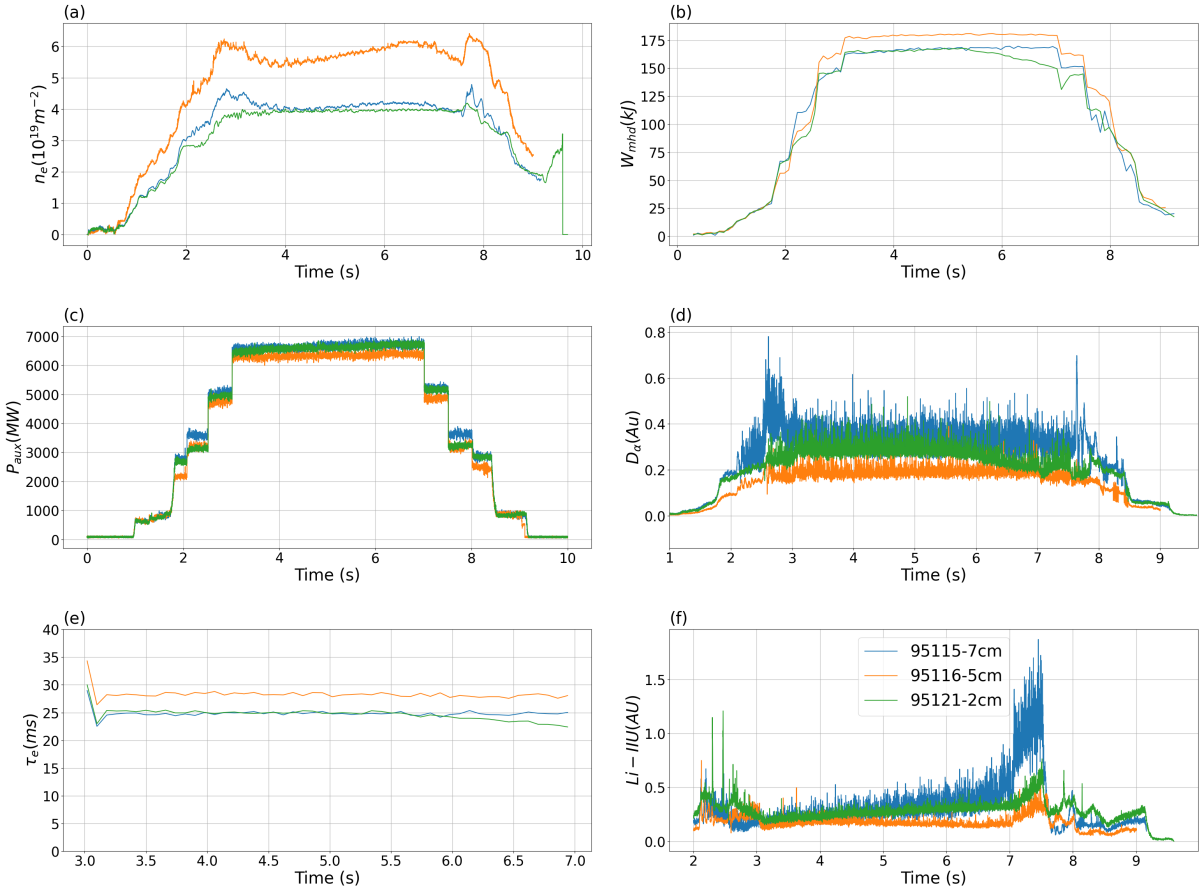

Figure 5.11: Time traces for three positions included in the radial scan (7cm, 5cm and 2cm from the seperatrix) Plots show line averaged density (a), stored plasma energy (b), total auxiliary heating power (c), D_{alpha} (d), global confinement time (e) and the lithium II spectral line measured in the upper divertor (f.)

around 6 seconds into the shot even though the auxiliary power flat top does not change until 8 seconds. This collapse is the result of a far higher total radiative power exhausted by the plasma for these two shots. Figure 5.13 displays the total power radiated by the plasma each second as measured by a fast bolometer. The power radiated in the two shots at 2cm both peak at around 1.2MW at around 6s, corresponding to the drop in stored energy. This value is far higher than reached in the shots further from the separatrix which tend to baseline around 200kW during flat-top operation outside of two spikes in the radiated power for shot 95117 that arise due to an increase in electron density at these points. All this evidence points to 95121 and 95125 suffering a radiative collapse, similarly to that suffered by shot 95061, causing an H-L transition and eventually the extinguishing of the plasma. As no increase in the line averaged electron density is observed it is probable that an influx of high-Z impurities result in this collapse, this is further collaborated by the gradual rise rather than a rapid peak pointing to a build up of impurity. The next question to

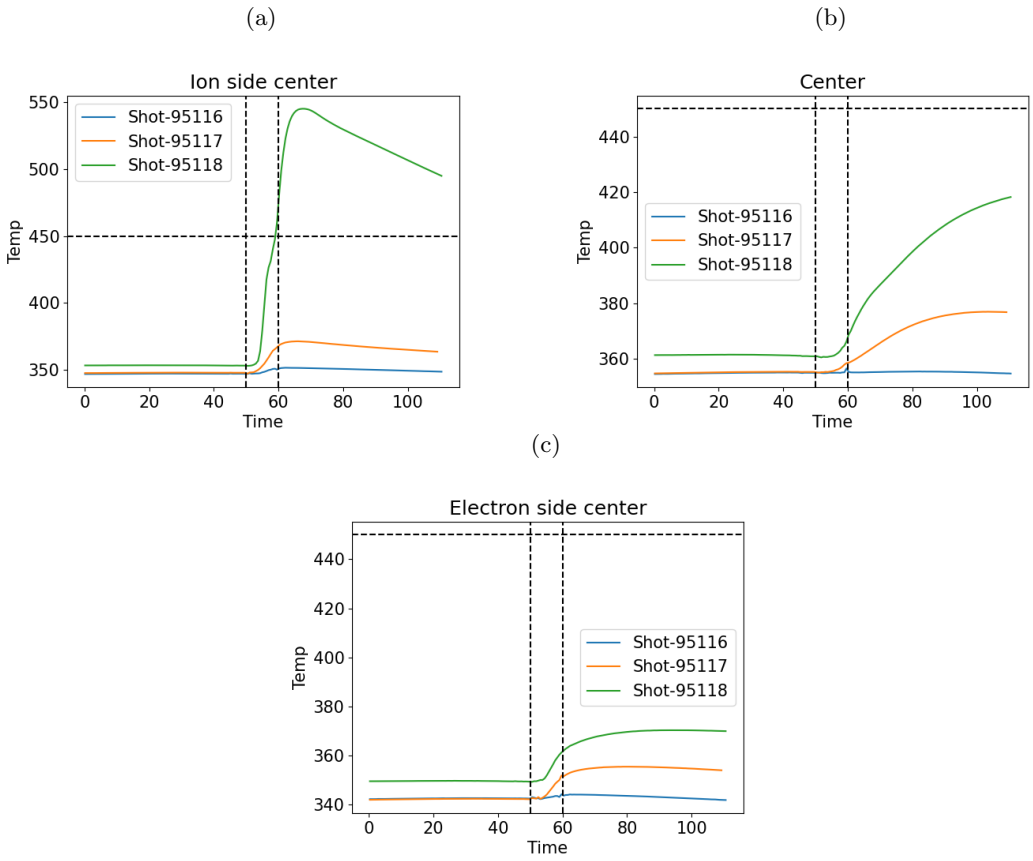

Figure 5.12: Traces for the temperature change measured by the TCs embedded into the TZM back plate for the three shots with the plate closest to the separatrix in the gap scan: 95116 (blue), 95117 (orange) and 95118 (green). The vertically dashed lines highlight the extent of plasma exposure and the horizontal line is the theoretical maximum operational limit for a free surface lithium PFC 450°C. Shot 95118 far exceeds this limit on the ion side of the plate.

answer is if this collapse is the result of the plate or an external factor within the device. As this collapse happened both times the plate was positioned closest to the separatrix and the in-between shots suffered from no such breakdown the signs point to this effect being due to LiMIT rather than a general build-up of impurities during the day. There are two possible causes of high-Z influx: firstly due to the position close to the separatrix the side of the TZM plate was exposed to the fast-ions arising due to the NBI heating and secondly that as these two shots came within the final couple on the run day the plate was no longer fully wet and as such areas of TZM were exposed to the plasma. Both of these scenarios result in the same outcome: molybdenum is sputtered from the plate by the plasma which then travels into the core cooling through collisional excitation and ionisation eventually leading to the radiative collapse of the plasma.

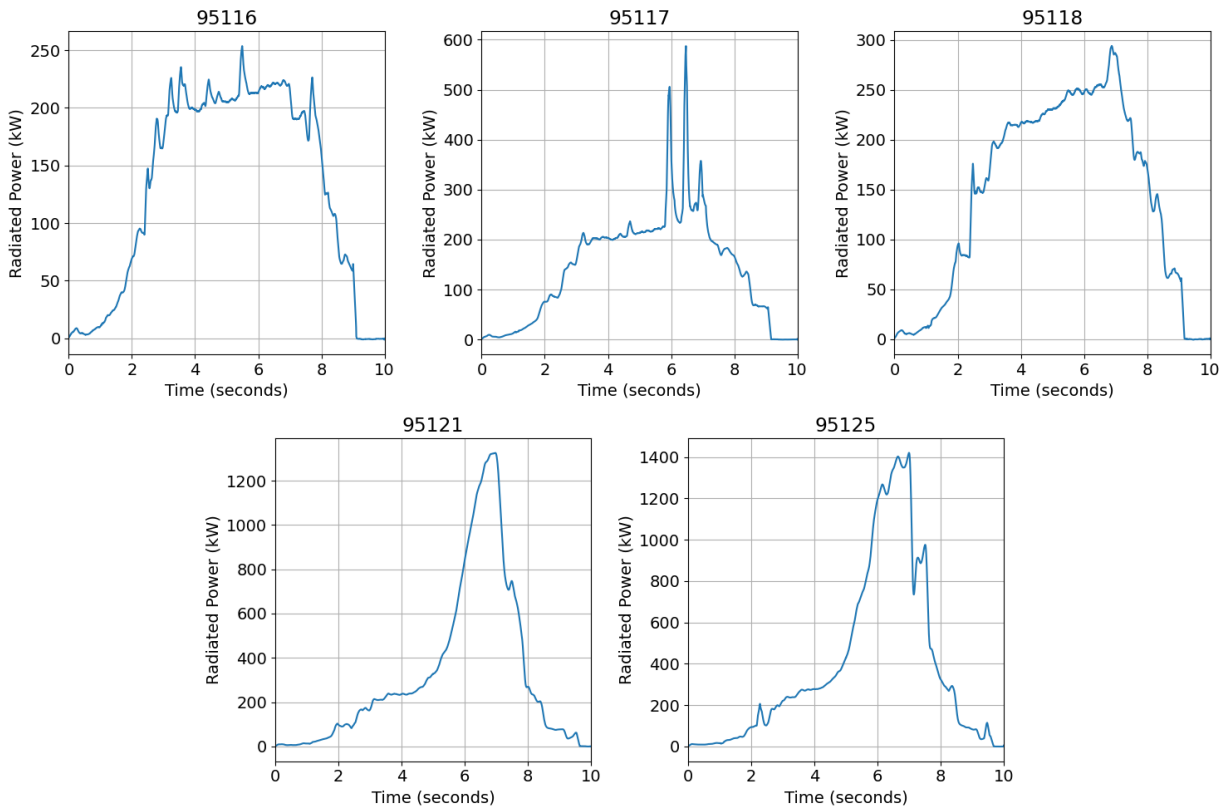

Figure 5.13: Total radiated power measured by the bolometer for shots 95116 5cm from separatrix, 95117 3.5cm from separatrix, 95118 2.5cm from separatrix, 95121 and 95125 both 2cm from separatrix. Shot 95121 and 95125 show far increased radiated power from the plasma core, likely due to these being the shots closest to the separatrix, explaining the radiative collapse both suffer.

5.4 Neutral Beam Heated Shots: Helium Pressure Scan

A second helium pressure scan was run with NBI heating, the parameters for the chosen shots can be found in table 5.4. All the shots were run with 6.7MW of auxiliary heating power, positioned at 2.5cm from the separatrix. The ion and electron side heat fluxes and the temperature change on the ion side of the plate are shown in figure 5.14, as expected when cooling pressure is increased the total temperature rise on the ion side of the plate is reduced. Interestingly however, there is also an observed drop in both the ion and electron heat fluxes on the plate with increasing helium pressure differing from the RF helium scan presented earlier.

Figure 5.15 displays a variety of global plasma parameters for the three shots. The drop in heat flux between the 0MPa shot and 1.5MPa shot can be reasoned to be due to a drop in stored energy within the plasma between the two shots (figure 5.15(b)). Clearly a colder plasma will result in a reduced heat flux at the plate. The drop with the 3MPa shot is a more complex matter to unravel, the plots in 5.15 show an

Table 5.4: Key parameters for the NBI shots 95118,95119 and 95120

Shot #	Distance from separatrix (cm)	Average Limiter Temperature (^{o}C)	Auxiliary Heating Power (MW)	Helium Cooling Pressure (MPa)	Line averaged n_e ($10^{19}m^{-3}$)	Plasma Energy, W_{mhd} (kJ)
95118	2.5	350	6.7	0	3.933	166
95119	2.5	350	6.7	3	4.677	167
95120	2.5	358	6.7	1.5	3.904	160

increased electron density, a decrease in the D_α, an increase in confinement time and a decrease in the local Bohm diffusion at the plate. This points to a decrease in the recycling within EAST during this shot, shown by the D_α decrease, leading to reduced diffusion and as such improved confinement. Two factors could be the cause of this either the increased cooling produces an faster TEMHD driven flow on the plate exposing a cleaner lithium surface to the plasma decreasing local recycling or a large lithium deposition onto the walls or the divertor either in a previous shot or during the 3MPa shot decreases global recycling.

Figure 5.16 plots the lithium flow velocity, calculated using equation 3.9, and the lithium surface temperature measured on the ion-side by an IR camera. The shot without helium cooling (95118) produces the highest computed velocity, $48cms^{-1}$ compared to $31cms^{-1}$ and $25cms^{-1}$ for shots 95120 (1.5MPa) and 95119 (3MPa) respectively, this is due to the far increased lithium surface temperature measured in 95118 producing a steeper temperature gradient across the trench and hence a faster flow rate. As shot 95119 has the slowest lithium flow rate the hypothesis that the lithium replenishment causes the decrease in recycling is incorrect.

The increased lithium surface temperature in shot 95118 combined with the higher heat flux experienced by the plate leads to large lithium evaporation and this is shown by the LiII lines in figure 5.17. The spectral lines display that a large quantity of lithium is present in the upper and lower divertor in shot 95118 therefore, it is theorised that lithium is deposited on the divertors during this shot thus reducing recycling and impurity gettering at the divertor in the subsequent shot. These two factors lead to the improvement in the plasma performance and reduced heat flux experienced by the plate in shot 95119, clearly improved confinement will reduce perpendicular transport and as such the perpendicular heat flux. Shot 95118 also displays a fascinating local behaviour in which the Bohm diffusion rate drops locally at the plate during the flat-top of the shots suggesting a relation between this and the large scale lithium evaporation observed in this shot. A mass lithium leads to an improvement in confinement via impuritiy gettering at the edge of the plasma while also exposing a clean lithium face to the plasma reducing the local recycling at the plate.

This way of thinking and the effects discussed during the radial scans appear to suggest that the lithium

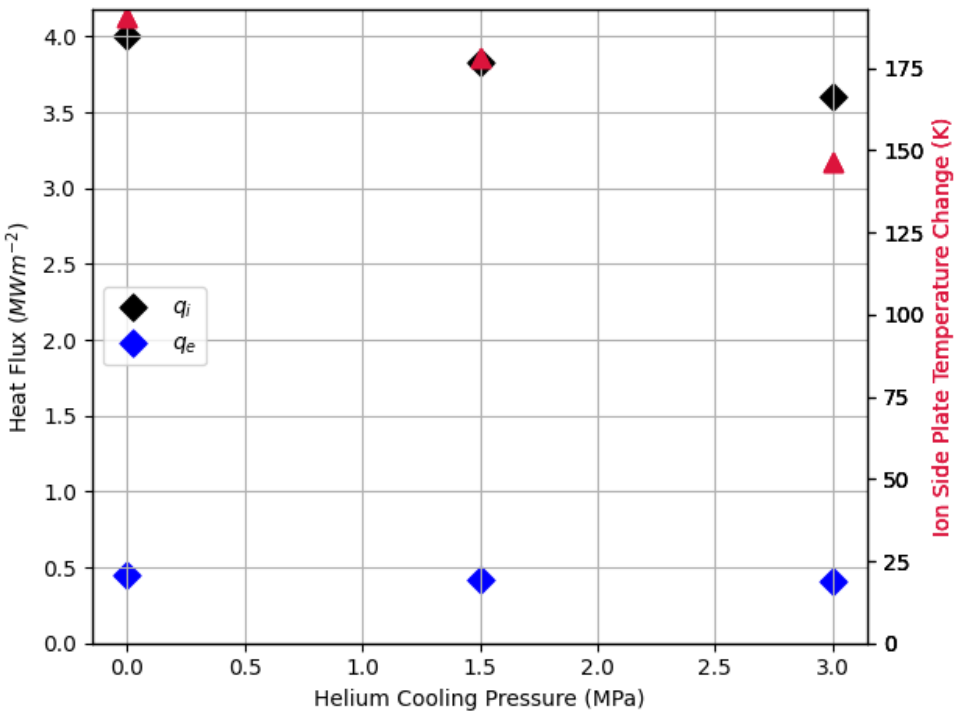

Figure 5.14: Ion and electron side heat fluxes for the NBI heating shots as well as the temperature change on the ion side of the plate for all shots. Both the heat flux and the temperature rise decrease with increasing cooling pressure.

on the plate has a very small effect on the plasma itself and that it is the evaporation and sputtering of lithium off the plate and its re-deposition elsewhere in the device effecting the plasma performance. This is intuitive: the LiMIT plate itself covers a miniscule amount of the total surface area of the device while also being located at the midplane as such the plate can not act as a major particle sink; this would mean that the effect on recycling caused by the LiMIT plate itself is minimal and very little gettering of impurities actually occurs when lithium flows on the plate. It then follows that when lithium is evaporated and enters the plasma and it is more likely to redeposited on the divertor regions of the device (the major particle sinks within a tokomak), this would mean that thin layers of lithium formed on the divertor region after evaporation on the plate lead to the consecutive shot showing improved plasma conditions and after the lithium layer is evaporated or saturated with impurities the benefits are lost.

5.5 Midshot Temperature Flattening

An interesting phenomena was discovered when matching the profiles for the NBI heated shots in COMSOL, certain shots displayed a flattening in their respective ion side profiles during the plasma exposure. To

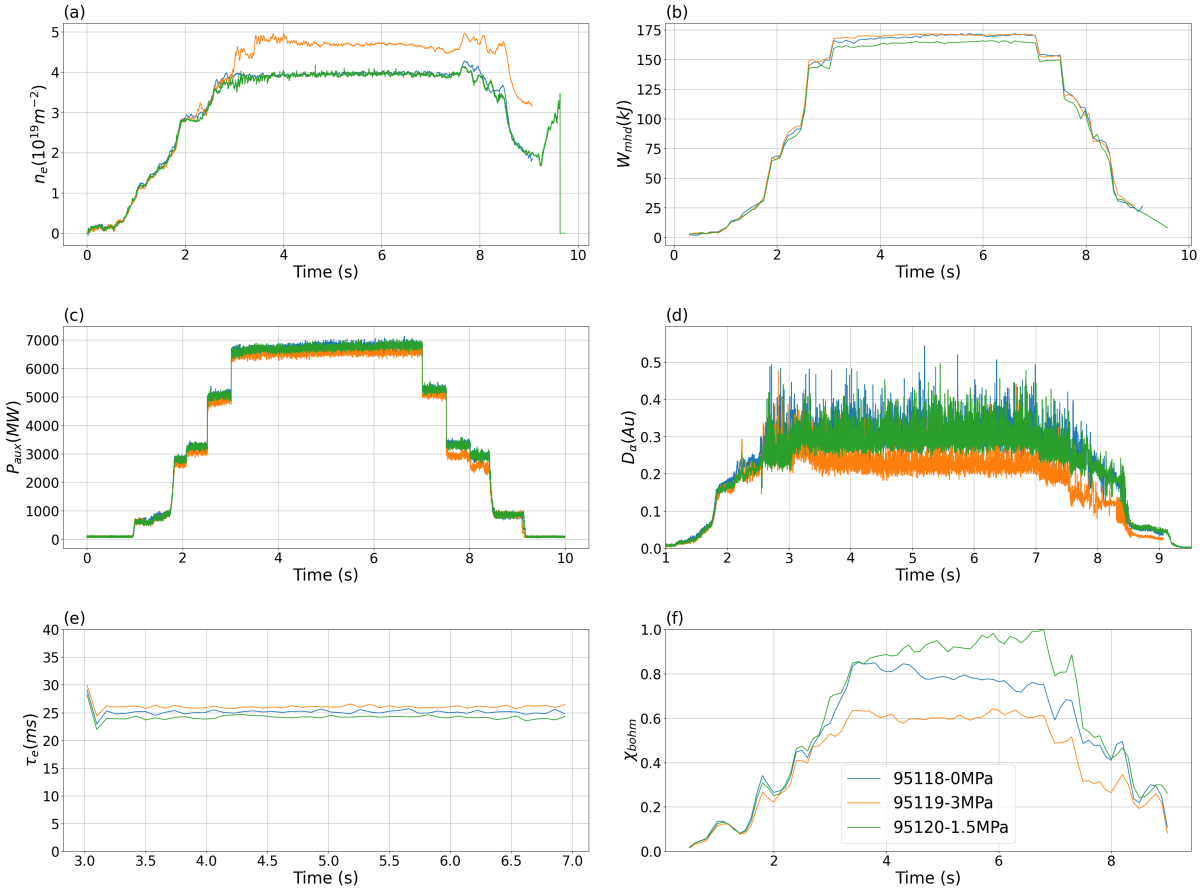

Figure 5.15: Plasma parameters for shots 95118 0MPa helium cooling pressure (blue), 95119 3MPa helium cooling pressure (orange) and 95120 1.5MPa helium cooling pressure (green.) Plots show (a) line averaged electron density , (b) stored energy, (c) auxiliary heating power, (d) D_α, (e) global confinement time and (f) the local Bohm diffusion coefficient at the plate.

highlight this point a comparison between the simulation and experimental data for the three central TCs can be found in figure 5.18 for shots 95118-95120 and in figure 5.19 for shots 95120 and 95125. From the plots it is seen that shots 95119 and 95121 do not display the flattening and act as expected however the three other shots all show varying degrees of flattening. Shot 95118 shows the smallest change out of the three exhibiting a decrease in the rate of temperature rise for 2 seconds halfway through the shot starting ay 725K , 95120 has a larger suppression in the temperature rise that occurs at 775K and shot 95125 has the most extreme effect with a 5 second flattening leading to the max temperature measured by the TC occurring nearly 20 seconds after plasma exposure. Interestingly the flattening for 95125 begins at a temperature of 660K suggesting that this effect is independent of the plate temperature, also as these shots were all run with different cooling pressures of helium it is apparent that this is also not the cause.

The large deviation between these traces and the model leads to the conclusion that there is physics

(a)

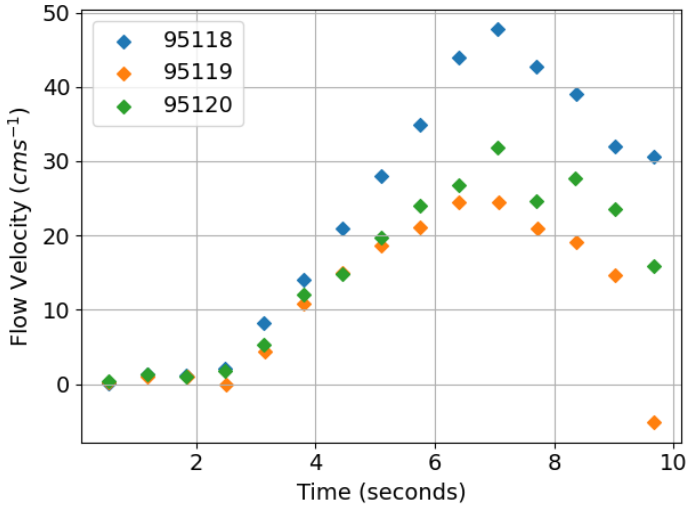

(b)

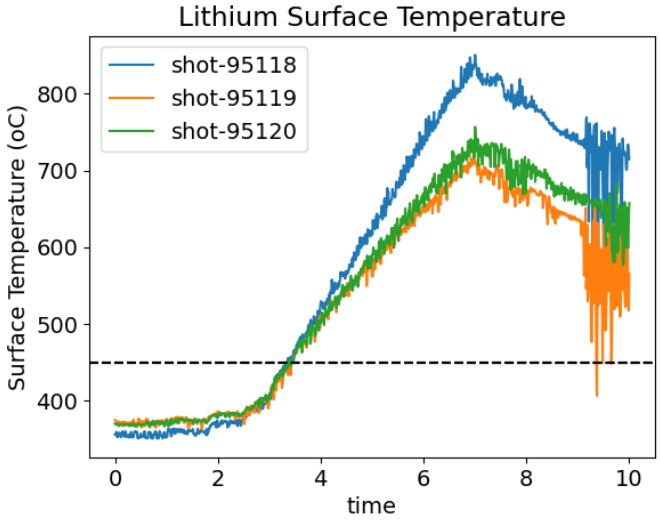

Figure 5.16: Figures showing (a) the calculated lithium velocities and (b) the lithium surface temperature measured on the ion-side of the plate by an IR camera. The shot without helium cooling (95118) produces the highest flow velocity on the ion side due to the higher temperature of the lithium surface leading to a much steeper temperature gradient across the trench. This highlights that the reduction in global recycling for shot 95119 isn't caused by increased TEMHD flow upon the plate.

of the interaction between the plate and the plasma missing from the COMSOL model that produces the flattening and a number of suitable candidates have been proposed and will be discussed here. Firstly, it was reasoned that there could have been a shift/confinement loss in the plasma mid-shot in the shots exhibiting the flatten of the temperature profile. This shift could have moved the plasma strike point such that it was positioned on the side of the plate; the distance to the ion side TC is longer from the side of the plate

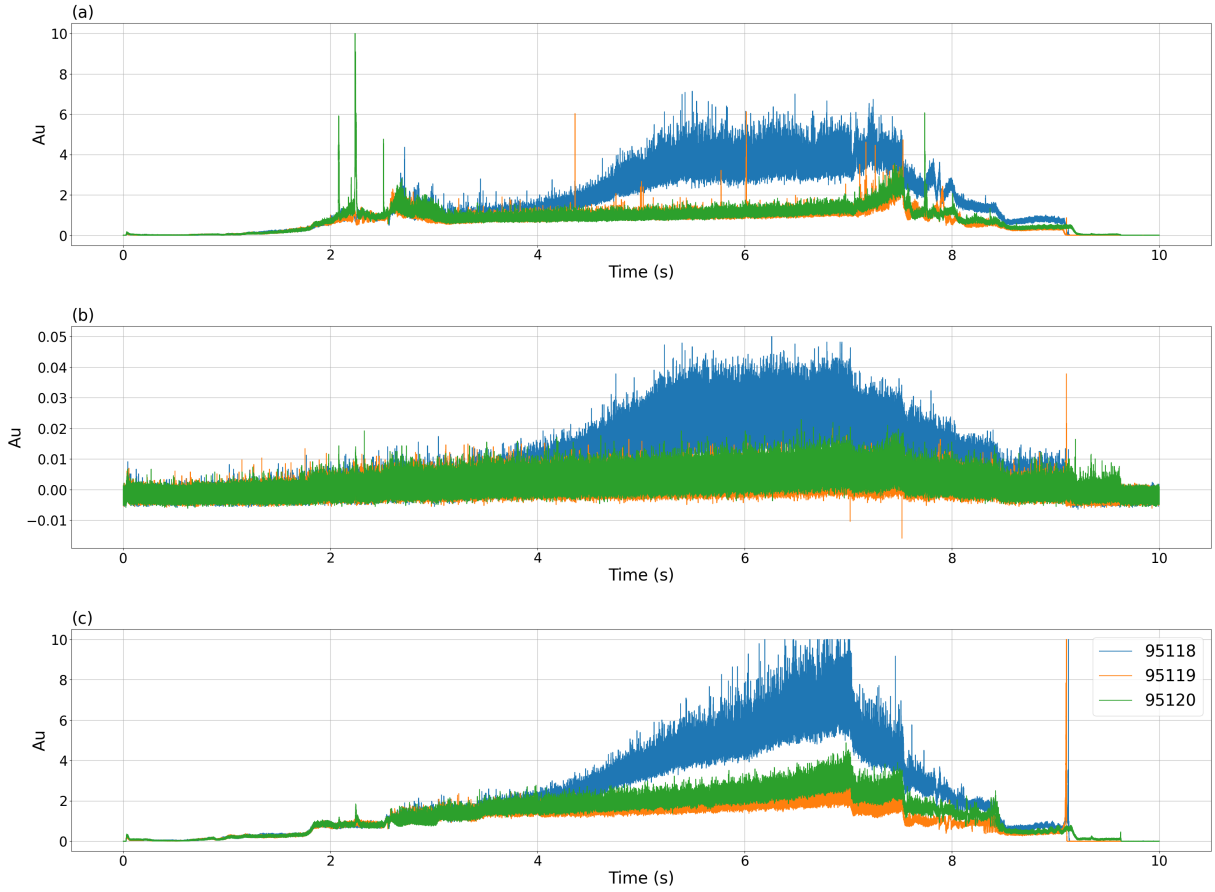

Figure 5.17: Time traces of Li II spectral lines in (a) the upper divertor, (b) the midlpane and (c) the lower divertor for shots 95118 0MPa helium cooling pressure (blue), 95119 3MPa helium cooling pressure (orange) and 95120 1.5MPa helium cooling pressure (green.) The lines for shot 95118 displays a large influx of lithium to the upper and lower divertor likely leading to lithium coating of both regions explaining the decrease in recycling observed in the next shot.

than the front. Increasing the distance between the heat strike and the TCs would induce a thermal lag as heat is transferred through the TZM flattening the temperature profile post shift and explaining the rise in temperature after the shot. To explore this effect the surface temperature change of all the NBI shots have been computed as this should highlight if the heat strike shifted mid-shot, these are shown in figure 5.20. The scales for each plot are different to allow for the general heat-strike shape to be compared. All of the shots show a near identical temperature response over the plasma window, especially on the ion-side, with the slight deviations on the electron side and the middle of the plate arise from the change in cooling pressure between shots, discrediting the hypothesis that a plasma shift mid shot produced the temperature flatten seen in the couple of shots.

(a)

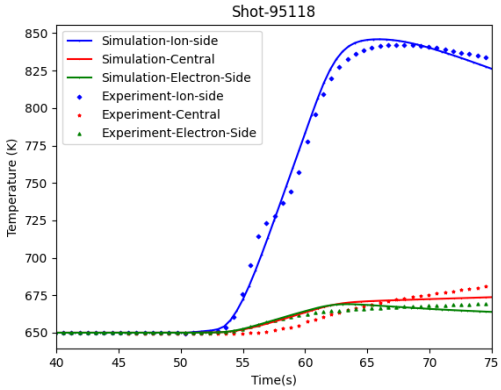

(b)

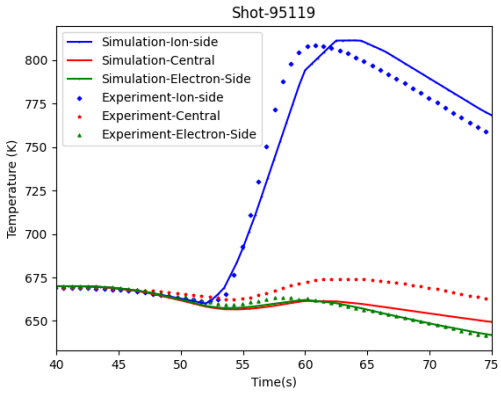

(c)

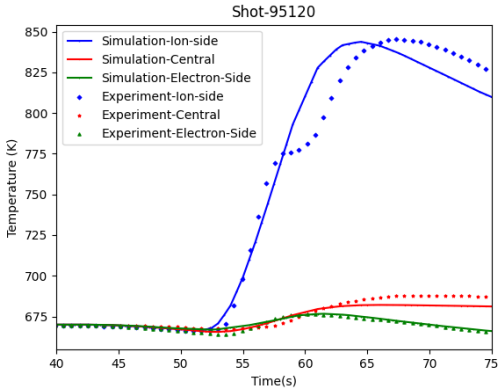

Figure 5.18: Comparison of matched simulation temperature profiles and experimental profiles for the central TCs for shots 95118 (5.18a), 95119 (5.18b) and 95120 (5.18c.) Shots 95118 and 95120 display a mid-shot flattening in their temperature traces during plasma exposure.

So there was no plasma shift, however it is possible that the plasma was detached from the plate for a period of time leading to a pause in the temperature increase on the plate. This detachment could be

(a)

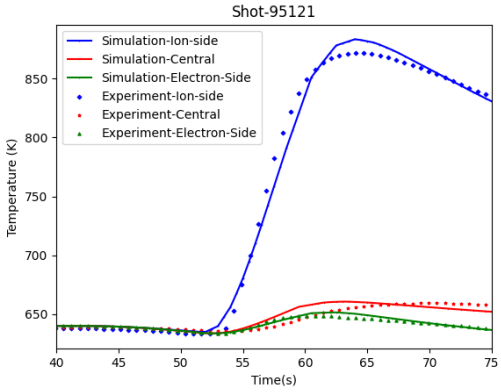

(b)

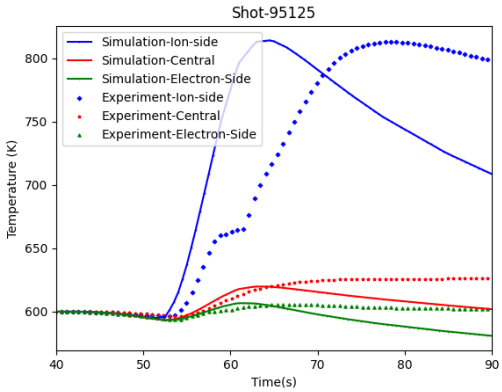

Figure 5.19: Comparison of matched simulation temperature profiles and experimental profiles for the central TCs for shots 95121 (5.19a) and 95125 (5.19b). Note that 95125 has been plotted over a longer time window (over 90s rather than 75s) so that its full behaviour can be displayed.

the result of vapor shielding due to the much higher heat flux faced by the plate during these shots, this shielding would begin to occur after the plate temperature surpassed 600^oC and would dissipate the energy from the plasma through neutral-ion collisions effectively detaching the plasma from the plate for a period of time after this the lithium is redeposited onto the plate leading to the temperature rise post-shot. To elucidate this matter the model outlined in section 3.2 is applied to these shots and the results for the heat flux dissipated by the vapour cloud for each shot are shown in figure 5.21. Before discussing the results it is my belief that it is important to discuss how the values were obtained and any potential pitfalls in the method. The main point of concern with the analysis is how the surface temperature of the lithium is measured, in order to calculate evaporation rate. The surface temperature was computed using the video from an infra-red camera with line of sight of the plate, the issue with using IR data is that it is dependant on the emissivity of the medium is recording and needs to be calibrated accordingly this clearly means

(a) 95118

(b) 95119

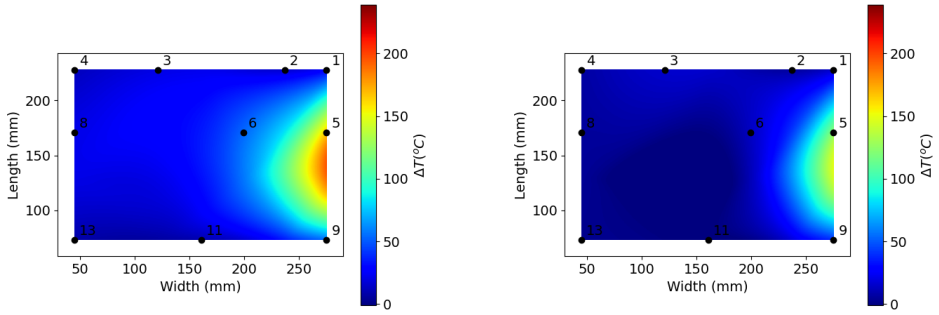

(c) 95120

(d) 95121

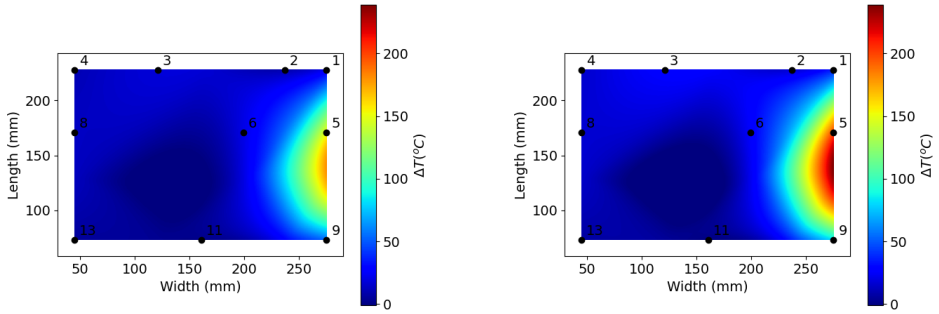

(e) 95125

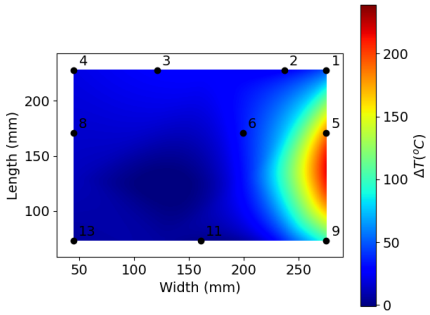

Figure 5.20: Surface temperature change for shots 95118 5.20a,95119 5.20b,95120 5.20c, 95121 5.20d and 95125 5.20e. The general shape of the strike points agrees between all the NBI shots with minor differences arising due to: LiMIT in shots 95121 and 95125 being positioned closer to the separatrix and hence experiencing more intense heating and the variation in helium cooling pressure applied across the plate in the shots.

that a difference between calibrated and actual emissivity will lead to surface temperatures deviating from their actual values. This problem will appear in this analysis due to the difference in emissivity between lithium and TZM as well as the fact that the emissivity of lithium is vastly increased with the unavoidable impurity build up within the lithium which will further disturb the measurements. Hence, it must be assumed during this analysis that the conditions on the plate observed by the IR camera were similar for each shot in order for a comparison between them to be made. This assumption combined with the fact that

the IR temperature is the maximum lithium temperature (i.e not averaged across the plate) and the vast number of assumptions made when deriving the model mean that the computed vapor shielding should be seen as a method to compare shots rather than accurately calculate the energy dissipated by the vapor shield.

With these caveats explain lets return to the figure, shot 95118 shows the highest level of vapor shielding with a peak value of around $6.3MWm^{-2}$, this would appear to validate the theory that the temperature flattening is caused by vapor shielding however shots 95120 and 95125 which exhibit more extreme flatten of their respective temperature profiles produce vapor clouds that exhaust far less power (95120 peak $\approx 1Mwm^{-2}$ and 95125 peak $\approx 0.7MWm^{-2}$) suggesting there are different processes causing this flattening. This theory is also discredited by a study of the surface temperature of the plate during the shots shown in figure 5.22 if vapor shielding regime was reached one would expect to see the surface temperature profile drop and then flatten when the plasma is detached yet no such behaviour is observed in the figure, this effect was shown during testing of a CPS system within Magnum-PSI to be on the order of 200^oC drop for multiple seconds [90]. A vapor shielding regime is also characterised by its oscillatory nature, i.e once the cloud is formed the vapor dissipates heat cooling the surface decreasing the size of the vapor shied this in turn leads to an increase in the plate temperature reforming the vapor cloud reducing the surface temperature once again, though no such behaviour is observed here. Another possible detractor for the IR camera data arises here in that one can not say with certainty whether the temperature measured is that of the lithium on the surface or of the vapor shield itself.

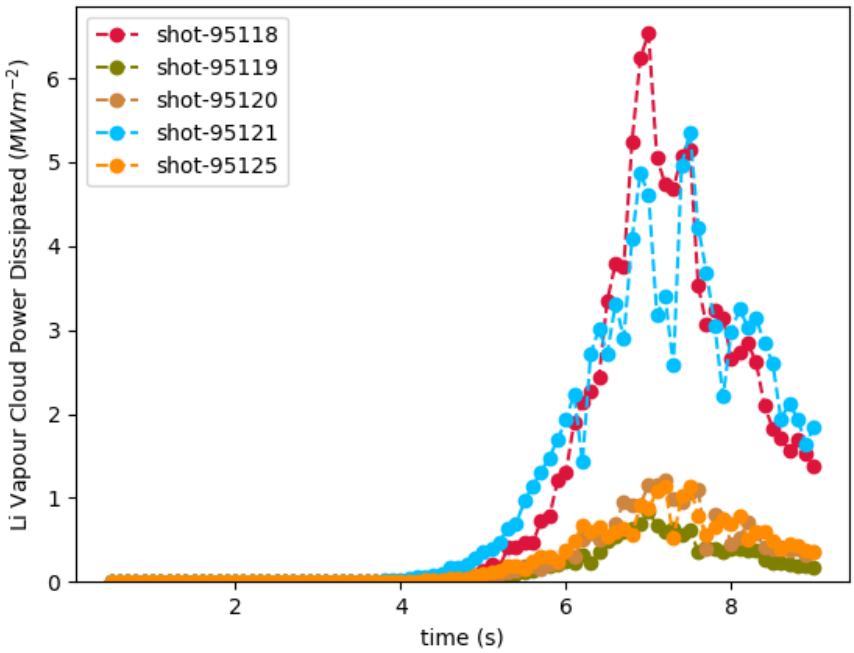

Figure 5.21: Calculated power dissipated by the lithium vapor shield during plasma exposure calculated at the ion-side of the plate. Shot 95121 dissipates more power in its vapour cloud than 95125 highlighting that vapour shielding is not the cause for the flattening of the temperature profile observed.

The final analysis of this flattening used equation 3.9 to calculate the flow velocity due to TEMHD for each of the shots. Plots of flow velocity over the shot window are shown in figure 5.23, equation 3.9 does not include the EM pumping present from the reservoir to the plate however this is the same for all shots so the overall velocity trends should not be changed by its inclusion. From the plots one can see that the three shots that display the mid-shot flattening do reach higher peak TEMHD velocities with 95118,95120 and 95125 reaching velocities of $44cms^{-1}$, $31cms^{-1}$ and $38cms^{-1}$ respectively higher than the $24cms^{-1}$ and $26cms^{-1}$ flows calculated for shots 95119 and 95121. These flow velocities are higher than expected as discussed before this IR camera data is measured on the ion side (i.e the side with the most extreme temperature gradient) therefore the velocity elsewhere on the plate will be lower alongside this issues in the emissivity calibration produce surface temperature measurements that are higher than actual. With this in mind figure 5.24 shows the computed values of the heat stored in the lithium over the plasma window calculated using equation 3.8 and then averaging over the plate. Even with the increased temperature gradient the heat stored in the lithium is many orders of magnitudes lower than that stored in the TZM plate or in the vapour cloud ($\sim 10kWm^{-2}$ compared to $\sim MWm^{-2}$.) Though heat is not stored in the lithium the increased flow velocity may result in heat being transported further down the plate the temperature change of TC9, the

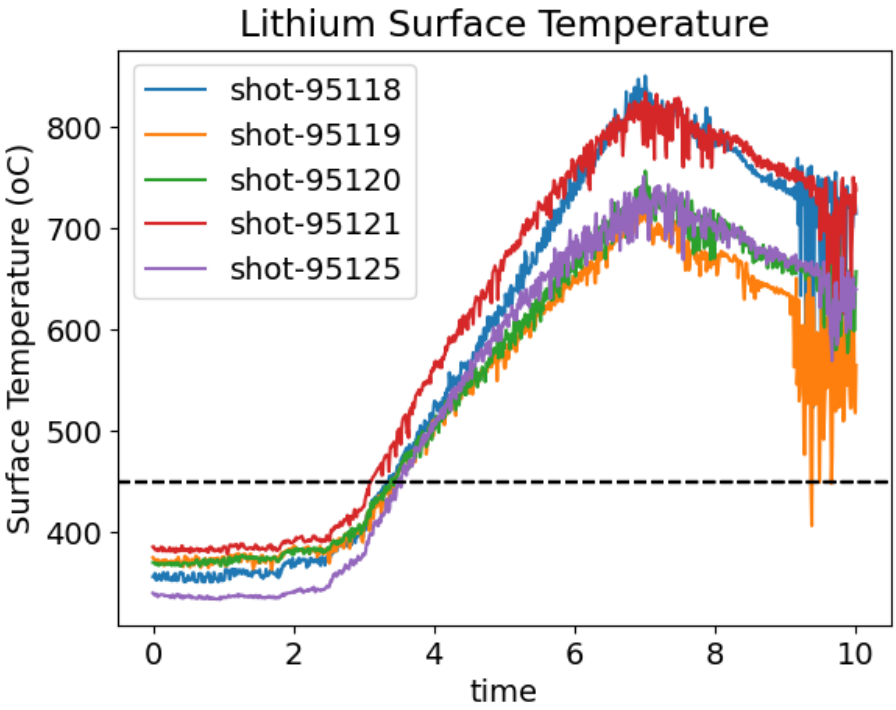

Figure 5.22: Lithium surface temperature during the LiMIT plasma exposure as measured on the ion-side of the plate by an IR camera.

TC located beneath TC5, is shown in table 5.5. The shots that exhibit a flattening of their temperature profiles during the plasma exposure do indeed have a larger temperature change when compared to shots at the same radial position within EAST that have no flattening thereby suggesting that the increased flow velocity in these shots is transporting heat down the TZM plate.

To summarise this section the increased flow velocity observed does not lead to a noticeable increase in the heat stored convectively within the lithium but does transport the heat further down the TZM plate causing a flattening in the temperature profile in the ion side TC under the strikepoint, as the plasma heating subsides the lithium flow due to TEMHD slows and therefore, so does the transport of heat down the plate leading to the temperature rise post-shot observed in the profiles with flattened profiles.

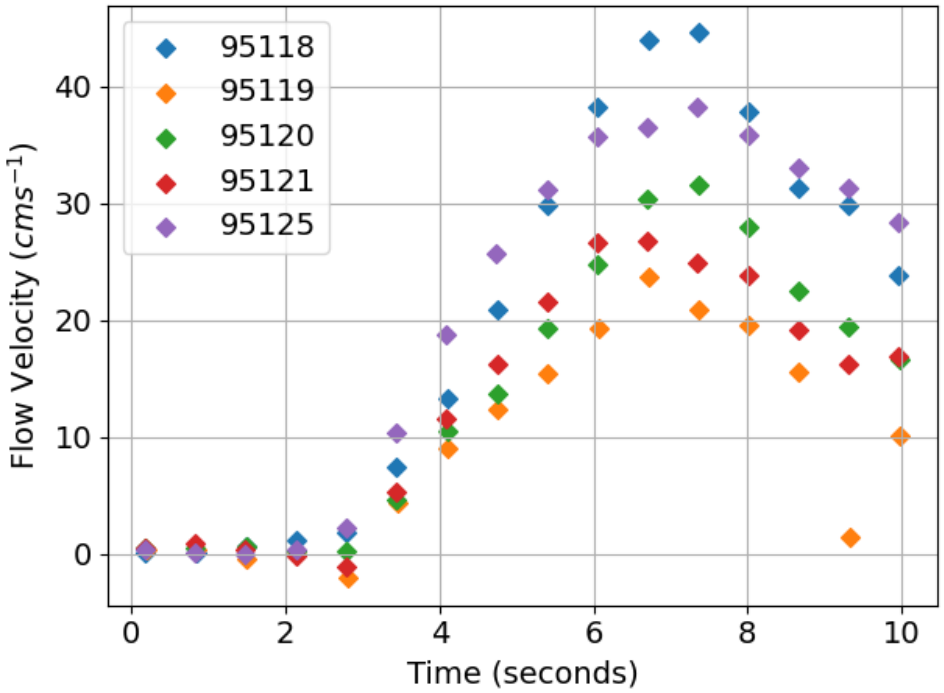

Figure 5.23: Plots of calculated TEMHD velocity on the LiMIT plate over the plasma window. The shots that have a flattening of their temperature profiles during the plasma exposure display higher flow velocities compared to those without such behaviour.

Table 5.5: Temperature change for TC9, TC located on the bottom of the ionside, for each of the NBI shots studied. The shots that display temperature flattening produce a larger temperature change compared to their respective shots that do not exhibit flattening suggesting that heat is being transported down the plate due to the increase lithium flow rate for these shots.

Shot #	Distance from separatrix (m)	Temperature Change (^oC)
95118	2.5	28.7
95119	2.5	17.5
95120	2.5	24.5
95121	2	37.3
95125	2	49.9

5.6 Post-Mortem

The post-mortem photos of LiMIT pointed to no macroscopic damage caused to the plate during the exposure in EAST, figure 5.25d, which is a marked improvement on the previous FLiLi runs which displayed signs of damage, figures 5.25a and 5.25b. The root cause of this could be the improved lithium coverage present on the LiMIT plate. Plate coverage is calculated by assuming that areas of plate where lithium wets to the surface were covered, i.e areas of the plate covered with lithium compounds. The wetting has

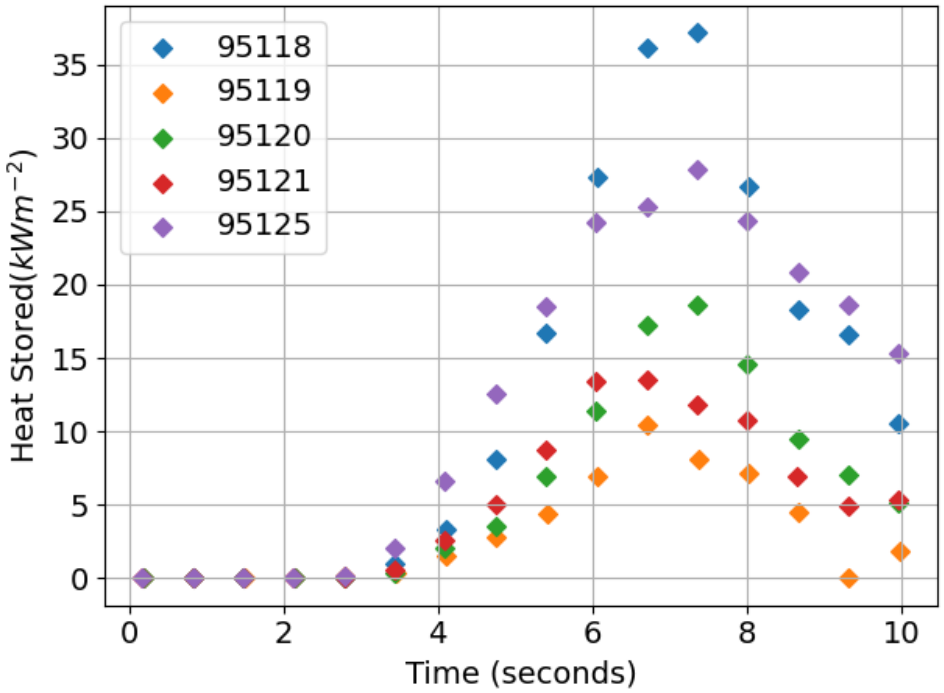

Figure 5.24: Plots of calculated convective heat stored in the Lithium over the plasma exposure. The heat stored convectively within the lithium (on the order of $\sim 10 kWm^{-2}$ is far smaller than that which is conducted into the TZM plate ($\sim MWm^{-2}$.)

shown marked improvement with each generation with a coverage of 30% with the first generation FLiLi plate improving to around 70% with the second generation plate, generation III plate having 80% coverage and finally the LiMIT plate which is estimated to have 87% plate coverage. In the early FLiLi designs the lithium streamed together after distribution forming narrow jets down the plate, this arises due to the high surface tension present in lithium ($405 mNm^{-1}$) wanting to pull the flow together, leaving large areas of the plate unwet. This streaming effect was negated with future iterations by improving the uniformity of the lithium distribution at the top of the plate. The post-mortem figure of LiMIT shows none of this jetting as the trenched nature of the plate suppresses the flow from pulling together. The one large rectangular unwet area near the electron side of the limit plate is theorised to have arisen from a blockage in the distribution channel, though lithium compounds are seen just below the distributor it is reckoned that lithium creep from the plate either side of the unwet region lead to their presence. The distribution channel on the LiMIT plate consists of many pinholes along the plate through which lithium can flow. Any blockage of one or a group of these holes, caused by either an impurity or lithium freezing, will result in an area of the plate left bare. This design could prove especially problematic with long term lithium operation as with increasing impurities, most notably lithium hydroxide, lithium becomes more viscous and can ultimately form a

slurry making pumping through tiny holes near impossible. With this in mind it is a vital part of the design work for new limiters that new methods of distribution are developed to produce even and uniform flows.

(a)

(b)

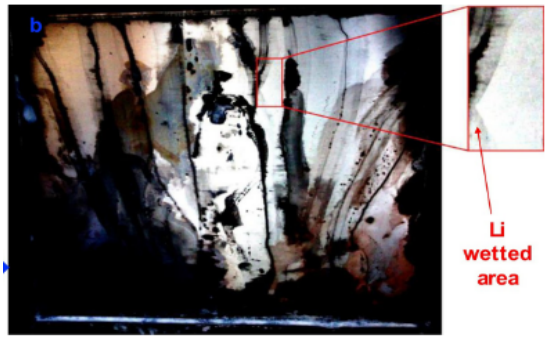

(c)

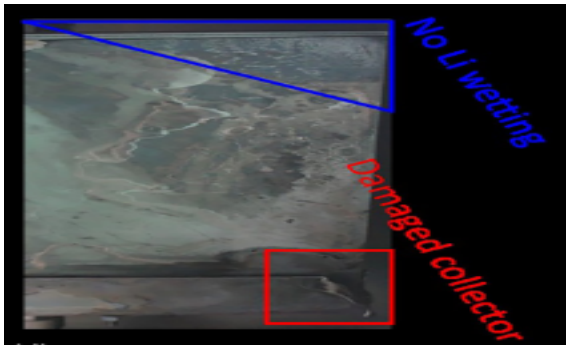

(d)

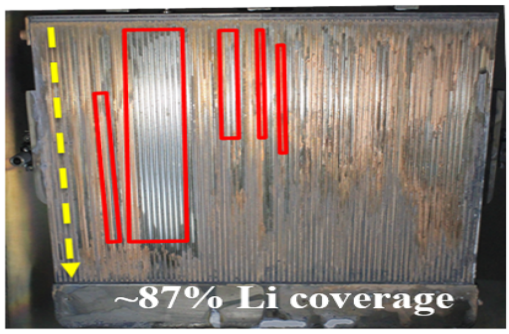

Figure 5.25: Post-Mortem shots from the four generations of lithium limiters ran in EAST, highlighting the lithium wet areas present on the surface of each plate. (a) FLiLi Gen I [8], (b) FLiLi Gen II [8], (c) FLiLi Gen III [7] and (d) LiMIT [9]. Each generation of limiter has shown increasing lithium plate coverage increasing from 30% in gen I to 87% for LiMIT. LiMIT also suffered no macroscopic damage to the TZM plate during testing.

Chapter 6

Conclusions

Lithium PFCs offer an attractive solution for the future PMI of fusion reactors. To further research into liquid metal PFCs a LiMIT style limiter was inserted into EAST and exposed to the plasma. Shots were run to discern the effect of helium cooling pressure, auxiliary heating power and radial positioning on the performance of both LiMIT and the plasma. Alongside the experimental work a COMSOL model has been developed to replicate the conditions experienced by the LiMIT plate during the exposures allowing for the heat absorbed into the TZM backplate of LiMIT during a shot to be computed. This chapter will first summarise the main results from the EAST campaign and the respective simulations and then will discuss further work building on the work presented.

6.1 Heat Handling Ability of LiMIT

While optimising the COMSOL model it was observed that modelling the heat stripe as constant across the plate was inaccurate and in fact the strike points are localised on the sides of LiMIT; this arose due to the angle between the flat plate leading to a portion of the parallel heat flux to be incident on the plate at it's edge. It was also discovered that the heat flux on the ion side was far in excess of that on the electron; due to the larger gyro-radii of ions it is theorised thast many more ions strike the plate producing a much more intense interaction between the plate and the plasma on the ion side.

Once the model was fully developed it was discerned that for RF heated shots, with plate temperatures below 450^oC, changing helium cooling pressure has no effect on plasma performance but does allow for LiMIT to handle an equal heat flux with a far reduced temperature response, for a heat flux of $\sim 1MWm^{-2}$ 3MPa of helium cooling resulted in a temperature rise of 15^oC on the plate compared to 40^oC without cooling. During the sweeps of RF power from 2.9-3.9MW, lithium was shown to condition the plasma. After a large evaporation event from the plate the plasma operation was able to transition from low to high confinement and eventually reached a point where the plasma stayed in H mode for the full duration of the flat-top. The heat flux was found to decrease exponentially with distance from the separatrix during the

sweep of LiMIT's radial position. The best plasma performance was achieved when the plate was situated 6cm from the seperatrix, this shot was preceded by one with large lithium evaporation, at closer positions the radiated power from the plasma greatly increases due to the presence of a strike point on the side of LiMIT sputtering TZM into the plasma core, this causes a radiative collapse of the plasma when the plate is 2cm from the separatrix. With NBI heating large lithium evaporation events occurred for multiple shots as the limiter temperature far exceeded the 450^oC limit. Shots following these events displayed increased confinement, electron density and stored energy. This effect was caused by lithium evaporated from the plate being deposited onto the divertor region of the plate decreasing recycling in the next shot, seen by the reduction of the D_α line during these shots, and by increasing impurity gettering.

In terms of the power handling shot 95121 provided the most extreme conditions faced by LiMIT during the plasma exposure, this was the shot with 6.7MW of auxiliary heating with the plate positioned 2cm from the separatrix. For this case an ion-side heat conductive flux of $8.2MWm^{-2}$ was calculated in COMSOL for the heat flux conducted into the plate and a further $5MWm^{-2}$ dissipated by the vapor cloud (though this value should be taken with a pinch of salt due to the problems with the methodology discussed above.) These values emphasis the incredible heat handling capability of the plate, even taking a very conservative estimate of the power exhausted by the vapor shield the plate of a couple of MWm^{-2}, LiMIT still withstood a heat strike $10MWm^{-2}$ (the agreed limit for tungsten PFCS and the nominal limit for ITER relevant divertor heat fluxes) without sustaining any macroscopic damage to the plate. More impressively, a large number of the shots approached or overcome the $10MWm^{-2}$ limit, highlighting the ability of LiMIT to withstand multiple exposures to high temperature plasma.

6.2 Future Work and Limiter Designs

The experiment was not without its issues however and it is important to mention them and talk of solutions in order to improve the next run campaign. Firstly, the heat strike was very localised on the electron side and ion side of the plate, with the ion side experiencing a much higher heat flux when comparing the two. This localisation effect became more pronounced the closer to the separatrix the plate was positioned. This issue arises as the plate is flat with the magnetic field lines parallel at its centre but curving away at the edges, this angle between the field lines and the plate meant that a component of the parallel heat flux was incident on the plate at the edges and as $q_{||} >> q_\perp$ this tended to concentrate heat flux on the plate edges. To rectify this is a challenge: one could design a plate that contours to match the field lines of the device

but that increases the engineering complexity of the plate greatly; instead one may need to heed this effect and design the plate cooling accordingly. This point ties into another issue with the current design: the lack of cooling beneath the ion-side of the plate. This region experienced heat fluxes far in excess of any other region of the plate and with the detraction of cooling here, especially during the high power NBI shots, the plate consistently exceeded 450^oC producing large lithium evaporation exposing the TZM plate to the plasma which lead to a radiative plasma collapse when the plate was located near to the separatrix. It is obvious that to prevent this error the cooling lines need to be designed such that they cover the entirety of the central profile of the plate. It is worth noting at this point that even if helium cooling was present on the ion-side of the plate, the temperature probably would have still exceeded the max operational limit; though this has the benefit of testing the maximum heat handling capability it suggests that for study of lithium benefits on plasma performance one is better placed positioning the plate at a greater distance from the separatrix. A final issue shows itself not with the plate but with the runs performed on the day. The omittance of the same shots to start and bookmark the campaign is an oversight, as such a pair/group of shots would have allowed for a direct analysis on the effect on the EAST plasma of prolonged LiMIT exposure.

These future ideas will be supplemented by experimental work at UIUC utilising the new MEME chamber. The first of the UIUC experimental campaigns will aim to achieve full plate coverage and uniform flow by testing a variety of different post distribution designs to elucidate the best design for future lithium PFCs.

References

[1] A. Horvath and E. Rachlew, "Nuclear power in the 21st century: Challenges and possibilities," *Ambio*, vol. 45, no. 1, pp. 38–49, 2016.

[2] Y. Xu, "A general comparison between tokamak and stellarator plasmas," *Matter and Radiation at Extremes*, vol. 1, no. 4, pp. 192–200, 2016.

[3] A. E. Costley, "Towards a compact spherical tokamak fusion pilot plant," *Philosophical Transactions of the Royal Society A: Mathematical, Physical and Engineering Sciences*, vol. 377, no. 2141, 2019.

[4] Q. Yang, Z. Chen, Q. Du, H. Xu, G. Zuo, J. Ren, J. Hu, Y. Song, J. Li, F. Ding, *et al.*, "Development of the flowing liquid lithium limiter for east tokamak," *Fusion Engineering and Design*, vol. 124, pp. 179–182, 2017.

[5] P. Fiflis, L. Kirsch, D. Andruczyk, D. Curreli, and D. N. Ruzic, "Seebeck coefficient measurements on Li, Sn, Ta, Mo, and W," *Journal of Nuclear Materials*, vol. 438, no. 1-3, pp. 224–227, 2013.

[6] M. Szott and D. N. Ruzic, "2-D moving mesh modeling of lithium dryout in open surface liquid metal flow applications," *Fusion Engineering and Design*, vol. 154, no. January, p. 111512, 2020.

[7] G. Z. Zuo, C. L. Li, R. Maingi, X. C. Meng, Z. Sun, W. Xu, Y. Z. Qian, M. Huang, Z. L. Tang, D. H. Zhang, L. Zhang, Y. J. Chen, S. T. Mao, Y. M. Wang, H. L. Zhao, D. Andruczyk, K. Tritz, X. Z. Gong, and J. S. Hu, "Results from a new flowing liquid Li limiter with TZM substrate during high confinement plasmas in the EAST device," *Physics of Plasmas*, vol. 27, no. 5, p. 052506, 2020.

[8] J. S. Hu, G. Z. Zuo, R. Maingi, Z. Sun, K. Tritz, W. Xu, Q. X. Yang, D. Andruczyk, M. Huang, X. C. Meng, X. Z. Gong, D. N. Ruzic, M. J. Ni, B. N. Wan, and J. G. Li, "Experiments of continuously and stably flowing lithium limiter in EAST towards a solution for the power exhaust of future fusion devices," *Nuclear Materials and Energy*, 2019.

[9] C. L. X. C. M. M. H. W. X. Y. W. Y. W. Q. Z. X. Z. G. G.Z. Zuo, J.S. Hu and E. Team, "Compatibility between a new limit-style flili and high confinement plasmas in east device," in *AAPPS-DPP2020*, 2020.

[10] D. Fasel and M. Q. Tran, "Availability of lithium in the context of future D-T fusion reactors," *Fusion Engineering and Design*, vol. 75, pp. 1163–1168, 2005.

[11] I. V. Kurchatov, "On the possibility of producing thermonuclear reactions in a gas discharge," *Journal of Nuclear Energy (1954)*, vol. 4, pp. 193–202, feb 1957.

[12] J. D. Lawson, "Some criteria for a power producing thermonuclear reactor," *Proceedings of the Physical Society. Section B*, vol. 70, no. 1, pp. 6–10, 1957.

[13] T. Boehly, D. Brown, R. Craxton, R. Keck, J. Knauer, J. Kelly, T. Kessler, S. Kumpan, S. Loucks, S. Letzring, F. Marshall, R. McCrory, S. Morse, W. Seka, J. Soures, and C. Verdon, "Initial performance results of the omega laser system," *Optics Communications*, vol. 133, no. 1, pp. 495–506, 1997.

[14] P. H. Rebut and B. E. Keen, "The jet experiment: Evolution, present status, and prospects," *Fusion Technology*, vol. 11, no. 1, pp. 13–42, 1987.

[15] R. Betti, P. Y. Chang, B. K. Spears, K. S. Anderson, J. Edwards, M. Fatenejad, J. D. Lindl, R. L. McCrory, R. Nora, and D. Shvarts, "Thermonuclear ignition in inertial confinement fusion and comparison with magnetic confinement," *Physics of Plasmas*, vol. 17, no. 5, 2010.

[16] S. Braginskii and V. Shafranov, "Plasma physics and the problem of controlled thermonuclear reactions vol 2 pergamon," 1959.

[17] L. Spitzer, "The Stellarator Concept," *Citation: The Physics of Fluids*, vol. 1, p. 253, 1958.

[18] C. Beidler, K. Allmaier, M. Y. Isaev, S. Kasilov, W. Kernbichler, G. Leitold, H. Maaßberg, D. Mikkelsen, S. Murakami, M. Schmidt, *et al.*, "Benchmarking of the mono-energetic transport coefficients—results from the international collaboration on neoclassical transport in stellarators (icnts)," *Nuclear Fusion*, vol. 51, no. 7, p. 076001, 2011.

[19] F. Sartori, G. de Tommasi, and F. Piccolo, "The joint european torus," *IEEE Control Systems Magazine*, vol. 26, no. 2, pp. 64–78, 2006.

[20] R. Pitts, "Fusion : the way ahead," vol. 19, no. 3, pp. 19–26, 2006.

[21] M. Mori, "Overview of the recent experimental results in JT-60 and JFT-2M," *Plasma Physics and Controlled Fusion*, vol. 36, no. 7 A, 1994.

[22] G. Manfredi and M. Ottaviani, "Gyro-Bohm scaling of ion thermal transport from global numerical simulations of ion-temperature-gradient-driven turbulence," *Physical Review Letters*, vol. 79, no. 21, pp. 4190–4193, 1997.

[23] M. Wakatani, V. Mukhovatov, K. Burrell, J. Connor, J. Cordey, Y. V. Esipchuk, X. Garbet, S. Lebedev, M. Mori, K. Toi, *et al.*, "Plasma confinement and transport," *Nuclear Fusion*, vol. 39, no. 12, pp. 2175–2249, 1999.

[24] E. Gibney, "Five-year delay would spell end of iter," *Nature. com. Nature Publishing Group*, vol. 31, 2014.

[25] F. Romanelli, P. Barabaschi, D. Borba, G. Federici, L. Horton, R. Neu, D. Stork, and H. Zohm, "Fusion electricity: A roadmap to the realization of fusion energy," 2012.

[26] N. J. Lopes Cardozo, A. G. Lange, and G. J. Kramer, "Fusion: Expensive and Taking Forever?," *Journal of Fusion Energy*, vol. 35, no. 1, pp. 94–101, 2016.

[27] F. Crisanti, R. Albanese, R. Ambrosino, G. Calabro, B. Duval, G. Giruzzi, G. Granucci, G. Maddaluno, G. Ramogida, H. Reimerdes, and R. Zagorski, "The DTT device: Rationale for the choice of the parameters," *Fusion Engineering and Design*, vol. 122, pp. 288–298, nov 2017.

[28] T. Eich, B. Sieglin, A. Scarabosio, W. Fundamenski, R. J. Goldston, and A. Herrmann, "Inter-ELM power decay length for JET and ASDEX Upgrade: Measurement and comparison with heuristic drift-based model," *Physical Review Letters*, vol. 107, no. 21, pp. 1–4, 2011.

[29] G. Federici, H. Wuerz, G. Janeschitz, and R. Tivey, "Erosion of plasma-facing components in ITER," in *Fusion Engineering and Design*, vol. 61-62, pp. 81–94, North-Holland, nov 2002.

[30] M. J. Baldwin and R. P. Doerner, "Formation of helium induced nanostructure 'fuzz' on various tungsten grades," *Journal of Nuclear Materials*, vol. 404, pp. 165–173, sep 2010.

[31] L. Keys, J. Smith, and J. Moteff, "High-temperature recovery of tungsten after neutron irradiation," *Physical Review*, vol. 176, no. 3, p. 851, 1968.

[32] W. Eckstein and J. László, "Sputtering of tungsten and molybdenum," *Journal of Nuclear Materials*, vol. 183, no. 1, pp. 19–24, 1991.

[33] T. Pütterich, R. Neu, R. Dux, A. D. Whiteford, M. G. O'Mullane, and H. P. Summers, "Calculation and experimental test of the cooling factor of tungsten," *Nuclear Fusion*, vol. 50, no. 2, 2010.

[34] A. Loarte, B. Lipschultz, A. S. Kukushkin, G. F. Matthews, P. C. Stangeby, N. Asakura, G. F. Counsell, G. Federici, A. Kallenbach, K. Krieger, A. Mahdavi, V. Philipps, D. Reiter, J. Roth, J. Strachan, D. Whyte, R. Doerner, T. Eich, W. Fundamenski, A. Herrmann, M. Fenstermacher, P. Ghendrih, M. Groth, A. Kirschner, S. Konoshima, B. Labombard, P. Lang, A. W. Leonard, P. Monier-Garbet, R. Neu, H. Pacher, B. Pegourie, R. A. Pitts, S. Takamura, J. Terry, and E. Tsitrone, "Chapter 4: Power and particle control," *Nuclear Fusion*, vol. 47, no. 6, 2007.

[35] H. Zohm, C. Angioni, E. Fable, G. Federici, G. Gantenbein, T. Hartmann, K. Lackner, E. Poli, L. Porte, O. Sauter, G. Tardini, D. Ward, and M. Wischmeier, "On the physics guidelines for a tokamak DEMO," *Nuclear Fusion*, vol. 53, no. 7, 2013.

[36] A. Kukushkin, H. Pacher, G. Janeschitz, A. Loarte, D. Coster, G. Matthews, D. Reiter, R. Schneider, and V. Zhogolev, "Basic divertor operation in iter-feat," *Nuclear fusion*, vol. 42, no. 2, p. 187, 2002.

[37] S. Krasheninnikov, A. Kukushkin, and A. Pshenov, "Divertor plasma detachment," *Physics of Plasmas*, vol. 23, no. 5, p. 055602, 2016.

[38] G. Matthews, "Plasma detachment from divertor targets and limiters," *Journal of nuclear materials*, vol. 220, pp. 104–116, 1995.

[39] A. Kallenbach, M. Bernert, R. Dux, L. Casali, T. Eich, L. Giannone, A. Herrmann, R. McDermott, A. Mlynek, H. Müller, *et al.*, "Impurity seeding for tokamak power exhaust: from present devices via iter to demo," *Plasma Physics and Controlled Fusion*, vol. 55, no. 12, p. 124041, 2013.

[40] G. Neilson, G. Federici, J. Li, D. Maisonnier, and R. Wolf, "Summary of the international workshop on magnetic fusion energy (mfe) roadmapping in the iter era; 7–10 september 2011, princeton, nj, usa," *Nuclear Fusion*, vol. 52, no. 4, p. 047001, 2012.

[41] F. Effenberg, S. Brezinsek, Y. Feng, R. König, M. Krychowiak, M. Jakubowski, H. Niemann, V. Perseo, O. Schmitz, D. Zhang, *et al.*, "First demonstration of radiative power exhaust with impurity seeding in the island divertor at wendelstein 7-x," *Nuclear Fusion*, vol. 59, no. 10, p. 106020, 2019.

[42] B. Lipschultz, B. LaBombard, E. Marmar, M. Pickrell, J. Terry, R. Watterson, and S. Wolfe, "Marfe: an edge plasma phenomenon," *Nuclear Fusion*, vol. 24, no. 8, p. 977, 1984.

[43] G. G. Plunk, P. Helander, P. Xanthopoulos, and J. W. Connor, "Collisionless microinstabilities in stellarators. I. Analytical theory of trapped-particle modes," *Physics of Plasmas*, vol. 21, p. 82303, 2014.

[44] M. Kotschenreuther, W. Dorland, M. A. Beer, and G. W. Hammett, "Quantitative predictions of tokamak energy confinement from first-principles simulations with kinetic effects ARTICLES YOU MAY BE INTERESTED IN Comparisons and physics basis of tokamak transport models and turbulence simulations Quantitative predictions o," *Physics of Plasmas*, vol. 2, p. 1904, 1995.

[45] A. de Castro, C. Moynihan, S. Stemmley, M. Szott, and D. Ruzic, "Lithium, a path to make fusion energy affordable," *Physics of Plasmas*, vol. 28, no. 5, p. 050901, 2021.

[46] G. Federici, A. Zhitlukhin, N. Arkhipov, R. Giniyatulin, N. Klimov, I. Landman, V. Podkovyrov, V. Safronov, A. Loarte, and M. Merola, "Effects of ELMs and disruptions on ITER divertor armour materials," in *Journal of Nuclear Materials*, vol. 337-339, pp. 684–690, North-Holland, mar 2005.

[47] A. Hassanein, "Prediction of material erosion and lifetime during major plasma instabilities in tokamak devices," jul 2002.

[48] J. Coenen, K. Krieger, B. Lipschultz, R. Dux, A. Kallenbach, T. Lunt, H. Mueller, S. Potzel, R. Neu, A. Terra, *et al.*, "Evolution of surface melt damage, its influence on plasma performance and prospects of recovery," *Journal of Nuclear Materials*, vol. 438, pp. S27–S33, 2013.

[49] D. Nishijima, M. Baldwin, R. Doerner, and J. Yu, "Sputtering properties of tungsten 'fuzzy'surfaces," *Journal of Nuclear Materials*, vol. 415, no. 1, pp. S96–S99, 2011.

[50] G. M. Wright, D. Brunner, M. J. Baldwin, R. P. Doerner, B. Labombard, B. Lipschultz, J. L. Terry, and D. G. Whyte, "Tungsten nano-tendril growth in the Alcator C-Mod divertor," *Nuclear Fusion*, vol. 52, no. 4, pp. 48–53, 2012.

[51] D. L. Rudakov, C. P. Wong, R. P. Doerner, G. M. Wright, T. Abrams, M. J. Baldwin, J. A. Boedo, A. R. Briesemeister, C. P. Chrobak, H. Y. Guo, E. M. Hollmann, A. G. McLean, M. E. Fenstermacher, C. J. Lasnier, A. W. Leonard, R. A. Moyer, D. C. Pace, D. M. Thomas, and J. G. Watkins, "Exposures of tungsten nanostructures to divertor plasmas in DIII-D," *Physica Scripta*, vol. 2016, no. T167, 2016.

[52] H. Sugai, H. Toyoda, K. Nakamura, K. Furuta, M. Ohori, K. Toi, S. Hirokura, and K. Sato, "Wall conditioning with lithium evaporation," *Journal of nuclear materials*, vol. 220, pp. 254–258, 1995.

[53] K. McGuire, H. Adler, P. Alling, C. Ancher, H. Anderson, J. Anderson, J. Anderson, V. Arunasalam, G. Ascione, D. Ashcroft, *et al.*, "Review of deuterium–tritium results from the tokamak fusion test reactor," *Physics of Plasmas*, vol. 2, no. 6, pp. 2176–2188, 1995.

[54] D. K. Mansfield, K. W. Hill, J. D. Strachan, M. G. Bell, S. D. Scott, R. Budny, E. S. Marmar, J. A. Snipes, J. L. Terry, S. Batha, R. E. Bell, M. Bitter, C. E. Bush, Z. Chang, D. S. Darrow, D. Ernst, E. Fredrickson, B. Grek, H. W. Herrmann, A. Janos, D. L. Jassby, F. C. Jobes, D. W. Johnson, L. C. Johnson, F. M. Levinton, D. R. Mikkelsen, D. Mueller, D. K. Owens, H. Park, A. T. Ramsey, A. L. Roquemore, C. H. Skinner, T. Stevenson, B. C. Stratton, E. Synakowski, G. Taylor, A. Von Halle, S. Von Goeler, K. L. Wong, and S. J. Zweben, "Enhancement of Tokamak Fusion Test Reactor performance by lithium conditioning," *Physics of Plasmas*, vol. 3, no. 5, pp. 1892–1897, 1996.

[55] L. Zakharov, "Vd shafranov and necessary conditions for fusion energy," *Plasma Physics Reports*, vol. 45, no. 12, pp. 1087–1092, 2019.

[56] S. I. Krasheninnikov, L. E. Zakharov, and G. V. Pereverzev, "On lithium walls and the performance of magnetic fusion devices," *Physics of Plasmas*, vol. 10, no. 5 II, pp. 1678–1682, 2003.

[57] Y. Hirooka, S. Hosaka, M. Nishiura, Y. Ohtsuka, and M. Nishikawa, "Helium ash removal by moving-surface plasma-facing components," *Journal of Nuclear Materials*, vol. 363-365, no. 1-3, pp. 775–780, 2007.

[58] Z. Sun, J. S. Hu, G. Z. Zuo, J. Ren, B. Cao, J. G. Li, and D. K. Mansfield, "Influence of lithium coatings with large-area coverage on EAST plasma performance," in *Fusion Engineering and Design*, vol. 89, pp. 2886–2893, Elsevier Ltd, dec 2014.

[59] D. P. Boyle, R. Majeski, J. C. Schmitt, C. Hansen, R. Kaita, S. Kubota, M. Lucia, and T. D. Rognlien, "Observation of Flat Electron Temperature Profiles in the Lithium Tokamak Experiment," *Physical Review Letters*, vol. 119, no. 1, pp. 1–6, 2017.

[60] L. E. Zakharov, "On a burning plasma low recycling regime with P DT = 23-26 MW, Q DT = 5-7 in a JET-like tokamak," *Nuclear Fusion*, vol. 59, no. 9, 2019.

[61] F. Wagner, A. Becoulet, R. Budny, V. Erckmann, D. Farina, G. Giruzzi, Y. Kamada, A. Kaye, F. Koechl, K. Lackner, *et al.*, "On the heating mix of iter," *Plasma Physics and Controlled Fusion*, vol. 52, no. 12, p. 124044, 2010.

[62] A. Loarte and D. Campbell, "The plasma physics aspects of the tritium burn fraction and the prediction for iter," in *4th IAEA DEMO Programme Workshop*, 2016.

[63] M. L. Apicella, G. Mazzitelli, V. Pericoli Ridolfini, V. Lazarev, A. Alekseyev, A. Vertkov, and R. Zagórski, "First experiments with lithium limiter on FTU," *Journal of Nuclear Materials*, vol. 363-365, no. 1-3, pp. 1346–1351, 2007.

[64] D. J. Battaglia, W. Guttenfelder, R. E. Bell, A. Diallo, N. Ferraro, E. Fredrickson, S. P. Gerhardt, S. M. Kaye, R. Maingi, and D. R. Smith, "Enhanced pedestal H-mode at low edge ion collisionality on NSTX," *Physics of Plasmas*, vol. 27, no. 7, 2020.

[65] R. Maingi, R. E. Bell, J. M. Canik, S. P. Gerhardt, S. M. Kaye, B. P. Leblanc, T. H. Osborne, M. G. Bell, E. D. Fredrickson, K. C. Lee, J. E. Menard, J. K. Park, and S. A. Sabbagh, "Triggered confinement enhancement and pedestal expansion in high-confinement-mode discharges in the national spherical torus experiment," *Physical Review Letters*, vol. 105, p. 135004, sep 2010.

[66] Y. Miura, "Study of improved confinement modes with edge and/or internal transport barriers on the Japan Atomic Energy Research Institute Tokamak-60 Upgrade (JT-60U)," *Physics of Plasmas*, vol. 10, no. 5 II, pp. 1809–1815, 2003.

[67] P. J. Catto and R. D. Hazeltine, "Isothermal tokamak," *Physics of Plasmas*, vol. 13, no. 12, 2006.

[68] R. J. Goldston, "Heuristic drift-based model of the power scrape-off width in low-gas-puff H-mode tokamaks," *Nuclear Fusion*, vol. 52, no. 1, 2012.

[69] R. Majeski, R. Bell, D. Boyle, P. Hughes, T. Kozub, A. LeViness, E. Merino, X. Zhang, J. Anderson, W. Capecchi, *et al.*, "First results from the lithium tokamak experiment-β," in *APS Division of Plasma Physics Meeting Abstracts*, vol. 2019, pp. GP10–131, 2019.

[70] J. Myra, D. Russell, and S. Zweben, "Theory based scaling of edge turbulence and implications for the scrape-off layer width," *Physics of Plasmas*, vol. 23, no. 11, p. 112502, 2016.

[71] M. Shimada and K. Tobita, "Magnetically guided liquid metal divertor (MAGLIMD) with resilience to disruptions and ELMs," *Plasma and Fusion Research*, vol. 15, pp. 1–10, 2020.

[72] V. Evtikhin, A. Vertkov, I. Lyublinski, B. Khripunov, V. Petrov, and S. Mirnov, "Research of lithium capillary-pore systems for fusion reactor plasma facing components," *Journal of nuclear materials*, vol. 307, pp. 1664–1669, 2002.

[73] S. V. Mirnov, V. B. Lazarev, S. M. Sotnikov, V. A. Evtikhin, I. E. Lyublinski, and A. V. Vertkov, "Li-CPS limiter in tokamak T-11M," *Fusion Engineering and Design*, vol. 65, no. 3 SPEC., pp. 455–465, 2003.

[74] V. Evtikhin, I. Lyublinski, A. Vertkov, A. Chumanov, E. Azizov, S. Mirnov, V. Lazarev, and S. Sotnikov, "Test of lithium capillary-pore systems on the t-11m tokamak," tech. rep., 2003.

[75] M. M. Szott, *Advanced geometries for dryout mitigation in TEMHD-driven liquid lithium systems*. PhD thesis, University of Illinois at Urbana-Champaign, 2020.

[76] T. W. Morgan, A. Vertkov, K. Bystrov, I. Lyublinski, J. W. Genuit, and G. Mazzitelli, "Power handling of a liquid-metal based CPS structure under high steady-state heat and particle fluxes," *Nuclear Materials and Energy*, vol. 12, pp. 210–215, 2017.

[77] J. Ren, G. Z. Zuo, J. S. Hu, Z. Sun, J. G. Li, L. E. Zakharov, D. N. Ruzic, and W. Y. Xu, "Investigations on interactions between the flowing liquid lithium limiter and plasmas," *Fusion Engineering and Design*, vol. 102, pp. 36–43, 2016.

[78] G. Z. Zuo, J. S. Hu, R. Maingi, J. Ren, Z. Sun, Q. X. Yang, Z. X. Chen, H. Xu, K. Tritz, L. E. Zakharov, C. Gentile, X. C. Meng, M. Huang, W. Xu, Y. Chen, L. Wang, N. Yan, S. T. Mao, Z. D. Yang, and J. G. Li, "Mitigation of plasma-material interactions via passive Li efflux from the surface of a flowing liquid lithium limiter in EAST," *Nuclear Fusion*, vol. 57, no. 4, 2017.

[79] G. Zuo, J. Hu, R. Maingi, Z. Sun, Q. Yang, M. Huang, X. Meng, W. Xu, Y. Qian, C. Li, H. Bi, Y. Chen, X. Yuan, X. Han, X. Zhu, Y. Wang, L. Zhang, H. Liu, L. Wang, X. Gong, K. Tritz, A. Diallo, R. Lunsford, M. Ni, and J. Li, "Results from an improved flowing liquid lithium limiter with increased flow uniformity in high power plasmas in EAST," *Nuclear Fusion*, vol. 59, no. 1, p. 016009, 2019.

[80] E. Kolemen, M. Hvasta, R. Majeski, R. Maingi, A. Brooks, and T. Kozub, "Design of the Flowing LIquid Torus (FLIT)," *Nuclear Materials and Energy*, vol. 19, no. August 2018, pp. 524–530, 2019.

[81] J. A. Shercliff, "Thermoelectric magnetohydrodynamics," *Journal of Fluid Mechanics*, vol. 91, no. 2, pp. 231–251, 1979.

[82] M. A. Jaworski, T. K. Gray, M. Antonelli, J. J. Kim, C. Y. Lau, M. B. Lee, M. J. Neumann, W. Xu, and D. N. Ruzic, "Thermoelectric magnetohydrodynamic stirring of liquid metals," *Physical Review Letters*, vol. 104, no. 9, pp. 1–4, 2010.

[83] W. Xu, P. Fiflis, M. Szott, K. Kalathiparambil, S. Jung, M. Christenson, I. Haehnlein, A. Kapat, D. Andruczyk, D. Curreli, and D. N. Ruzic, "Vertical flow in the Thermoelectric Liquid Metal Plasma Facing Structures (TELS) facility at Illinois," *Journal of Nuclear Materials*, vol. 463, pp. 1181–1185, 2015.

[84] D. N. Ruzic, W. Xu, D. Andruczyk, and M. A. Jaworski, "Lithium-metal infused trenches (LiMIT) for heat removal in fusion devices," *Nuclear Fusion*, vol. 51, no. 10, 2011.

[85] D. N. Ruzic, M. Szott, C. Sandoval, M. Christenson, P. Fiflis, S. Hammouti, K. Kalathiparambil, I. Shchelkanov, D. Andruczyk, R. Stubbers, C. J. Foster, and B. Jurczyk, "Flowing liquid lithium plasma-facing components – Physics, technology and system analysis of the LiMIT system," *Nuclear Materials and Energy*, vol. 12, pp. 1324–1329, 2017.

[86] W. Xu, D. Curreli, D. Andruczyk, T. Mui, R. Switts, and D. N. Ruzic, "Heat transfer of TEMHD driven lithium flow in stainless steel trenches," *Journal of Nuclear Materials*, vol. 438, no. SUPPL, pp. 422–425, 2013.

[87] J. Ren, J. S. Hu, G. Z. Zuo, Z. Sun, J. G. Li, D. N. Ruzic, and L. E. Zakharov, "First results of flowing liquid lithium limiter in HT-7," *Physica Scripta*, vol. T159, 2014.

[88] P. Fiflis, T. W. Morgan, S. Brons, G. G. Van Eden, M. A. Van Den Berg, W. Xu, D. Curreli, and D. N. Ruzic, "Performance of the lithium metal infused trenches in the magnum PSI linear plasma simulator," *Nuclear Fusion*, vol. 55, no. 11, 2015.

[89] P. Rindt, T. W. Morgan, M. A. Jaworski, and N. J. Lopes Cardozo, "Power handling limit of liquid lithium divertor targets," *Nuclear Fusion*, vol. 58, no. 10, 2018.

[90] P. Rindt, T. W. Morgan, G. G. Van Eden, M. A. Jaworski, and N. J. Lopes Cardozo, "Power handling and vapor shielding of pre-filled lithium divertor targets in Magnum-PSI," *Nuclear Fusion*, vol. 59, no. 5, 2019.

[91] R. J. Goldston, A. Hakim, G. W. Hammett, M. A. Jaworski, and J. Schwartz, "Recent advances towards a lithium vapor box divertor," *Nuclear Materials and Energy*, vol. 12, pp. 1118–1121, 2017.

[92] M. Ono, M. A. Jaworski, R. Kaita, Y. Hirooka, D. Andruczyk, and T. K. Gray, "Active radiative liquid lithium divertor concept," *Fusion Engineering and Design*, vol. 89, no. 12, pp. 2838–2844, 2014.

[93] J. N. Brooks, T. D. Rognlien, D. N. Ruzic, and J. P. Allain, "Erosion/redeposition analysis of lithium-based liquid surface divertors," *Journal of Nuclear Materials*, vol. 290-293, pp. 185–190, 2001.

[94] A. A. Pshenov and A. S. Kukushkin, "Modelling of lithium transport and its influence on the edge plasma parameters in T-15MD tokamak," *Journal of Physics: Conference Series*, vol. 941, no. 1, pp. 0–5, 2018.

[95] C. B. Alcock, V. P. Itkin, and M. K. Horrigan, "Vapour pressure equations for the metallic elements: 298-2500k," *Canadian Metallurgical Quarterly*, vol. 23, no. 3, pp. 309–313, 1984.

[96] J. P. Allain and J. N. Brooks, "Lithium surface-response modelling for the NSTX liquid lithium divertor," *Nuclear Fusion*, vol. 51, no. 2, 2011.

[97] Y. Homma, K. Hoshino, S. Yamoto, N. Asakura, S. Tokunaga, A. Hatayama, Y. Sakamoto, R. Hiwatari, K. Tobita, and J. S. D. T. f. F. DEMO, "Numerical analysis of tungsten erosion and deposition processes under a DEMO divertor plasma," *Nuclear Materials and Energy*, vol. 12, pp. 323–328, 2017.

[98] A. De Castro, A. Sepetys, M. González, and F. L. Tabarés, "Temperature dependence of liquid lithium film formation and deuterium retention on hot W samples studied by LID-QMS. Implications for future fusion reactors," *Nuclear Fusion*, vol. 58, no. 4, 2018.

[99] J. D. Huba, *NRL plasma formulary*, vol. 6790. Naval Research Laboratory, 1998.